REPORT DOCUMENTATION PAGE

Form Approved
OMB No. 0704-0188

Public reporting burden for this collection of information is estimated to average 1 hour per response, including the time for reviewing instructions, searching existing data sources, gathering and maintaining the data needed, and completing and reviewing the collection of information. Send comments regarding this burden estimate or any other aspect of this collection of information, including suggestions for reducing this burden, to Washington Headquarters Services, Directorate for Information Operations and Reports, 1215 Jefferson Davis Highway, Suite 1204, Arlington, VA 22202-4302, and to the Office of Management and Budget, Paperwork Reduction Project (0704-0188), Washington, DC 20503

1. AGENCY USE ONLY *(Leave Blank)*

2. REPORT DATE
04/21/00

3. REPORT TYPE AND DATES COVERED
Final Report 09/30/93 - 04/30/99

4. TITLE AND SUBTITLE

Deformation and Failure in Functionally Gradient Materials

5. FUNDING NUMBERS
Grant No.: N00014-93-1-1164
PR 98PR00775-01
P O Code ONR 334
CAGE Code. 50854

6. AUTHORS

R. J. Asao

7. PERFORMING ORGANIZATION NAME(S) AND ADDRESS(ES)

The Regents of The University of California
University of California, San Diego
Department of Mechanical and Aerospace Engineering
9500 Gilman Drive
La Jolla, CA 92093-0411

8. PERFORMING ORGANIZATION REPORT NUMBER

8. SPONSORING / MONITORING AGENCY NAME(S) AND ADDRESS(ES)

Office of Naval Research
San Diego Regional Office suite 300
San Diego, CA 92121-3019

10. SPONSORING / MONITORING AGENCY REPORT NUMBER

11. SUPPLEMENTARY NOTES

None

12a. DISTRIBUTION / AVAILABILITY STATEMENT

Public Release Without Limitations

DISTRIBUTION STATEMENT A
Approved for Public Release
Distribution Unlimited

12b. DISTRIBUTION CODE

13. ABSTRACT *(Maximum 200 words)*

Several aspects regarding the mechanical behavior of functionally graded materials have been investigated. In particular, the microstructure's effect of the failure initiation under thermal loading has been modeled by a computational micro-mechanics model, cracks in various geometries and gradient variation forms have been studied and calibrated for testing these materials.

14. SUBJECT TERMS

15. NUMBER OF PAGES

16. PRICE CODE

17. SECURITY CLASSIFICATION OF REPORT

18. SECURITY CLASSIFICATION OF THIS PAGE

19. SECURITY CLASSIFICATION OF ABSTRACT

20. LIMITATION OF ABSTRACT

20000601 038

DTIC QUALITY INSPECTED 1

Summary on Studies of Functionally Graded Materials

For functionally graded materials (FGMs), the change of microstructures induces material gradients, and makes them different in behavior from other materials, homogeneous and conventional composite materials. Our current study has been focused on the following two aspects: (1) Micro-residual-stress under thermal loading. A physical based computational model is developed to study microstructures in FGMs under thermal loading. The influence of discrete microstructure on residual stress at the grain size level is examined. (2) Fracture mechanics. In particular, the study has been carried out to determine the effect of material gradients on the crack tip for various loadings and geometries, including the commonly used specimens, under the small-scale yielding condition. A locally homogeneous model has been proposed to predict the crack propagation direction under the influence of loading, geometry and material gradients. Both analytical and numerical methods have been investigated for crack mechanics of the non-traditional, non-homogeneous materials. The brief summary of our work is as follows according to the two aspects.

(a) Effect of Microstructure on FGMs

The microstructures of FGMs are discrete and random in nature. The heterogeneous structure causes locally concentrated residual stress during thermal loading, as we have shown in calculations using micro-mechanics model. The effect of discrete microstructure on residual stress distribution at the grain size level are examined with respect to material gradients and FGM volume percentage within a ceramic-FGM interlayer-metal layer system. Both thermal-elastic and thermal-plastic deformations are considered, and the plastic behavior of metal grain is modeled by crystal plasticity theory. The results are compared with those obtained using a continuous model which does not consider the microstructure. In the averaged sense both micro-mechanics model and continuous model give the same macroscopic stress, whereas the micro-mechanics model predicts fairly high stress concentration at the grain size level, higher than 700 MPa for 300 degree temperature drop in $Ni-Al_2O_3$ system. Statistical analysis shows that the stress concentration is insensitive to material gradients and FGM volume percentage. This suggests that the consideration of microstructure of FGM for detailed analysis is needed.

Figure 1 is our computational model in which the difference of the continuous model and micro-mechanical model is clearly seen. Figure 2 shows the contour plots of (a) averaged in-plane principal stress p and (b) accumulated sum of slips developed in the linear gradient, 40% FGM. The temperature drop was from 700 to $400^{\circ}C$. Similar to the elastic case, the stress distribution is inhomogeneous, with many metal grains experiencing high tensile stresses and many ceramic grains experiencing compressive stresses. Stress concentration in the ceramic grains is significantly reduced in the region where metal content is greater than 70vol% due to plastic relaxation. With only 300 degree temperature drop, Figure 2(b) shows that: (a) there is plastic strain accumulation in many of metal grains, and (b) certain sites have relatively high strain accumulations, about 1.5%. The high strain accumulation seems to appear in the regions where metal content is between 50 to 75%. Figure 3 shows the distribution profiles of averaged in-plane stress in FGM layer for both elastic and plastic cases. The plastic relaxation effect is very clear here since stresses are in general shifted to lower magnitudes. The distribution for high tensile stresses with p>700Mpa, however, has reduced only slightly with plastic relaxation. Similar to the thermal-elastic case, the stress distribution profile for high tensile stress regions is insensitive to material gradient and FGM volume percentage. On the other hand, the distribution profile for high compressive stresses with p<-2500Mpa (mostly in ceramic grains) drops significantly. This suggests that, when ceramic grains are subject to tensile stresses if temperature increases, the plastic relaxation effects may reduce their tensile stress concentrations. We average stresses over each column of elements for the plastic solution to obtain the averaged in-plane stresses. Compared with the elastic averaged in-plane stresses, it is found that the metal rich section and part of the pure metal region are under general macroscopic yielding, which sets the maximum magnitude of the macroscopic stresses for the plastic case.

We also employ APSP (averaged peak stress of p) to treat the data obtained. The term 6% APSP is the stress p averaged over the 6vol% microstructure of the FGM layer which has the highest tensile stresses (p); similar, one can obtain 3vol% APSP etc. Figure 4 shows the 6vol% APSP for different material gradients and different FGM volume percentages, and for both elastic (marked with EL) and plastic solution (marked with PL). From it, the distribution profile for high stresses is found to insensitive to material gradients and FGM volume percentages, and the plastic relaxation effect is relatively small for high stresses. Similar conclusion can be obtained for 3vol% APSP.

(b) Cracks in FGMs

In the crack problems we have studied, a closed form solution for a semi-infinite crack in a FGM strip is obtained. From the fundamental solution, we have found these useful solutions: four-point-bending specimen, orthotropic cracked FGM plate. These results show that the material gradients do have a strong effect on the stress intensity factors and the mode mixity which measures the proportion of mode I to mode II at the crack tip. The magnitude of the stress intensity and the mode mixity are considered as the most important factors to determine crack propagation in FGMs. The documented complete solution can be used in fracture testing of FGMs. For the small-scale yielding crack, crack deflection initiation in FGMs is studied by the locally homogeneous model. In the model, the effect of microstructure at the tip region is neglected and as in all of our work for crack problems up to now the FGMs are considered as perfectly non-homogeneous materials with gradients of material properties at macroscopic level. The locally homogeneous model neglects the second order effects and is a first order approximation. Using it, we have examined the crack propagation direction in several cracked specimens. In our numerical study, a simplified method is found for calculating crack tip field of FGMs in finite element analysis. We show that the standard domain integral is sufficiently accurate when applied for FGMs at the small domain near crack tip, and the non-homogeneous term is very small compared to the standard domain integral. We have given the error estimation in terms of domain size, material properties and their gradients. The numerical results for both two-dimensional and three-dimensional problems show that the method is accurate and efficient. The advantage of the method is that, it does not require the input of material gradients and the existing finite element codes can be used for FGMs without much additional work.

Figure 5 and 6 show some of the cracked geometries we have solved using both analytical and numerical methods. Figure 7 shows the solution of mode I stress intensity factor vs. the position of the crack tip in the FGM for linear material variation in the three-layered three-point-bending specimen shown in Figure 6, where $h/H = 0.1$. The geometry is the case that the interlayer of

FGM is considerably thin compared to the two bulk materials. The solutions of this kind for various *h/H* and material variation form a complete solution for the three point bending specimen. Usually tough materials such as metals have lower modulus than brittle materials such as ceramics. From this figure, when the crack travels from tough side (the side with smaller modulus) to brittle side (the side with larger modulus) the crack tip stresses increases. When the toughness of the two bulk materials are different, it is expected to vary along the thickness of the FGM and can be written as $\Gamma((a-H)/H)$ in the FGM. Then, for stable growth in the FGM we have: (a) the energy release rate is equal to the toughness, and (b) the rate of change of energy release rate with respect to the crack length is less than that of the toughness. For unstable growth, in (b) the "less" is replaced by "greater". Let's look a special case where the toughness is constant across the thickness of the FGM. From the figure, we see in this special case that when material #2 is much softer than material #1, $E_2/E_1 << 1$, the crack growth is likely to be stable. This is especially true when the crack tip is close to material #2. When material #2 is stiffer than material #1, the crack growth is likely to be unstable. In general, if the toughness varies with position and the crack is close to material #2 with $E_2/E_1 << 1$, it is likely to be stable growth since the drop of the slop in the figure is very strong in the region and it is likely to overcome the drop of the toughness. Figure 8 is the case that $h/H = 0.5$ and other parameters are the same as Figure 7. From the two figures we see that the trend of these curves has a dramatic change as the percentage of the FGM changes, and this is especially true for those curves with $E_2/E_1 < 1$. In most part of Figure 8 the stress intensity factor increases as the crack length increases. This means that if the increase of the toughness at the crack tip as the crack length increases is not as fast as the stress intensity factor, it is an unstable growth for the crack tip traveling at most part of the FGM and for every E_2/E_1. In the discussion of the crack growth, we have assumed that the crack propagates along the original direction, since these are the cases where geometry, loading and material are symmetric with respect to the crack line. A first order approximation model, which is based on the local homogeneity, has been used by us to examine the crack propagating direction for several cracked FGM geometries. The model also predicts that crack grows along its original direction when everything is symmetric.

(c) Further Work under Consideration

Our further work, including the work being carried on, concentrates on the following unsolved problems relating to the understanding of FGMs' behavior as well as the implication of these understandings on the design aspects and material selection for the Hi-Temp purpose:

- Continue our study in micro-mechanical modeling of residual stress under thermal loading. Carry out more detailed analysis on the micro-stress concentration by investigating more FGM systems and more geometries so that more insight can be obtained regarding to sensitivity of local stress concentration to FGM volume percentage and material gradients. Morever, include cyclic loading and combined thermal-mechanical loading. Advanced aspect on crystal plasticity theory to account for the metal particles' detailed deformation will be developed.

- Plastic and visco-plastic mechanism at the crack tip region in FGMs under thermal, mechanical, and combined thermal and mechanical loadings, including detailed characterization of the crack tip field under these loadings and for various material gradient effects. This will involve both analytical and large scale finite element computation studies. For the non-linear finite element analysis for non-homogeneous cracked materials, the effective numerical method will be investigated.

- Develop a phenomenological theory based on experimental evidence, or from micromechanics at a smaller scale which can account for the interaction of the two particles phases, to characterize the toughness of FGMs; determine the crack propagation in terms of various parameters including material gradients and the crack tip position; and also determine the crack path, the direction of deflection, using second order and more accurate theory.

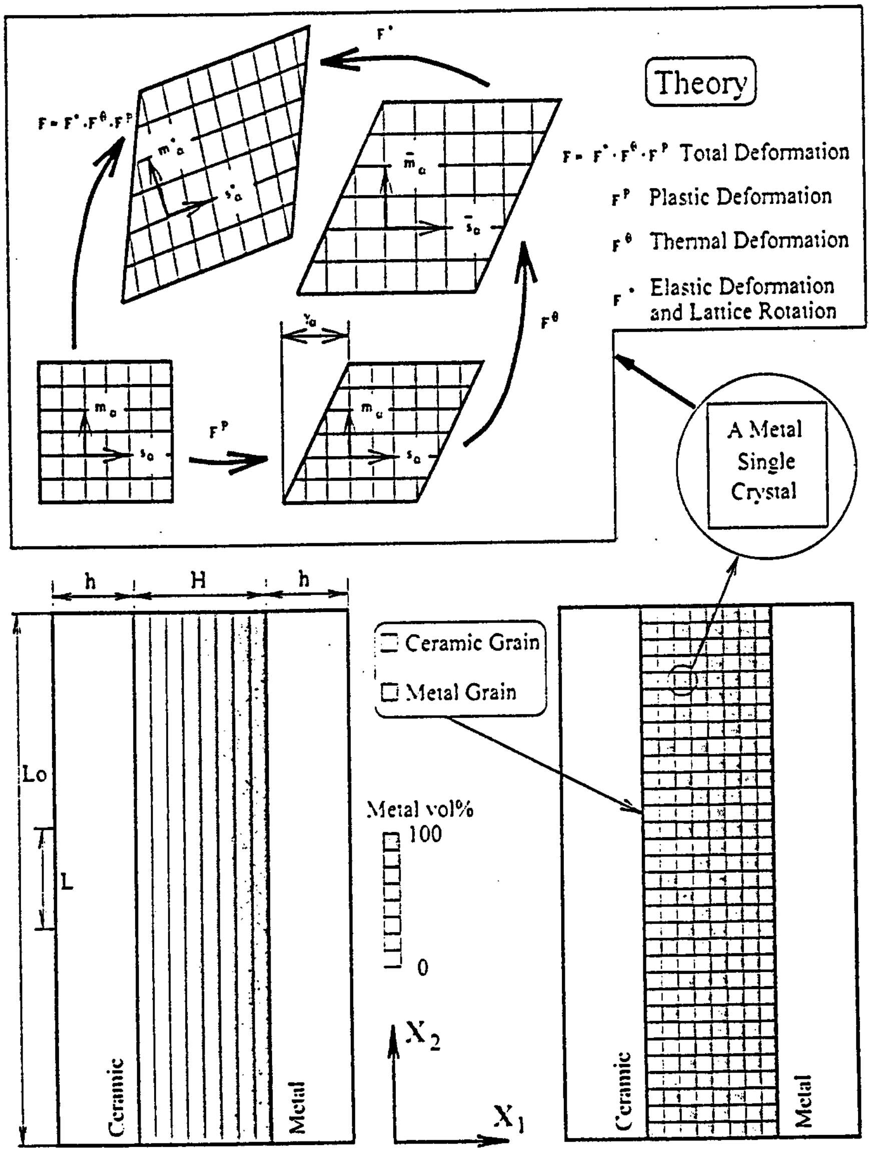
Theory
F = F* · F^θ · F^p Total Deformation
F^p Plastic Deformation
F^θ Thermal Deformation
F* Elastic Deformation and Lattice Rotation
F = F*.F^θ.F^p
F*
F^p
F^θ
γα
mα
sα
A Metal Single Crystal
Ceramic Grain
Metal Grain
h
H
h
Lo
L
Metal vol%
100
0
X2
X1
Ceramic
Metal
Ceramic
Metal

(a) Continuous Model

(b) Micromechanics Model

Figure 1. Schematic drawings of ceramic/FGM/metal structures, with (a) continuous model and (b) discrete micro-mechanics model using crystal plasticity theory

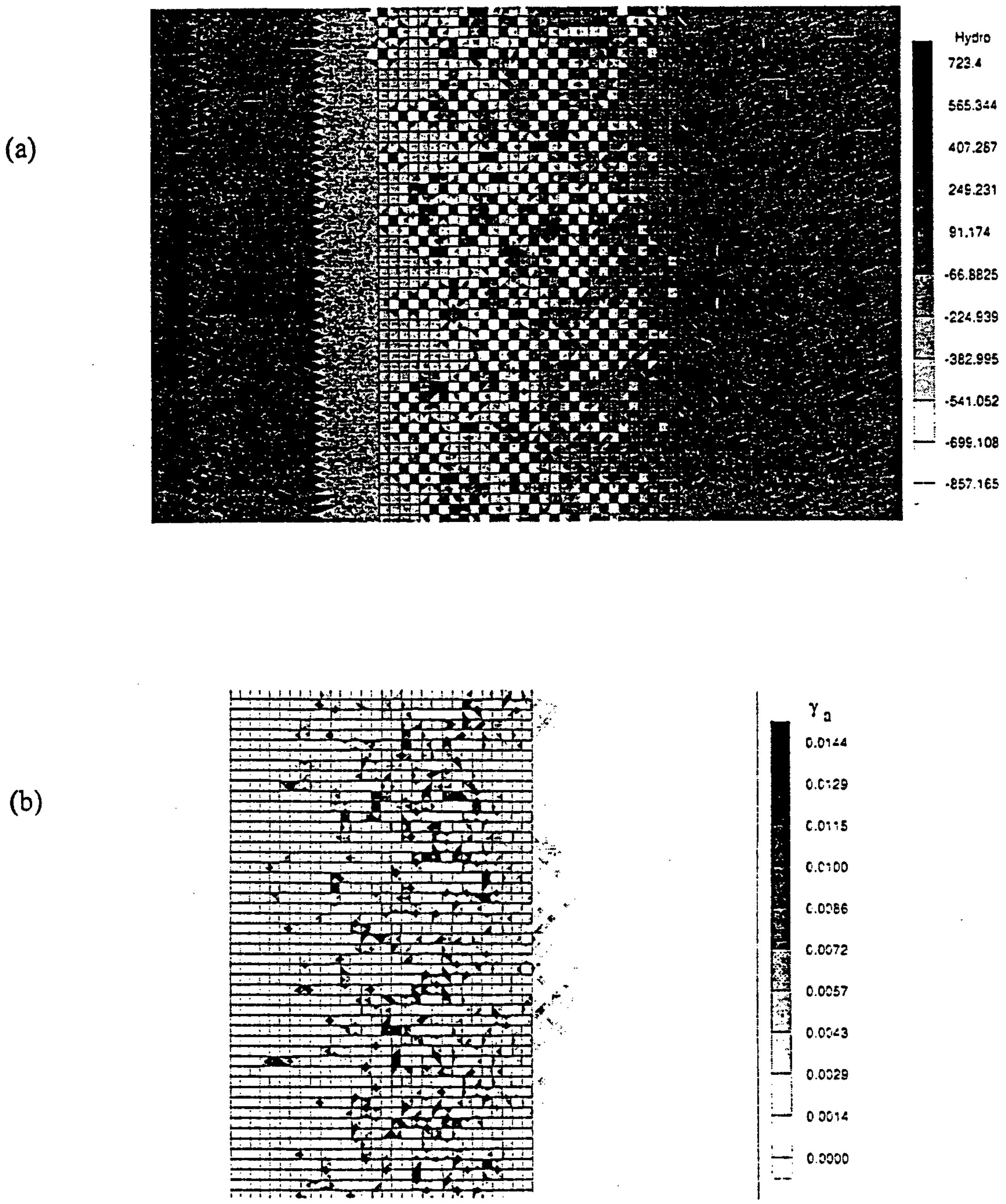

Figure 2. Contour plots of (a) hydrostatic stress and (b) accumulated sum of slip developed in the linear gradient 40vol% FGM.

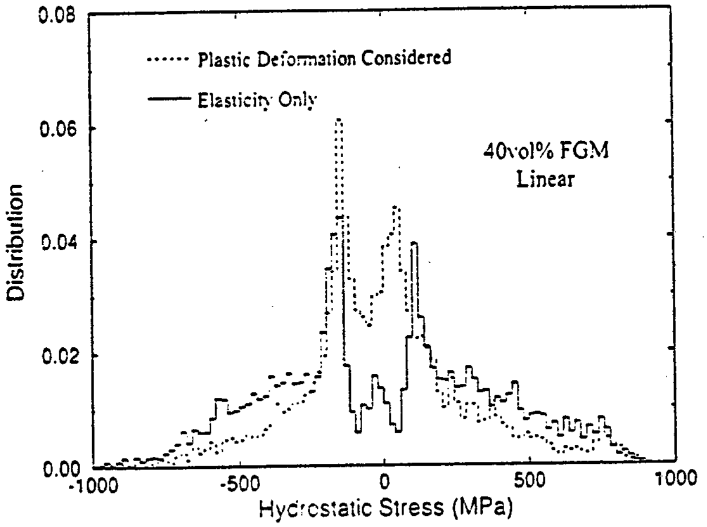

Figure 3. Hydrostatic stress distribution profiles developed in the FGM layer (40vol% FGM with linear gradient) for both elastic and plastic cases.

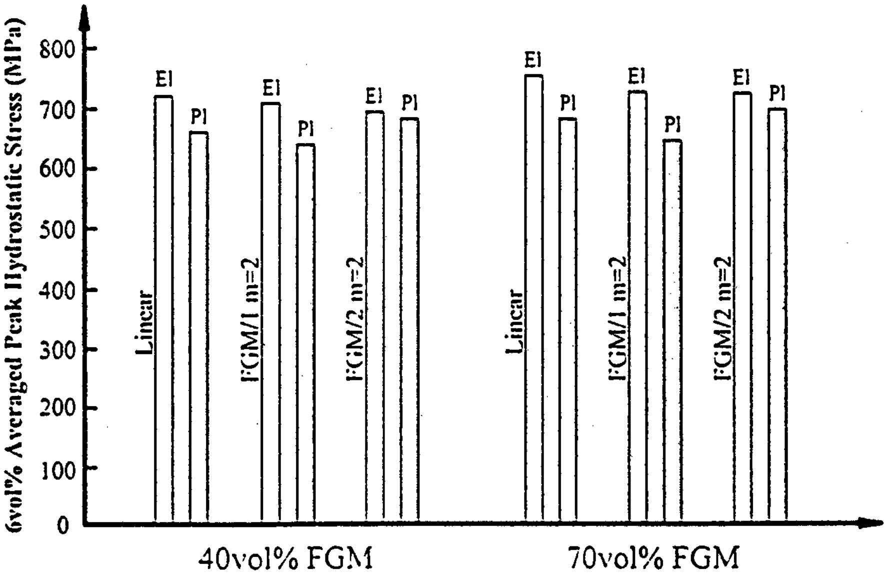

Figure 4. The 6vol% APSP for different gradients, volume percentage and for both elastic and plastic solutions.

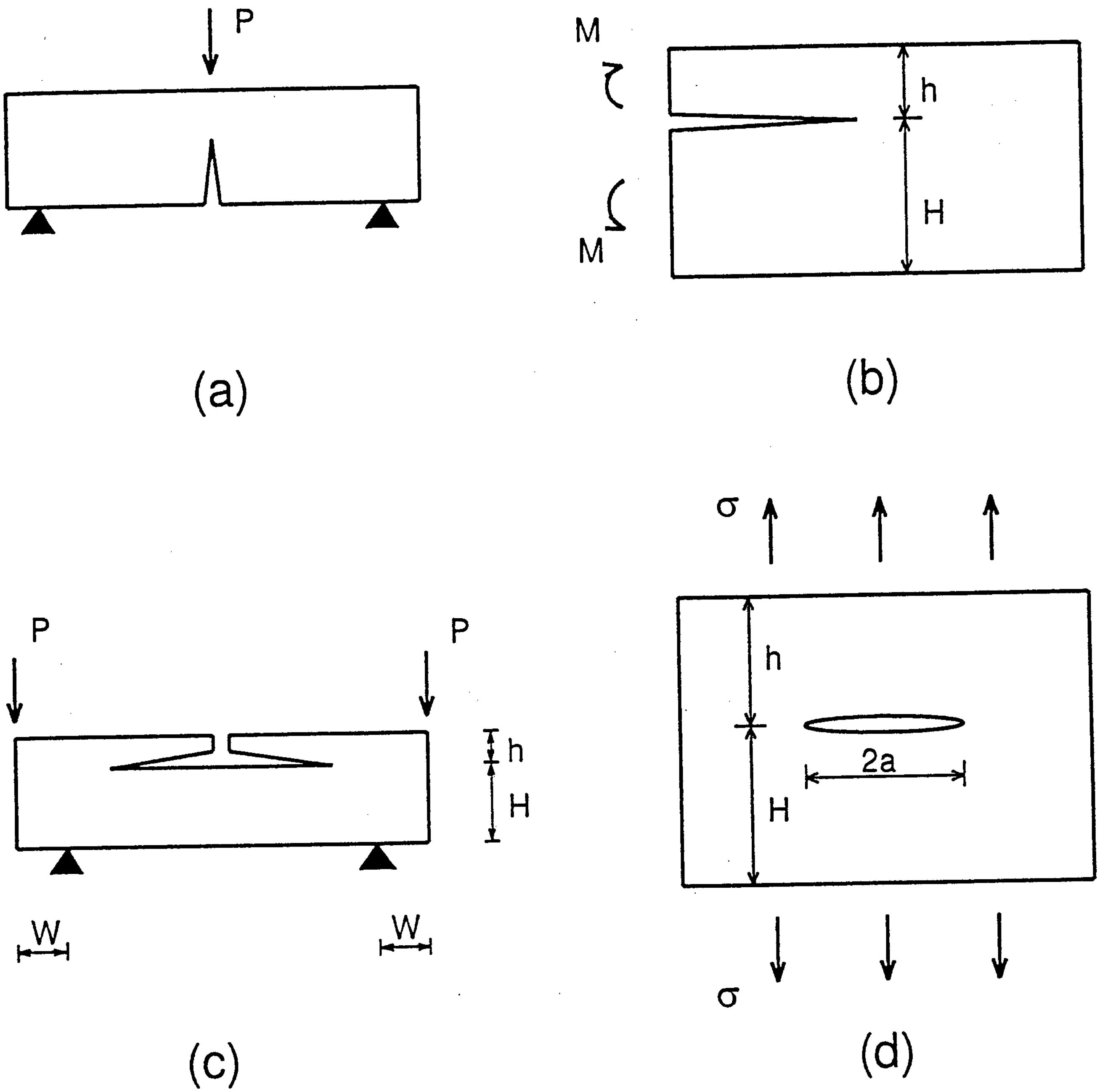
P
M
h
H
M
(a)
(b)
σ
P
P
h
H
W
W
h
2a
H
σ
(c)
(d)

Figure 5. Several cracked specimens of FGMs.

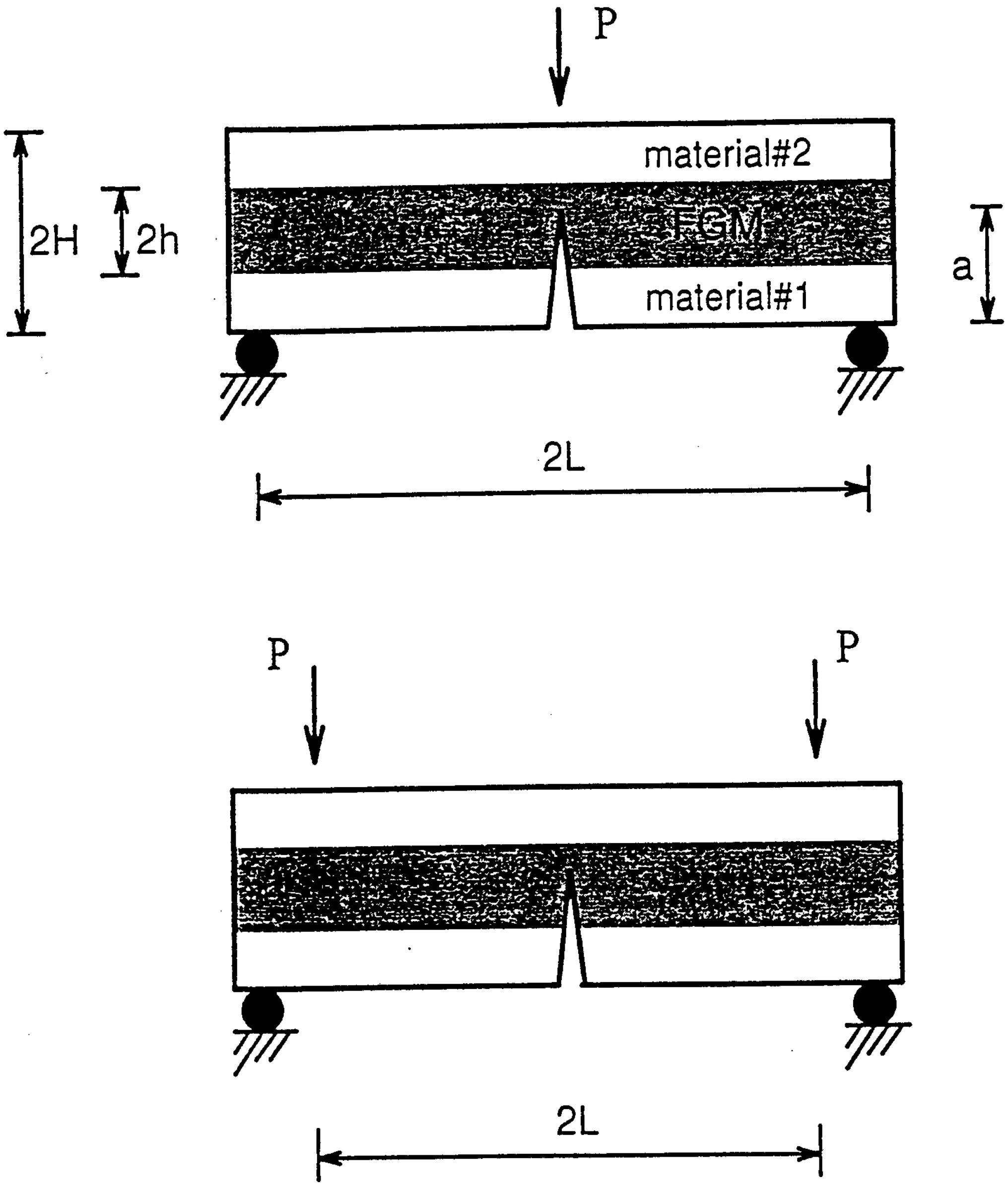
P
material#2
FGM
material#1
2H
2h
a
2L
P
P
2L

Figure 6. Sandwiched structures with interlayers being FGMs.

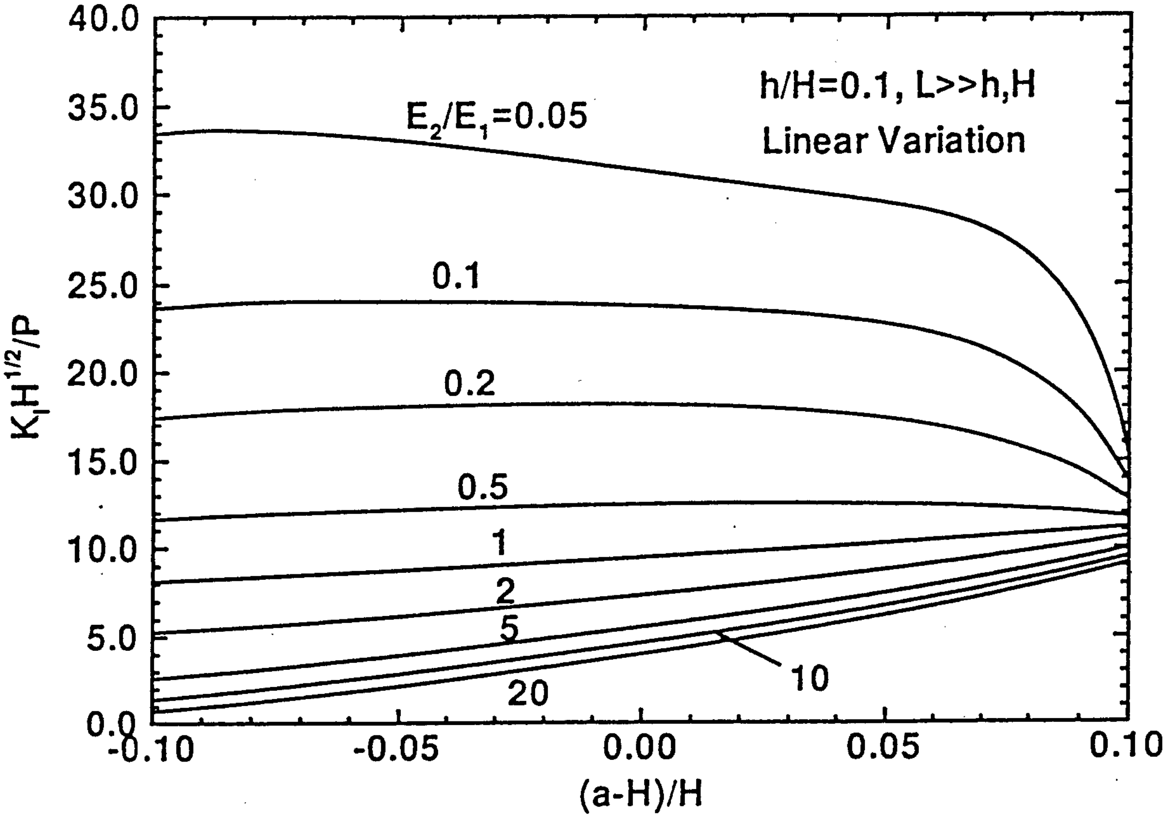

Figure 7. Stress intensity factor vs. the crack tip position inside the FGM interlayer for the three point bending structure in Figure 6 with h/H=0.1.

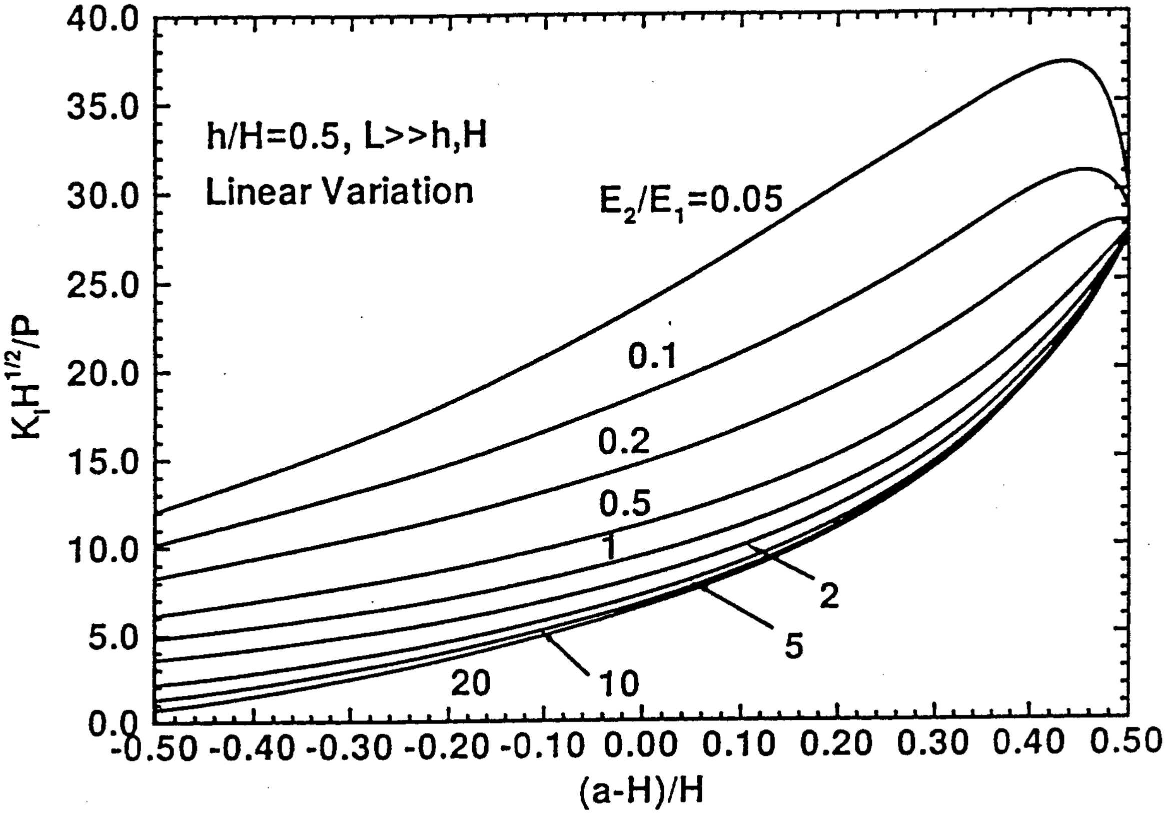

Figure 8. Stress intensity factor vs. the crack tip position inside the FGM interlayer for the three point bending structure in Figure 6 with h/H=0.5.

Pergamon

Int. J. Solids Structures Vol. 34, No. 24, pp. 3085–3098, 1997
© 1997 Elsevier Science Ltd
All rights reserved. Printed in Great Britain
0020–7683/97 $17.00 + .00

PII: S0020–7683(96)00175–8

CRACK DEFLECTION IN FUNCTIONALLY GRADED MATERIALS

PEI GU and R. J. ASARO
Department of Applied Mechanics and Engineering Sciences, Mail Code 0411,
University of California at San Diego, 9500 Gilman Drive, La Jolla, CA 92093-0411, U.S.A.

(*Received* 18 *April* 1996; *in revised form* 7 *August* 1996)

Abstract—Small crack deflection in brittle functionally graded materials (FGMs) is studied. The FGMs are modeled as simply nonhomogeneous materials, i.e., the effect of microstructure is neglected and the material property variation is considered to be continuous. Considering local homogeneity and the small scale inelasticity of brittle materials, the toughness is taken to be independent of direction; therefore, the crack propagates along the direction of maximum energy release rate, or the direction which gives a vanished mode II stress intensity factor. Kink directions for several specimens which may be used to experimentally study fracture behavior of FGMs are calculated. It is shown that material gradients have a strong effect on the kink direction when the crack is at the central region of a FGM, whereas they have little effect when the crack is close to the boundaries of the FGM. © 1997 Elsevier Science Ltd.

1. INTRODUCTION

In functionally graded materials (FGMs), although the absence of sharp interfaces does largely reduce material property mismatch, cracks occur when they are subjected to external loadings (Yamanouchi *et al.*, 1990; Holt *et al.*, 1993). Fractures induced by these cracks may in large part determine the overall mechanical and thermal-mechanical responses of FGMs. The need to understand, quantify and improve the toughness of FGMs has brought interest in a fracture mechanics methodology for such materials. In our recent work (Gu and Asaro, 1997), stress intensity factors of several specimens composed of FGMs were solved; the effect of material gradients on near-tip fields was determined; and possible fracture criterion was discussed. In this paper, we address crack deflection (or kinking) in brittle FGMs, i.e., for crack with arbitrary orientation, we study the direction of its extension when the critical condition is met. Here, brittle FGMs are those having strictly linear response. An example is the Si-C FGM system in which both material phases are brittle. For those FGMs made of metal and ceramic phases, the present model gives an approximate solution if the crack is on the brittle-behaved ceramic-rich side. If the crack is at the metal-rich side, its propagation is primarily via plastic mechanisms. Our study aimed at non-linear crack tip behavior is ongoing (Gu and Asaro, 1996), and will be discussed elsewhere.

The crack deflection model is developed in the same spirit as that for homogeneous materials (Cotterell and Rice, 1980) and for bimaterials with interface cracks (He and Hutchinson, 1989). The crack tip stress and displacement fields of FGMs, as briefly discussed in Section 2, take the same forms as those for homogeneous materials. Based on this fact, the asymptotic problem, which has a homogeneous body, is employed to study the crack tip behavior. Considering the local homogeneity and small-scale inelasticity of brittle materials around the crack tip, the toughness is taken to be independent of direction at a fixed point. It follows that the crack propagates along the direction of maximum energy release rate or the direction in which the mode II stress intensity factor vanishes. The kink direction is a function of the external loading, the geometry, and elastic property's gradients of a given specimen. After a short discussion on crack deflection model for homogeneous materials and for bimaterials in Section 3.1 and Section 3.2, we present that for FGMs in Section 3.3, in which the asymptotic problem based on the K-field and the directional independence of the toughness are discussed in detail. Kink angles for four-point bending specimen, double-cantilever beam and center cracked plate are calculated in Section 4, and the following qualitative results are obtained from the solution. For the four-point bending specimen, the crack intends to grow to the more compliant side. For the double-cantilever beam and center cracked plate, when the crack is at the middle of the specimen or at the compliant side, it intends to grow to the more compliant side, whereas when the crack is at the stiff side it intends to grow to the stiffer side. The material gradients do have a strong effect on the kink angle when the crack is at the middle of the FGM; but the effect is small when the crack is close to the boundaries of the FGM. We also investigate crack propagation in a compositionally graded interface. It is found that of the two Dundurs' parameters, α and β (see eqn 12), the effect of the former on the kink angle is stronger than the latter.

2. CRACK TIP FIELDS OF FGMs

For the purpose of studying crack kinking, the major results of the crack tip fields in FGMs are highlighted; detailed discussion can be found in Gu and Asaro (1997). The functionally graded material shown in Fig. 1 is considered as a nonhomogeneous material whose material properties vary continuously. Stresses near the crack tip have a square-root singularity, and singular terms of the stresses are of the form:

$$\sigma_{ij} = \frac{K_I}{\sqrt{2\pi r}}\bar{\sigma}^{I}_{ij}(\theta) + \frac{K_{II}}{\sqrt{2\pi r}}\bar{\sigma}^{II}_{ij}(\theta) + \frac{K_{III}}{\sqrt{2\pi r}}\bar{\sigma}^{III}_{ij}(\theta), \tag{1}$$

where $i, j = 1,2,3$; r and θ are the polar coordinates shown in Fig. 1. The dimensionless angular functions $\bar{\sigma}^{I}_{ij}(\theta)$, $\bar{\sigma}^{II}_{ij}(\theta)$ and $\bar{\sigma}^{III}_{ij}(\theta)$ are the same as those for homogeneous materials. The result is independent of the form for material properties and the orientation of the crack. The stress intensity factors K_I, K_{II} and K_{III} are functions of the material gradients, external loading, and geometry. Material gradients do not affect the order of the singularity and the angular functions, but do affect the stress intensity factors. As a result the near-tip stresses have the same form as that for a homogeneous material. It can also be shown that the near-tip displacements take the same form as that for homogeneous materials, and this is independent of material gradients and the orientation of the crack. For plane stress and plane strain problems, they are of the form:

$$u_i = \frac{K_I}{2E'(0)}\sqrt{\frac{r}{2\pi}}u^{I}_i(\theta) + \frac{K_{II}}{2E'(0)}\sqrt{\frac{r}{2\pi}}u^{II}_i(\theta), \tag{2}$$

where $E'(0)$ is the Young's modulus at the crack tip, and the angular functions, $u^{I}_i(\theta)$ and $u^{II}_i(\theta)$, are the same as those for homogeneous materials.

Having the near tip stress and displacement fields, the energy release rate of the crack tip is obtained as

$$\mathcal{G} = \frac{K_I^2}{E'(0)} + \frac{K_{II}^2}{E'(0)} + \frac{K_{III}^2}{2\mu(0)}. \tag{3}$$

Here, $\mu(0)$ is the shear modulus at the crack tip. The above equation is again independent

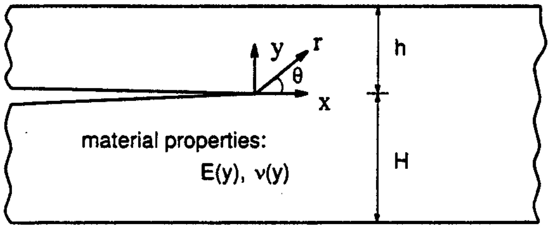

Fig. 1. A crack in a FGM which has continuous variation of material properties.

of the form for the material properties and the orientation of the crack, and has the same form as that for homogeneous materials. The path-independence of the J integral (Rice, 1968) holds if the crack is perpendicular to the direction along which material properties change; this is implied in Rice's original proof for homogeneous materials. Using the near tip fields obtained above, it can be shown that the J integral is equal to the energy release rate for the crack perpendicular to the direction along which material properties change.

For in-plane problems, the complex stress intensity $K = K_I + iK_{II}$ for FGMs has the following generic form

$$K = |K| e^{i\psi}, \tag{4}$$

where

$$\psi = \tan^{-1}\frac{K_{II}}{K_I} \tag{5}$$

is the phase angle of the complex stress intensity factor. The phase angle measures mode mixity, i.e., the proportion of the shear traction to the normal traction ahead of the crack tip, since

$$\psi = \tan^{-1}\left(\frac{\sigma_{xy}}{\sigma_{yy}}\right)_{\theta=0, r\to 0}. \tag{6}$$

The complex stress intensity has the following dimensional form:

$$K = TL^{1/2}Y, \tag{7}$$

where T is a representative stress magnitude, L is a characteristic length and Y is a dimensionless function which relates to the geometry of the problem and material properties. Both the phase angle and the dimensional form are consistent with those for homogeneous materials.

3. MODELING OF CRACK DEFLECTION

A number of studies have been performed for crack deflection in homogeneous materials and bimaterials with interface cracks. Before discussing the model for FGMs, we give a brief review of some results for homogeneous materials and bimaterials in Section 3.1 and 3.2, respectively. Since the interest is crack extension initiation, we concentrate on small kinks, where the kink length is much less than the length of the pre-existing cracks (main cracks).

3.1. *Homogeneous materials*

Stress intensity factors at the kinked crack tip uniquely characterize its near-tip fields; therefore, they are the parameters to determine the deflection direction at the load when the crack starts to propagate. The stress intensity factors for the kinked crack in a homogeneous material have been solved for elsewhere, including Palaniswamy and Knauss (1978) and Lo (1978). The latter detailed a method for solving crack kinking problems using integral equations which are formulated by the continuous distribution of dislocations: a method valid for both finite and infinitesimal (small) kinks. The idea is essentially to remove the tractions which are caused by the stress field of the main crack in the kinked crack before kinking. For the infinitesimal kink, since the kink length is much smaller than the size of the K-dominance zone of the main crack, the loading is the two stress intensity factors, K_I and K_{II}, of the main crack, and the stress intensity factors of the kinked crack, K_I^* and K_{II}^*, are obtained in terms of K_I and K_{II}. This is the asymptotic problem: a semi-infinite crack in the homogeneous material which is loaded by the K-field of the main crack characterized by K_I and K_{II}; the propagation of the main crack is controlled by its K-field. At large distances from the semi-infinite crack tip, the stress field approaches the K-field of the main crack. Near the semi-infinite crack tip, the stress field is perturbed from the K-field of the main crack because of the kinking. By dimensional analysis and linearity, the stress intensity factors of the kinked crack are expressed as

$$\begin{aligned} K_I^* &= C_{11}(\phi)K_I + C_{12}(\phi)K_{II}, \\ K_{II}^* &= C_{21}(\phi)K_I + C_{22}(\phi)K_{II}, \end{aligned} \tag{8}$$

where ϕ is the angle between the kink direction and the main crack, and C_{11}, C_{12}, C_{21} and C_{22} are coefficients which can be determined by Lo's method. For finite kinks, K_I^* and K_{II}^* must be obtained by solving a full boundary value problem considering the load, the geometry of the specimen including both the main crack length and the kink length.

If there is only mode I loading, the crack would extend along the direction of the pre-existing crack. This direction is the direction of maximum energy release rate. For mixed mode problems, the two often used criteria are the maximum energy release rate criterion (Cotterell, 1965) and mode I type criterion (also referred to as local symmetry criterion, see Cotterell and Rice (1980) and Goldstein and Salganik (1974)). The former states that the crack propagates along the direction of maximum energy release rate, and the latter that the crack grows along the direction for which the mode II stress intensity factor vanishes. Kink directions determined by the two criteria are consistent: it was shown that the difference is less than 1 degree for almost all loading combinations except the case in which the shear mode is overwhelmingly dominant where the difference is then about 2 degrees (He and Hutchinson, 1989).

For small ϕ, using first order approximation, Cotterell and Rice (1980) were able to analytically evaluate those coefficients in (8) as

$$\begin{aligned} C_{11} &= \frac{1}{4}\left(3\cos\frac{\phi}{2} + \cos\frac{3\phi}{2}\right), \\ C_{12} &= -\frac{3}{4}\left(\sin\frac{\phi}{2} + \sin\frac{3\phi}{2}\right), \\ C_{21} &= \frac{1}{4}\left(\sin\frac{\phi}{2} + \sin\frac{3\phi}{2}\right), \\ C_{22} &= \frac{1}{4}\left(\cos\frac{\phi}{2} + 3\cos\frac{3\phi}{2}\right). \end{aligned} \tag{9}$$

They showed that stress intensity factors calculated by using (9) are in good agreement with those exact solutions for ϕ up to 40 degrees: the error is less than 5%. They also showed that, by substituting the approximation (9) into (8), the energy release rate is locally a maximum for the mode I path (the path with a vanished mode II stress intensity factor).

3.2. *Bimaterials with interface cracks*

For an interface crack, stresses have an oscillatory singularity, and both stress intensity factors and angular functions involve Dundurs' parameters, i.e.,

$$\sigma_{ij} = \frac{\mathrm{Re}(Kr^{i\varepsilon})}{\sqrt{2\pi r}}\bar{\sigma}_{ij}^{I}(\theta,\varepsilon) + \frac{\mathrm{Im}(Kr^{i\varepsilon})}{\sqrt{2\pi r}}\bar{\sigma}_{ij}^{II}(\theta,\varepsilon) + \frac{K_{III}}{\sqrt{2\pi r}}\bar{\sigma}_{ij}^{III}(\theta), \tag{10}$$

where $K = K_I + iK_{II}$, and

$$\varepsilon = \frac{1}{2\pi} \ln \frac{1-\beta}{1+\beta}. \tag{11}$$

In (10), β is one of the two Dundurs' parameters. The Dundurs' parameters (Dundurs, 1969), α and β, are defined as

$$\alpha = \frac{\mu_1(\kappa_2+1)-\mu_2(\kappa_1+1)}{\mu_1(\kappa_2+1)+\mu_2(\kappa_1+1)},$$

$$\beta = \frac{\mu_1(\kappa_2-1)-\mu_2(\kappa_1-1)}{\mu_1(\kappa_2+1)+\mu_2(\kappa_1+1)}, \tag{12}$$

where μ_1 and μ_2 are the shear moduli of the two bulk materials; $\kappa_i = 3-4\nu_i$ for plane strain and $\kappa_i = (3-\nu_i)/(1+\nu_i)$ for plane stress ($i = 1, 2$), with ν_1 and ν_2 being the Poisson's ratios of the two bulk materials. The complex stress intensity factor, K, has the dimensional form

$$K = TL^{1/2-i\varepsilon}Y, \tag{13}$$

where T is a representative stress magnitude, L is a characteristic length and Y is a dimensionless function which relates to the geometry of the problem and Dundurs' parameters.

For the interface crack kinking problem, the stress intensity factors of the kinked crack are not unique in the sense that they are dependent on the kink length. For small kinks, dimensional analysis and linearity give the relationship between the complex stress intensity factor of the kinked crack K^* and that of the interface crack K as

$$K^* = c(\phi, \alpha, \beta)Ka^{i\varepsilon} + \bar{d}(\phi, \alpha, \beta)\bar{K}a^{-i\varepsilon}, \tag{14}$$

where a is the kink length and ($^-$) denotes the conjugate of the complex variable. It is seen that only when $\beta = 0$ (i.e. $\varepsilon = 0$) K^* is independent of the kink length. A complete solution in this case was obtained by He and Hutchinson (1989) using the integral equation method. The kink length dependence case, $\beta \neq 0$, was studied by Mukai *et al.* (1990) and Geubelle and Knauss (1994). The results showed that K^* and the kink angle are strongly dependent on kink length for sufficiently large β. It was concluded by the latter that this is due to "rotational stress and deformation fields" (Symington, 1987) at the crack tip, which extended to a region far outside of the contact zone. They suggested that the kink length a should be viewed as a property of the bimaterial combination, and be determined by fitting experimental data.

Whether the interface crack stays on the interface or kinks into one of the bulk materials is decided by the ratio of the energy release rate for the crack to extend on the interface $\mathscr{G}_i$ to that for the crack to kink $\mathscr{G}_s$, and the ratio of the interfacial toughness Γ_i to the toughness of the bulk materials Γ_s. Kinking is thereby favored if

$$\frac{\mathscr{G}_s}{\mathscr{G}_i} > \frac{\Gamma_s}{\Gamma_i}. \tag{15}$$

3.3. *Functionally graded materials*

Crack propagation is the competition between the energy release rate and the toughness of the material. In order to address crack kinking in FGMs, we need to study both physical parameters.

The energy release rate of a kinked crack in a FGM depends on the geometry, the loading, and the material properties including material gradients. The exact solution for it has to be obtained from the solution of the full boundary value problem. For small kinks, the solution may be obtained in an asymptotic way similar to that outlined in Section 3.1. In Section 2, we have noted that crack tip fields for FGMs have the same forms as those

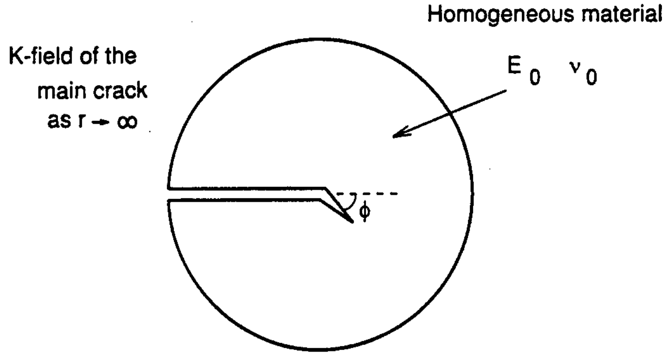

Fig. 2. Local homogenization near the crack tip region in a FGM: a homogeneous body is loaded far away from the tip of a semi-infinite crack by the K-field of the crack in the FGM (the asymptotic problem).

for homogeneous materials, and only the stress intensity factors are functions of material gradients. The elastic constants appeared in the displacement near-tip field and the energy release rate are those at the crack tip. This suggests that, to study crack kinking one can consider the asymptotic problem shown in Fig. 2: a homogeneous plate, which has a semi-infinite crack and the elastic constants at the main crack tip, is subjected to the loading characterized by the stress intensity factors of the main crack. The only difference between the asymptotic problem for FGMs and that for homogeneous materials is that here the elastic constants appearing in the problem are those at the main crack tip which change with its position, whereas for homogeneous materials those elastic constants do not change with the position of the main crack tip. Knowing the asymptotic problem, stress intensity factors of the kinked crack can be solved by the same technique to solve those for homogeneous materials. The local homogenization results in that the relationship (8) for homogeneous materials holds for FGMs. Specifically, the coefficients C_{ij} in (8) are the same as those for homogeneous materials, and material gradients affect the stress intensity factors of the kinked crack K^* only through the stress intensity factors of the main crack K. These coefficients can be obtained accurately by using the integral equation method to solve the asymptotic problem in Fig. 2, which is a homogeneous crack-kinking problem; as mentioned before, they are well approximated by the expressions in (9) for small ϕ.

The above approach for crack kinking is valid if the kink length is sufficiently smaller than the size of K-dominance zone. To examine the K-dominance zone, the asymptotic solution over the full field solution ahead of the crack tip, $\sigma^a_{yy}/\sigma^f_{yy}$, is plotted in Fig. 3 for the center cracked plate subjected to remote stress shown in Fig. 4(d), where $h/H = 1$. It is assumed that the width of the plate is much larger than the crack length. The crack is perpendicular to the direction of material property variation, and the variation is in the exponential form which is the same as that in Gu and Asaro (1997) and which will also be stated in the next section. It is seen that the size of the dominance zone decreases as γ, which is the measure of material gradients, increases. At 10% of the crack length ahead of

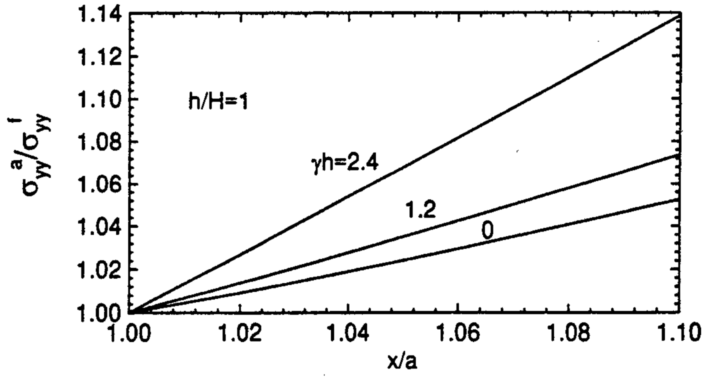

Fig. 3. Comparison of asymptotic solution with full field solution.

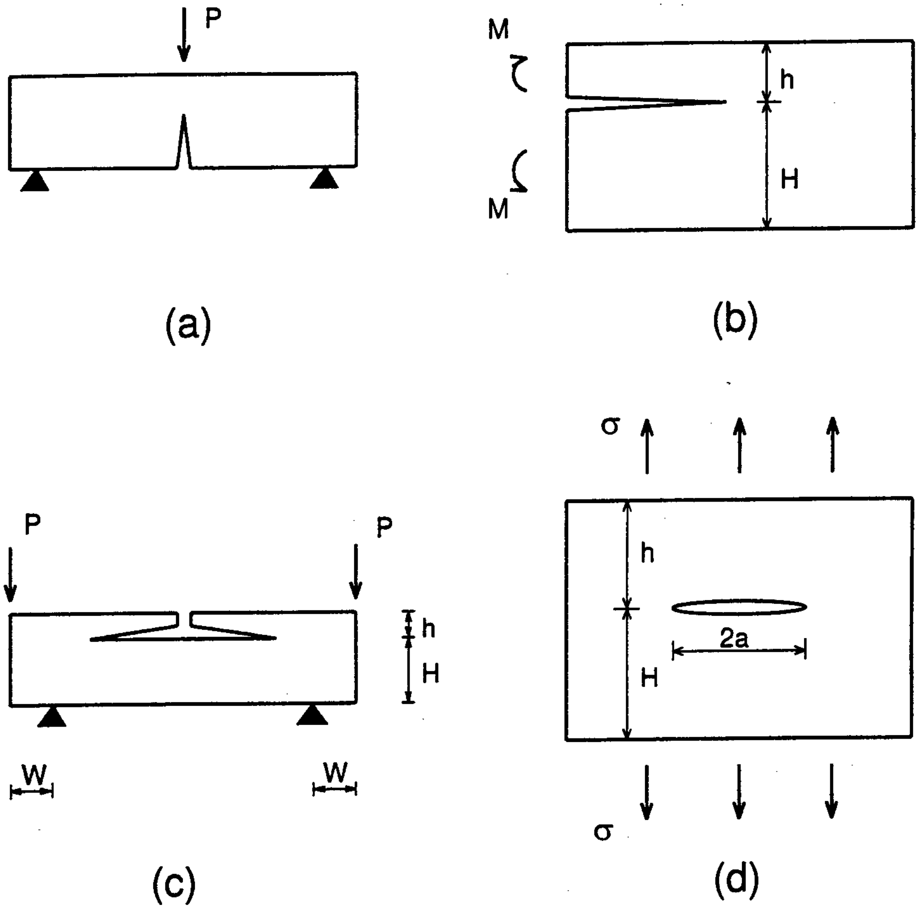

Fig. 4. Several Specimens. (a) Three-point bending specimen. (b) Double-cantilever beam. (c) Four-point bending specimen. (d) Center cracked plate. The material properties vary along the vertical direction.

the crack tip the error between the exact and asymptotic solutions for homogeneous materials is 5%, whereas it is 7% for $\gamma h = 1.2$, and 14% for $\gamma h = 2.4$. Note that, in the case of $\gamma h = 1.2$, the ratio of the Young's modulus at the upper boundary to that at the lower boundary is about 11. It is fair to say that, for material gradients which are not too large, the radius of K-dominance zone would be in the size comparable to that of homogeneous materials, at least, not reduced much from that of homogeneous materials. For interface cracks in bimaterials and sandwich structures, the size of the dominance zone was investigated by O'Dowd *et al.* (1992), Shih (1991) and Gu (1993).

The often used techniques to make FGMs are thermal spray, powder processing and chemical vapor deposition (CVD). The microstructure of these FGMs depends on these manufacturing processes (see Yamanouchi *et al.*, 1990; Holt *et al.*, 1993). For a real FGM, typical micrograph shows discrete structure. If the FGM is made of material phases A and B, the A-rich side has a dispersive structure with B particles in the A matrix; at the B-rich side A particles are in the B matrix; and in the middle region between the two sides, it is a skeletal structure due to the connectivity of both phases. For such complicated structure, the characterization of its toughness is an open issue at this moment. The toughness is likely a function of the position of the crack tip, and may also depend on the direction along which the crack propagates and the loading phase angle. In this study, we neglect the effect of microstructure; we study the idealized case, simply nonhomogeneous materials, i.e., the materials are those with a continuous change of material properties. This means that the microstructure of a FGM is sufficiently fine that the continuum model gives satisfactory predictions.

For the simply nonhomogeneous material, since we study small kink in the locally homogeneous body controlled by the K-field (the asymptotic problem shown in Fig. 2) and small-scale inelastic deformation around the crack tip, the toughness of the nonhomogeneous material is taken to be independent of direction at a fixed point. If the cohesive stress p, the inelastic stress in the cohesive zone ahead of the crack tip to restrain separation for creating free surfaces (Dugdale, 1960; Barenblatt, 1962) is not only a function of separation but also position, say $p(\delta, y)$, the toughness of the FGM at the position y may be expressed as

$$\Gamma = \int_0^{\delta_0} p(\delta, y)\,\mathrm{d}\delta, \tag{16}$$

where δ_0 is limit separation at y. This is the result of applying the J integral around the cohesive zone of the homogeneous body in Fig. 2 (see Rice, 1968).

For some FGMs, their micrograph may show layered structures, and these discrete microlayers have varying compositions and thus form the macroscopic material gradients along the thickness direction. If the crack lies on one of the interfaces, it may behave like a real interface crack. The mechanics of elastic interface fracture was established (Rice, 1988; Hutchinson, 1990). The criterion for an interface crack to grow on the interface is

$$\mathcal{G} = \Gamma(\psi), \tag{17}$$

where ψ is the phase angle. The condition for crack kinking into one of the two adjacent layers was stated in Section 3.2. Plastic interface fracture was investigated by Shih and Asaro (1988, 1989) and Shih (1991). In this study, since the FGM is considered as a simply nonhomogeneous material, the possibility of having discrete microlayers is excluded.

Considering the above, the kink direction for the FGM is the direction of maximum energy release rate or that in which the mode II stress intensity factor vanishes. Both directions relate to the geometry, loading and the material gradients. The two criteria for FGMs, like those for homogeneous materials, are also consistent, since they are built on locally homogeneous materials.

The locally homogenized model is expected to work well for brittle, simply nonhomogeneous materials, as discussed above. For those FGMs in which plastic mechanisms are involved in a sufficiently large region around the main crack tip, or microstructural gradients are presented at the tip region, further investigation is needed to determine these effects.

4. SOLUTIONS AND IMPLICATIONS

An immediate consequence of the present model is that, for the three point bending specimen shown in Fig. 4(a), the crack extends vertically ahead of the main crack tip along its direction, since the crack tip only has a mode I stress intensity factor (both geometry and loading are symmetric). The conclusion is independent of the form of the material property variation, and is the same as that in the case of a homogeneous material.

Stress intensity factors for the double-cantilever beam, Fig. 4(b), and the four-point bending specimen, Fig. 4(c), were obtained by Gu and Asaro (1997), where material properties were assumed to follow the exponential form:

$$E'(y) = E_0\,\mathrm{e}^{\gamma y},$$
$$\nu'(y) = \nu_0(1+\rho y)\,\mathrm{e}^{\gamma y}. \tag{18}$$

In (18), γ and ρ are material constants representing the material gradients; E_0 and ν_0 are the values of these elastic properties at $y = 0$. For plane stress problems, $E'(y) = E(y)$ and $\nu'(y) = \nu(y)$, where $E(y)$ and $\nu(y)$ are Young's modulus and Poisson's ratio, respectively; for plane strain problems, $E'(y) = E(y)/[1-\nu(y)^2]$ and $\nu'(y) = \nu(y)/[1-\nu(y)]$. The shear modulus, $\mu(y)$, relates to Young's modulus and Poisson's ratio by

$$\mu(y) = \frac{E'(y)}{2[1+\nu'(y)]}. \tag{19}$$

The above forms provide analytical flexibility and lead to somewhat simple forms for the field equations. Using (18) and (19), it is shown that for a traction boundary value problem, the stress field depends on the material parameter γ, which is related to the moduli at the upper boundary E'_u and at the lower boundary E'_l as

$$\gamma h = \frac{h}{L} \ln \frac{E'_u}{E'_l}. \tag{20}$$

In (20), $L = h+H$ is the thickness of the FGM and h a characteristic length. The parameter ρ in (18) does not affect the solution. When the modulus at the upper boundary is larger than that at the lower boundary, for example, the upper side is ceramic and the lower side is metal, the parameter γh is larger than zero; for the case of a homogeneous material, it is zero. We examine the kink direction in the double-cantilever beam and the four-point bending specimen.

For the double-cantilever beam, the energy release rate $\mathscr{G}$, normalized by $M/h^{1.5}$, is plotted vs the possible kink angle ϕ in Fig. 5, where ϕ is positive when the crack goes

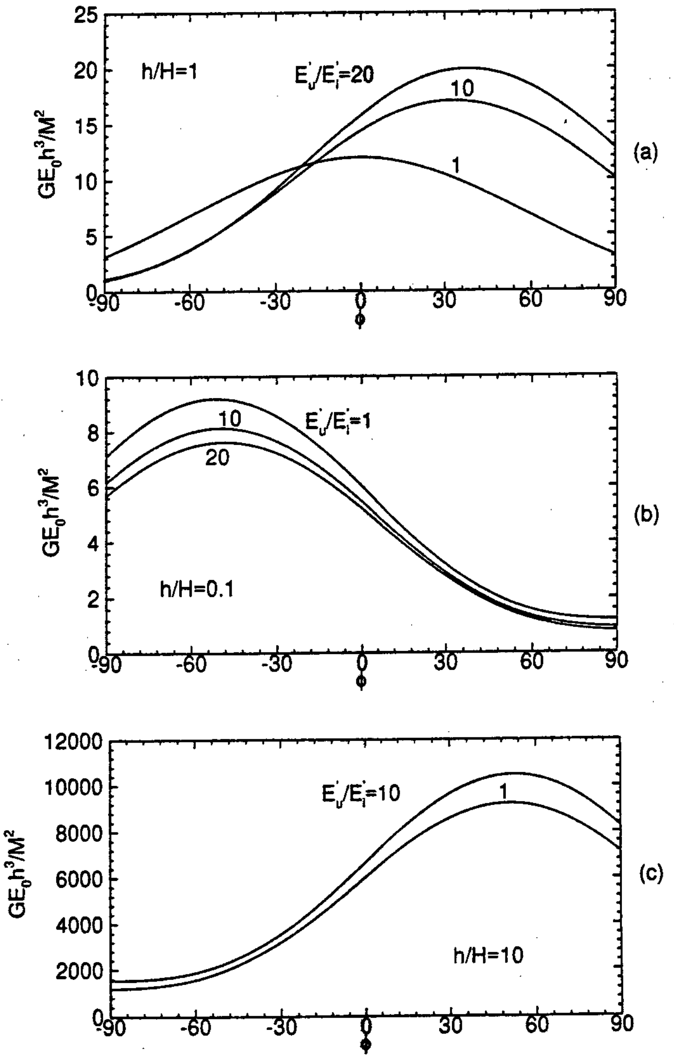

Fig. 5. The energy release rate for the double-cantilever beam for (a) $h/H = 1$, (b) $h/H = 0.1$ and (c) $h/H = 10$.

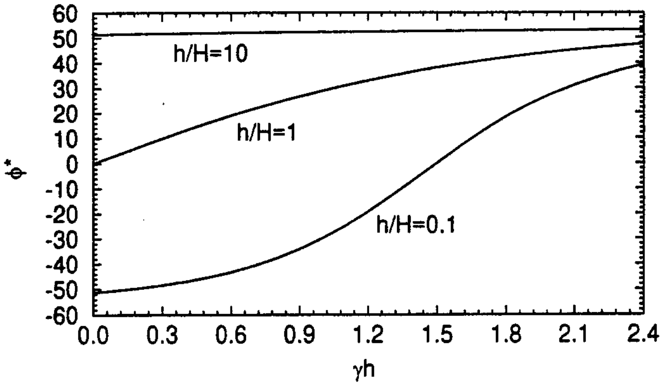

Fig. 6. Kink angle for the double-cantilever beam.

downwards (Fig. 2). When $h/H = 1$ (the crack is at the middle of the strip) and $h/H = 10$ (the crack is at the compliant side), the energy release rate is enhanced if $\phi > 0$; and it increases as the material gradient, measured by E'_u/E'_l, increases. When $h/H = 0.1$ (the crack is at the stiff side), the trend is different: the energy release rate is enhanced if $\phi < 0$; it decreases as the material gradient, E'_u/E'_l, increases. For some crack positions, the material gradient does have a strong effect on the energy release rate. For example, at $h/H = 1$, the maximum energy release rate for $E'_u/E'_l = 20$ is about 20, whereas it is 12 for the homogeneous case, $E'_u/E'_l = 1$. The implication of these qualitative behaviors is that when the crack is at the position where h/H is sufficiently large, the crack is kinked to the more compliant side, or downwards; when the crack is at the position where h/H is small, the crack is kinked to the stiffer side, or upwards. For the case of $h/H = 1$, the kink angle, the angle at which maximum energy release rate occurs, is 0° for homogeneous materials. This is a well known result, and is due to the symmetric loading and symmetric material properties in this case. It is also seen that, for the cases of $h/H = 1$ and $h/H = 10$, the kink angle increases as the material gradient increases. Kink angles for the three crack positions are plotted in Fig. 6. It shows that for small γ, the kink angles for the three crack positions are quite different, but as γ increases they become closer. When $h/H = 0.1$, the kink angle changes from negative sign to positive sign, i.e., upward kink becomes downward kink, at $\gamma h \approx 1.5$ as it increases. But at this crack position, it is seen from (20) that $E'_u/E'_l = 40$ for $\gamma h = 0.34$. This tells us that the portion of the curve where $\gamma h > 0.34$ is no practical use, since $E'_u/E'_l > 40$ in that portion and such large difference in elastic moduli may not appear in a FGM, at least, at the present time. It is noted that when the crack is at the middle position, the material gradient does have a strong effect on the kink angle, whereas it has little effect for the crack close to the upper and lower boundaries.

For the four-point bending specimen, it is assumed that the horizontal distance between the crack tip and the loading is large enough. As shown in Fig. 7, the maximum energy release rate is attained when ϕ is positive, and increases as the material gradient, E'_u/E'_l, increases for $h/H = 1$, 0.1 and 10. When $h/H = 0.1$ and 1, the increase of it is significant. For example, at $h/H = 0.1$, the energy release rate is 0.003 for the case of homogeneous materials, and 0.017 for $E'_u/E'_l = 20$; at $h/H = 1$, it is 8.41 and 20.02 for the two cases, respectively. Kink angles for the three crack positions are plotted vs the material gradient γh in Fig. 8. The figure shows, for the four-point bending specimen, γh does not have a strong effect on the kink angle. When the crack is at the middle of the beam, the difference of it between the case of a homogeneous material and that of $E'_u/E'_l = 20$ is less than 2°. When the crack is at $h/H = 0.1$ and 10 the difference is even less. In experiments, such small difference is difficult to be measured.

For the center cracked plate shown in Fig. 4(d), the energy release rate, besides h/H and γh, also varies with the crack length a/h. For the case of $a/h = 1$, kink angles are shown in Fig. 9. The trend of these curves is similar to that in Fig. 6 for the double-cantilever beam.

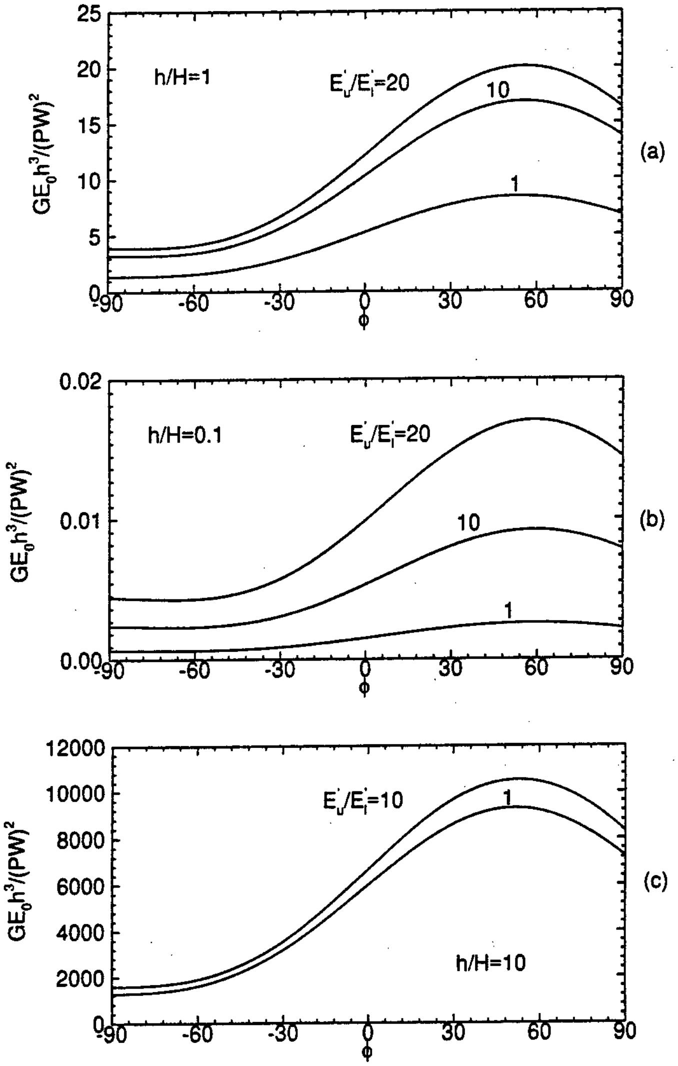

Fig. 7. The energy release rate for the four-point bending specimen for (a) $h/H = 1$, (b) $h/H = 0.1$ and (c) $h/H = 10$.

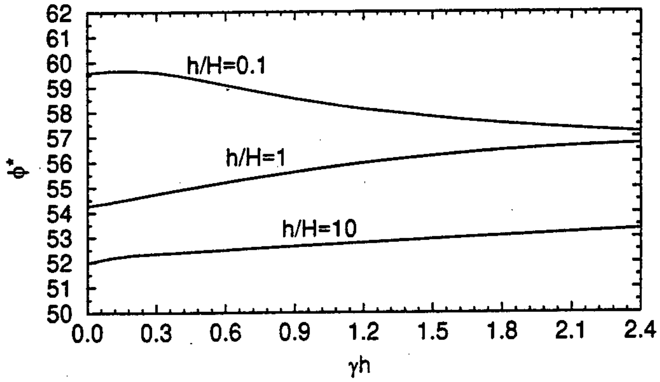

Fig. 8. Kink angle for the four-point bending specimen.

Two layers can be jointed by a compositionally graded material (FGM) sandwiched between them, as shown in Fig. 10. It reduces the mismatch of the bimaterial without the interlayer and gives better thermal-mechanical performance for the whole system (Giannakopoulos *et al.*, 1995). Also, for a bimaterial, the interface, the transition zone, is a FGM microscopically. For some bimaterials, the thickness of the zone is at the level that it may

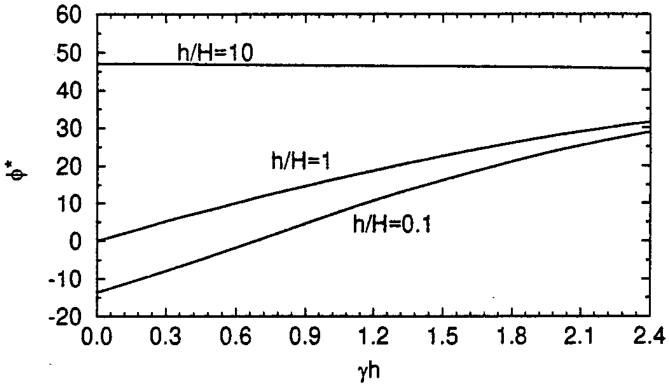

Fig. 9. Kink angle for the center cracked plate.

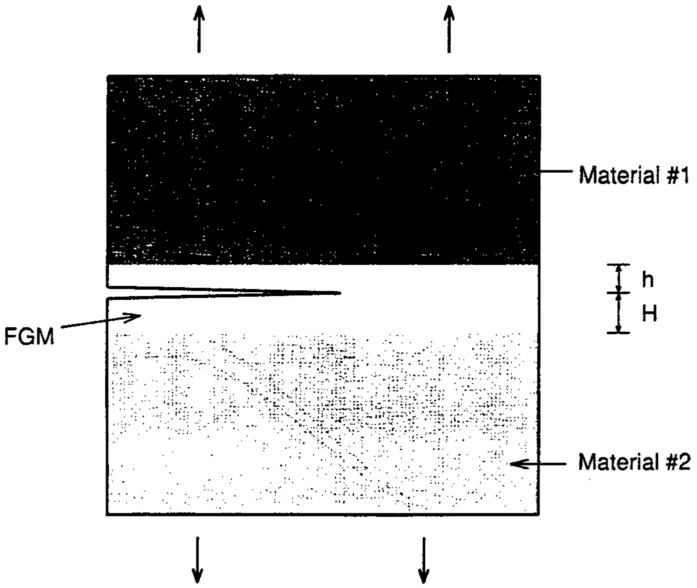

Fig. 10. A crack in a compositionally graded layer between two dissimilar materials.

not be neglected in analyzing the fracture of the interface. We use the above method to study the crack propagation inside the compositionally graded layer. The main crack shown in the above figure is parallel to the boundaries of the graded layer. The thicknesses of the two bulk materials are considered as much larger than the thickness of the interlayer. For a crack on a sharp interface, as discussed in Section 3.2, the energy release rate of the kinked crack is dependent on the extension length, and there is a contact zone in the region very close to the main crack tip due to its oscillatory singular field. The solution to the crack deflection problem in such case is not unique, except one of the two Dundurs' parameters, β, vanishes. It is seen that by introducing the transition zone to the interface the oscillatory singular field near the main crack tip, which is physically unacceptable, is removed, and therefore the problem of non-uniqueness for crack kinking does not exist.

The thickness of the graded layer and the position of the crack inside it are specified by h and H shown in Fig. 10. Here, since the thickness of the graded layer is considered much less than the length scale of the two bulk materials, the loading is represented by the complex stress intensity factor K^{∞} of the bimaterial problem without the graded layer. The complex stress intensity factor K of the crack inside the graded layer is expressed as

$$K = q\,\mathrm{e}^{i\omega}h^{i\varepsilon}K^{\infty}. \tag{21}$$

The equation is obtained by dimension analysis and linearity consideration. Both q and ω in above expression are functions of Dundurs' parameters, α and β, the position of the

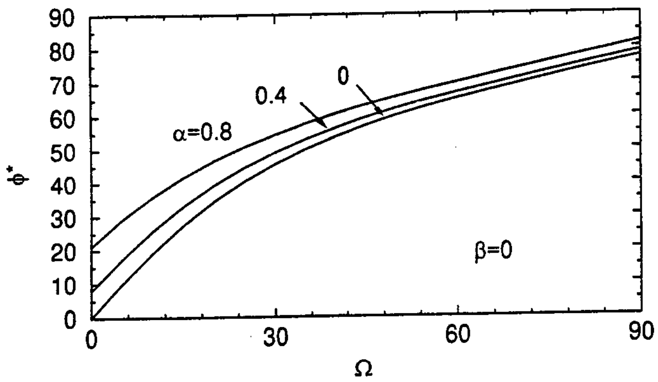

Fig. 11. The effect of α on kink angle for a crack inside the compositionally graded layer.

crack inside the graded layer, h/H, and the form of the material gradients. The former can be evaluated by using the J integral. For the case that the elastic modulus follows the exponential form given in (18) and Poisson's ratio is a constant,

$$q = \frac{\sqrt{1-\beta^2}}{(1+\alpha)^{h/2(h+H)}(1-\alpha)^{H/2(h+H)}}. \tag{22}$$

For $h/H = 1$, Yang and Shih (1994) gave a general expression to estimate ω for any form of material property variation in terms of a known bimaterial solution. They compared the results obtained from the approximation with those from finite element analyses, and it was concluded that the approximation was quite satisfactory. We use their expression to examine crack deflection in the graded layer for the case where $h/H = 1$ and material properties follow the above mentioned form. In Fig. 11, we plot the kink angle for $\alpha = 0$, 0.4 and 0.8, where $\beta = 0$ and

$$\Omega = \arctan\frac{\mathrm{Im}(K^{\alpha} h^{i\epsilon})}{\mathrm{Re}(K^{\alpha} h^{i\epsilon})}. \tag{23}$$

The effect of α on the kink angle is stronger for small Ω than for large Ω. In Fig. 12, we plot the kink angle for $\beta = 0$ and 0.2, where $\alpha = 0.4$. Since for many engineering materials β is less than 0.2 (see Suga *et al.*, 1988), the two figures show that β has a weaker effect on the kink angle than α. The results which are obtained from the linear variation of the material properties also support the observation.

The current study provides a means to assess crack deflection in a special set of FGMs, simply nonhomogeneous materials. From the above solutions, it is seen that material gradients do have a strong effect on the kink direction when a crack is at the central part of the FGMs. The solutions may be used in either testing the fracture behavior or measuring

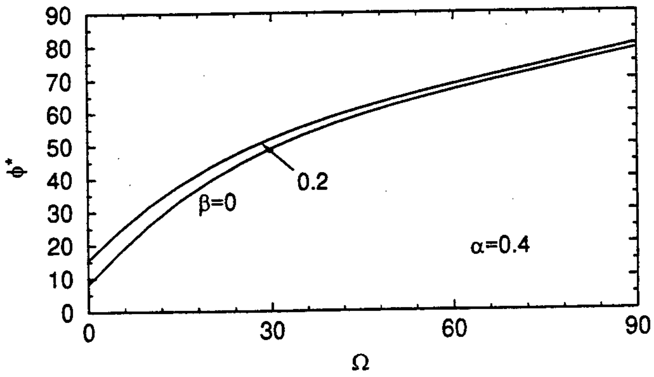

Fig. 12. The effect of β on kink angle for a crack inside the compositionally graded layer.

the toughness of FGMs. On the other hand, this study can be viewed as an initial effort for crack deflection in real FGMs: the effect of microstructure, i.e., the effect of local inhomogeneities around the crack tip on both the energy release rate and the toughness, is up for further investigation.

Acknowledgments—This work was supported by the Office of Naval Research through Grant N00014-93-1-1164.

REFERENCES

Barenblatt, G. I. (1962). The mathematical theory of equilibrium cracks in brittle fracture. *Advances in Applied Mechanics* **7**, 55–129.

Cotterell, B. (1965). On brittle fracture paths. *International Journal of Fracture* **1**, 96–103.

Cotterell, B. and Rice, J. R. (1980). Slightly curved or kinked cracks. *International Journal of Fracture* **16**, 155–169.

Dugdale, D. S. (1960). Yielding of steel sheets containing slits. *Journal of the Mechanics and Physics of Solids* **8**, 100–108.

Dundurs, J. (1969). Edge-bonded dissimilar orthogonal elastic wedges. *Journal of Applied Mechanics* **36**, 650–652.

Geubelle, P. H. and Knauss, W. G. (1994). Crack propagation at and near bimaterial interfaces: linear analysis. *Journal of Applied Mechanics* **61**, 560–566.

Giannakopoulos, A. E., Suresh, S., Finot, M. and Olsson, M. (1995). Elastoplastic analysis of thermal cycling: layered materials with compositional gradients. *Acta Metallurgica* **43**, 1335–1354.

Goldstein, R. V. and Salganik, R. L. (1974). Brittle fracture of solids with arbitrary cracks. *International Journal of Fracture* **10**, 507–523.

Gu, P. (1993). Multilayer material with an interface crack. *Journal of Applied Mechanics* **60**, 1052–1054.

Gu, P. and Asaro, R. J. (1997). Cracks in functionally graded materials. *International Journal of Solids and Structures* **34**, 1–17.

Gu, P. and Asaro, R. J. (1996). Plastic crack problems in functionally graded materials. Work in progress.

He, M.-Y. and Hutchinson, J. W. (1989). Kinking of a crack out of an interface. *Journal of Applied Mechanics* **56**, 270–278.

Holt, J. B., Koizumi, M., Hirai, T. and Munir, Z. A. (eds) (1993). *Ceramic Transactions* vol. 34, The American Ceramic Society, Westerville, Ohio.

Hutchinson, J. W. (1990). Mixed mode fracture mechanics of interfaces. In *Metal-Ceramic Interfaces, Acta-Scripta Metall. Proc.* Vol. 4, Pergamon, New York, pp. 295–306.

Lo, K. K. (1978). Analysis of branched cracks. *Journal of Applied Mechanics* **45**, 797–802.

Mukai, D. J., Ballarini, R. and Miller, G. R. (1990). Analysis of branched interface cracks. *Journal of Applied Mechanics* **57**, 887–893.

O'Dowd, N. P., Shih, C. F. and Stout, M. G. (1992). Test geometries for measuring interfacial fracture toughness. *International Journal of Solids and Structures* **29**, 571–589.

Palaniswamy, K. and Knauss, W. G. (1978). On the problem of crack extension in brittle solids under general loading. *Mechanics Today* Vol. 4, Pergamon, New York, pp. 87–148.

Rice, J. R. (1968). A path independent integral and approximate analysis of strain concentration by notches and cracks. *Journal of Applied Mechanics* **35**, 379–386.

Rice, J. R. (1988). Elastic fracture mechanics concepts for interfacial cracks. *Journal of Applied Mechanics* **55**, 98–103.

Shih, C. F. (1991). Cracks on bimaterial interfaces: elasticity and plasticity aspects. *Materials Science and Engineering* **A143**, 77–90.

Shih, C. F. and Asaro, R. J. (1988). Elastic-plastic analysis of cracks on bimaterial interfaces: part I—small scale yielding. *Journal of Applied Mechanics* **55**, 299–316.

Shih, C. F. and Asaro, R. J. (1989). Elastic-plastic analysis of cracks on bimaterial interfaces: part II—structure of small scale yielding fields. *Journal of Applied Mechanics* **56**, 763–779.

Suga, T., Elssner, E. and Schmander, S. (1988). Composite parameters and mechanical compatibility of material joints. *Journal of Computers and Materials* **22**, 917–934.

Symington, M. F. (1987). Eigenvalues for interface cracks in linear elasticity. *Journal of Applied Mechanics* **54**, 973–974.

Yamanouchi, M., Koizumi, M., Hirai, T. and Shiota, I. (eds) (1990). *Proceedings of the First International Symposium on Functionally Gradient Materials*, Sendai, Japan.

Yang, W. and Shih, C. F. (1994). Fracture along an interlayer. *International Journal of Solids and Structures* **31**, 985–1002.

Pergamon

Int. J. Solids Structures Vol. 34, No. 8, pp. 949–967, 1997
© 1997 Elsevier Science Ltd
Printed in Great Britain. All rights reserved
0020–7683/97 $17.00 + .00

PII: S0020–7683(96)00064–9

FAILURE OF A THIN FILM DUE TO INCLUSIONS ON THE INTERFACE

PEI GU†, WEI YANG‡, C. F. SHIH§ and R. J. ASARO†
† Department of Applied Mechanics and Engineering Sciences, Mail Code 0411,
University of California at San Diego, 9500 Cilman Drive, La Jolla, CA 92093-0411, U.S.A.
‡ Department of Engineering Mechanics, Tsinghua University, Beijing 100084, China
§ Division of Engineering, Brown University, Providence, RI 02912, U.S.A.

(*Received* 25 *October* 1995; *in revised form* 18 *April* 1996)

Abstract—This paper addresses failures near irregularities on the interface between a film and a substrate. Several boundary value problems, including two-dimensional and three-dimensional problems, involving inclusions of various shapes placed on the interface, are considered. The loading is induced by the lattice parameter mismatch between the film and substrate. Stresses near the interface and the inclusion boundary are of particular interest. The solutions show stress concentration around the inclusion boundary; in fact, a logarithmic singularity exists at the intersection of the inclusion, film and substrate. Emphasis is placed on identifying failures associated with high stresses near the inclusion. A theoretical prediction of the misfit strain to cause adhesion failure is obtained. The driving force for dislocation emission from the inclusion is calculated, and it is shown that dislocation emission from inclusions is favoured under a sufficiently large misfit strain. © 1997, Elsevier Science Ltd. All rights reserved.

1. INTRODUCTION

Thin films are widely used in electronic components and other advanced devices. Because high residual strains in the films due to either thermal expansion coefficient mismatch or lattice parameter mismatch between the films and substrates can cause device failures related to dislocation nucleation and interfacial cracking, the study of these mechanisms is a subject of interest. Many works addressing such problems can be found in the open literature. Examples of recent development include solutions to a large number of interfacial cracking problems by Hutchinson and Suo (1991), a detailed treatment for threading dislocations in the thin films by Freund (1993), and solutions to various stress-related problems in silicon technology, including film-edge induced stresses and dislocation generation in substrate due to these stresses, by Hu (1991).

The interfacial microstructure of a film/substrate system controls the performance of the system in more ways than one. It appears that this aspect has been overlooked by many. Recent experiments (Perovic *et al.*, 1989) have shown that β-SiC precipitates are formed on the interface between the Ge_xSi_{1-x} layer and Si substrate by molecular beam epitaxy, and dislocations emit from these precipitates when a critical particle size is reached. Also, it is possible that the surface of the substrate is not a perfect plane, i.e., there are irregularities on the substrate. Inclusions on the interface are sources of stress concentration, and therefore are the possible sites for failure initiation. Besides dislocation nucleation, adhesion failure occurs if stresses on the interface exceed its adhesion strength. In this paper, we examine the stress concentration near these inclusions, and attempt to identify failures resulting from these high stresses. For this purpose, an inclusion on the interface between a thin film and substrate is considered, and the loading arises from the lattice parameter mismatch between the film and substrate. In this study, we take the inclusion, film and substrate as elastically deforming bodies, i.e., the problem is solved by elasticity theory. The inclusion can be regarded as a local inhomogeneity. So, it is assumed that both the thickness of the film and the substrate are much larger than the size of the inclusion. Under these assumptions, we are able to obtain several analytical solutions for two-dimensional and three-dimensional inclusion problems.

The plan of this paper is as follows. In Section 2, the two-dimensional problem, an elliptical inclusion on the interface between a film and substrate, is analyzed. This idealized case admits an analytical solution with a relatively simple form which is obtained by complex variable method. In Section 3, the stresses on the interface between the film and substrate for the two-dimensional problem are examined. It is shown that high stresses are generated near the inclusion; in fact, the shear stress has a logarithmic singularity at the intersection of the inclusion, film and substrate. A theoretical prediction for the misfit strain to cause adhesion failure is obtained. Section 4 addresses the bending effect due to the misfit strain. The three-dimensional problem is solved in Section 5. Section 6 discusses dislocation emission from the inclusion, where the driving force for dislocation emission is derived, and it is shown that dislocation emission is favored for a sufficiently large misfit strain.

2. TWO-DIMENSIONAL PROBLEM: AN ELLIPTICAL INCLUSION

The mathematical problem shown in Fig. 1 is a film of thickness h bonded to the surface of a substrate. At the origin, there is an elliptical inclusion on the interface between the film and substrate. The major and minor axes are a and b, respectively. The film has a lattice parameter α_f, which differs from that of the substrate and inclusion, α_s. The inclusion and the substrate could have different lattice parameters, but this possibility is not considered here. The interface between film and substrate and the interface between film and inclusion are assumed to be coherent, so that a stress field is induced in the film, substrate and inclusion. Far away from the inclusion, its solution is known: the substrate is stress free and the film is subjected to biaxial uniform tension or compression

$$\sigma_0 = \frac{2\mu_1(1+\nu_1)}{1-\nu_1}\varepsilon_0, \tag{1}$$

where

$$\varepsilon_0 = \frac{\alpha_s-\alpha_f}{\alpha_f}. \tag{2}$$

Both the film and substrate have shear modulus μ_1 and Poisson's ratio ν_1, while these elastic constants for the inclusion are μ_2 and ν_2. For the semiconductor layered systems, the difference in elastic properties between the film and substrate is usually small; it is neglected here. As stated in the introduction, the film thickness is much larger than the inclusion size.

To solve the boundary value problem, one must match lattice parameters across the interfaces between the film and substrate and between the film and inclusion. On the interface between the film and substrate, there is a lattice parameter mismatch in the x and z directions (the z axis is perpendicular to the x and y axes shown in Fig. 1); but on the interface between the film and inclusion, there is a lattice parameter mismatch in all three directions, x, y and z. The solution to the three-dimensional problem can be obtained by considering two two-dimensional problems using an Eshelby-type superposition, as shown

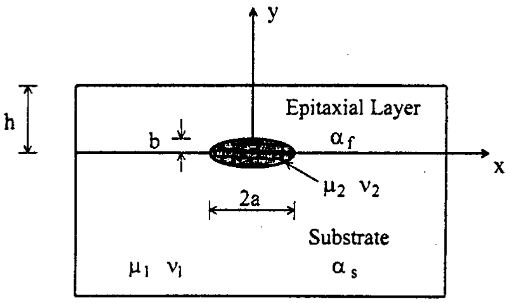

Fig. 1. A elliptical inclusion on the interface between a film and substrate.

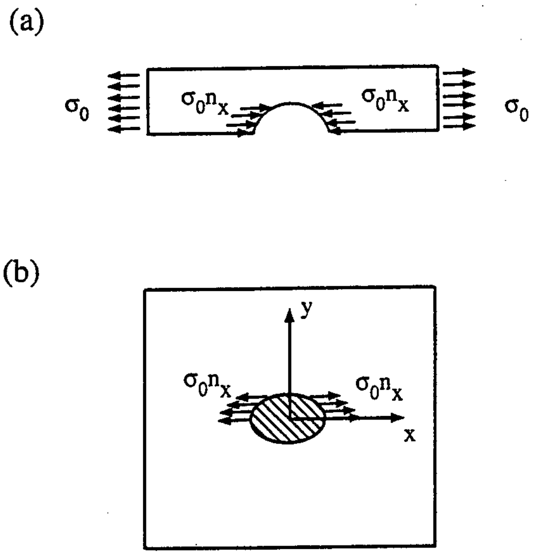

Fig. 2. A superposition scheme for solving lattice parameter mismatch problem.

in Fig. 2. First, we match the lattice parameters on both interfaces in the x and z directions, stretching the film by ε_0 in the x and z directions. The state of stress induced by this process is a uniform biaxial stress, $\sigma_{xx} = \sigma_{zz} = \sigma_0$. Next, a distribution of traction is applied to the interface between the film and inclusion so as to free it from stress, Fig. 2(b). In this cut and paste process, we have neglected the effect of Poisson's ratio. The stretch of the film induced a strain $\varepsilon_{yy} = -2\nu_1/(1-\nu_1)\varepsilon_0$; this strain reduces the lattice parameter in the y direction of the film. We have also neglected the difference in the lattice parameters in the y direction. These effects may be neglected if both the film and the substrate have the same lattice parameter in the y direction and the Poisson's ratio of the film is very small. We first solve the problem shown in Fig. 2(b), then the problem for the mismatch in the y direction.

The problem shown in Fig. 2(b) may be solved using the complex variable method (Muskhelishvili, 1953). Stress and displacement fields are generated by complex potentials $\phi(\xi)$ and $\psi(\xi)$ such that:

$$\begin{aligned} \sigma_{xx}+\sigma_{yy} &= 2[\phi'(\xi)+\overline{\phi'(\xi)}], \\ \sigma_{yy}-\sigma_{xx}+2\mathrm{i}\sigma_{xy} &= 2[\bar{\xi}\phi''(\xi)+\psi'(\xi)], \\ 2\mu(u+\mathrm{i}v) &= \kappa\phi(\xi)-\xi\overline{\phi'(\xi)}-\overline{\psi(\xi)}, \end{aligned} \tag{3}$$

where $\xi = x+\mathrm{i}y$; $\kappa = 3-4\nu$ for plane strain; $\kappa = (3-\nu)/(1+\nu)$ for plane stress. The resultant force along the arc from $\xi = \xi_1$ to $\xi = \xi_2$ can be expressed as

$$F_x+\mathrm{i}F_y = -\mathrm{i}[\phi(\xi)+\xi\overline{\phi'(\xi)}+\overline{\psi(\xi)}]|_{\xi=\xi_1}^{\xi=\xi_2}. \tag{4}$$

The resultant force due to the traction acting on the inclusion boundary between $\xi = a$ and $\xi = \xi_0$ in Fig. 2(b) is

$$f(\xi_0) = \begin{cases} -\mathrm{i}\dfrac{\mu_1(1+\nu_1)}{1-\nu_1}\varepsilon_0(\xi_0-\bar{\xi}_0) & \mathrm{Im}\xi_0 \geqslant 0 \\ 0 & \mathrm{Im}\xi_0 < 0. \end{cases} \tag{5}$$

Using a conformal mapping, $\xi = R(\zeta+m/\zeta)$ with $R = (a+b)/2$ and $m = (a-b)/(a+b)$, the elliptical inclusion is mapped onto a unit circle. Then, continuity conditions on the interface between the inclusion and matrix (the film and substrate) can be written as

$$\frac{1}{2\mu_1}\left[\kappa_1\phi_1(\tau)-\frac{\tau^2+m}{\tau(1-m\tau^2)}\overline{\phi_1'(\tau)}-\psi_1(\tau)\right]-\frac{1}{2\mu_2}\left[\kappa_2\phi_2(\tau)-\frac{\tau^2+m}{\tau(1-m\tau^2)}\overline{\phi_2'(\tau)}-\psi_2(\tau)\right]=0,$$

$$\left[\phi_1(\tau)+\frac{\tau^2+m}{\tau(1-m\tau^2)}\overline{\phi_1'(\tau)}+\psi_1(\tau)\right]-\left[\phi_2(\tau)+\frac{\tau^2+m}{\tau(1-m\tau^2)}\overline{\phi_2'(\tau)}+\psi_2(\tau)\right]=g(\tau), \quad (6)$$

where

$$g(\tau)=\begin{cases}-C\left(\tau-\dfrac{1}{\tau}\right) & \operatorname{Im}\tau\geqslant 0\\ 0 & \operatorname{Im}\tau<0,\end{cases}$$

$$C=\frac{\mu_1(1+\nu_1)}{1-\nu_1}\varepsilon_0 R(1-m), \quad (7)$$

and $|\tau|=1$. Here, $\phi_1(\zeta)$ and $\psi_1(\zeta)$ are complex potentials defined for the matrix, and $\phi_2(\zeta)$ and $\psi_2(\zeta)$ are complex potentials defined for the inclusion.

The solution to the problem is the four potentials which satisfy (6). Also, $\phi_1(\zeta)$ and $\psi_1(\zeta)$ have to give a stress free state at $z=\infty$. The detailed procedure to solve the problem is given in the Appendix, and the solution to the elliptical inclusion is obtained in terms of series. For a circular inclusion, the solution is a simple finite-term solution, which is given by

$$\phi_1(\zeta)=\frac{1}{\Gamma\kappa_1+1}\frac{C}{2\pi\mathrm{i}}\left[-2+\frac{\mathrm{i}\pi}{\zeta}+\frac{\zeta^2-1}{\zeta}\log\frac{\zeta+1}{\zeta-1}\right],$$

$$\psi_1(\zeta)=-\frac{\kappa_2}{\Gamma+\kappa_2}\frac{C}{2\pi\mathrm{i}}\left[-2+\frac{\mathrm{i}\pi}{\zeta}+\frac{\zeta^2-1}{\zeta}\log\frac{\zeta+1}{\zeta-1}\right]-\phi_1'(\zeta)\frac{1}{\zeta}+A\frac{1}{\zeta}, \quad (8)$$

where

$$A=\frac{\Gamma(1+\kappa_2)}{(\Gamma+\kappa_2)(2\Gamma+\kappa_2-1)}\frac{C}{2}, \quad (9)$$

and $\Gamma=\mu_2/\mu_1$. We shall not write here the expressions for $\phi_2(\zeta)$ and $\psi_2(\zeta)$ since the stress fields in the film and substrate are our interest.

The solution for the elliptical inclusion can be obtained directly in following special cases: $\Gamma=0$, $\Gamma=1$, and $\Gamma=\infty$. For $\Gamma=\infty$ (rigid inclusion), the solution is $\phi_1(\zeta)=\phi_2(\zeta)=\psi_1(\zeta)=\psi_2(\zeta)=0$. When $\Gamma=1$, the problem corresponds to a traction $\sigma_0\,\mathrm{d}y/\mathrm{d}s$ ($\mathrm{d}s$ is the differential arc length of the boundary of the ellipse) acting on the upper boundary of the ellipse in a homogeneous body. Its solution can be readily obtained by integrating a point force solution over the upper boundary of the inclusion. Similarly, for $\Gamma=0$, the solution can be obtained by integrating a point force acting on the upper boundary of the elliptical hole.

A step irregularity on the substrate surface shown in Fig. 3 gives rise to a similar problem. As before, both the film and substrate have the same elastic properties; there is no lattice parameter mismatch in the y direction, and the Poisson's ratio of the film is very small. The solution to the problem is obtained by the integration of a point force solution over $0<y<a$ with the point force being $\sigma_0\,\mathrm{d}y$. The two potentials are given by

$$\phi_1(\xi)=\frac{\sigma_0}{2\pi\mathrm{i}(1+\kappa)}[(\xi-\mathrm{i}a)\log(\xi-\mathrm{i}a)-\xi\log\xi],$$

$$\psi_1(\xi)=-\frac{\kappa\sigma_0}{2\pi\mathrm{i}(1+\kappa)}[(\xi-\mathrm{i}a)\log(\xi-\mathrm{i}a)-\xi\log\xi]+\frac{\sigma_0}{2\pi\mathrm{i}(1+\kappa)}\xi[\log(\xi-\mathrm{i}a)-\log\xi]. \quad (10)$$

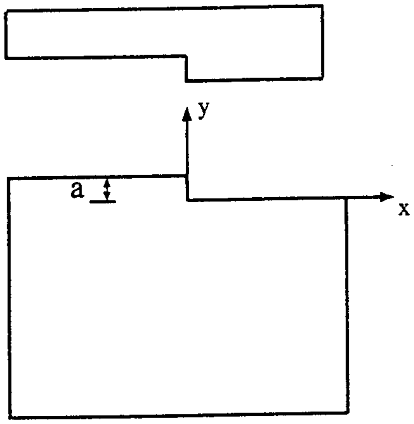

Fig. 3. A step irregularity.

We next solve the problem for the mismatch in the y direction. We view the problem as the one similar to Eshelby's internal problem, by assuming that there is a uniform eigenstrain in the upper half of the inclusion (the portion above the interface between the film and substrate) ε_{yy}^* due to the mismatch in the y direction. The eigenstrain is

$$\varepsilon_{yy}^* = \varepsilon_0\left(1+2\frac{\nu_1}{1-\nu_1}\right). \tag{11}$$

The term involving ν_1 represents the effect of the Poisson's ratio ν_1 in the cut and paste process discussed before, and the rest represents the effect of the difference in lattice parameters in the y direction. If there is no lattice parameter mismatch in the y direction,

$$\varepsilon_{yy}^* = 2\frac{\nu_1}{1-\nu_1}\varepsilon_0. \tag{12}$$

The mathematical problem can be formulated by the complex variable method, see List and Silberstein (1966). The continuity condition on the interface between the inclusion and the matrix is the same as (6), except in this case the right side of the first equation is $g(\tau)$ and that of the second equation is zero. Here,

$$g(\tau) = \begin{cases} \dfrac{\varepsilon_{yy}^*}{2}R(1-m)\left(\tau-\dfrac{1}{\tau}\right) & \mathrm{Im}\tau \geqslant 0 \\ 0 & \mathrm{Im}\tau < 0. \end{cases} \tag{13}$$

This shows that the problem can be solved in the similar way as that in the Appendix. The two potentials for a circular inclusion are given by

$$\phi_1(\zeta) = -\frac{\Gamma}{\Gamma\kappa_1+1}\frac{\mu_1\varepsilon_{yy}^*R}{2\pi i}\left[-2+\frac{i\pi}{\zeta}+\frac{\zeta^2-1}{\zeta}\log\frac{\zeta+1}{\zeta-1}\right],$$

$$\psi_1(\zeta) = -\frac{\Gamma}{\Gamma+\kappa_2}\frac{\mu_1\varepsilon_{yy}^*R}{2\pi i}\left[-2+\frac{i\pi}{\zeta}+\frac{\zeta^2-1}{\zeta}\log\frac{\zeta+1}{\zeta-1}\right]-\phi_1'(\zeta)\frac{1}{\zeta}+A_1\frac{1}{\zeta}, \tag{14}$$

where

$$A_1 = -\frac{\Gamma(1+\kappa_2)}{(\Gamma+\kappa_2)(2\Gamma+\kappa_2-1)}\frac{\mu_1\varepsilon_{yy}^*R}{2}. \tag{15}$$

Finally, we mention that the analysis for the mismatch in the y direction is the first order approximation since we assume a uniform eigenstrain in the inclusion; in the real case the eigenstrain appears to be more complicated.

3. STRESSES ON THE INTERFACE BETWEEN THE FILM AND SUBSTRATE

Having the solution in Section 2, we examine the stresses on the interface between the film and substrate near an inclusion. For the most part of this section, we assume that the film and the substrate have the same lattice parameter in the y direction and the Poisson's ratio of the film is small, so that the solution for the problem shown in Fig. 2(b) is a valid solution. For a circular inclusion, the shear stress on the interface is

$$\sigma_{xy}(\rho,0) = -\frac{\sigma_0}{4\pi}\frac{1}{1+\Gamma\kappa_1}\left(-\frac{6}{\rho^3}+\frac{3-\rho^2}{\rho^4}\log\frac{\rho+1}{\rho-1}\right) + \frac{\sigma_0}{4\pi}\frac{\kappa_2}{\Gamma+\kappa_2}\left(-\frac{2}{\rho}+\frac{1+\rho^2}{\rho^2}\log\frac{\rho+1}{\rho-1}\right), \quad (16)$$

where $\rho = x/a$, and is either greater than 1 or less than -1. It has a logarithmic singularity at the intersection of the film, substrate and inclusion, $\rho = \pm 1$. The singular term is

$$\sigma_{xy}(\rho,0) = \frac{\sigma_0}{2\pi}\left(\frac{\kappa_2}{\Gamma+\kappa_2}-\frac{1}{1+\Gamma\kappa_1}\right)\log\frac{\rho+1}{\rho-1} \quad (17)$$

as $\rho \to \pm 1$. The expression before the logarithmic function in the above expression is a logarithmic stress intensity factor, which varies with Γ, κ_1 and κ_2. For fixed $\kappa_1 = \kappa_2 = 2.6$ (plane strain with $v_1 = v_2 = 0.1$), the logarithmic stress intensity factor is the largest when $\Gamma = 1$, and it vanishes when $\Gamma = 0$ (hole) and $\Gamma = \infty$ (rigid inclusion). The singularity is so weak that its zone of dominance is very small. This can be seen from Fig. 4, where (16) is plotted for several Γ's. In this figure, the shear stress for $\Gamma = 0$ is larger than the shear stress for $\Gamma = 1$ except the very small portion near $\rho = 1$. Also, the shear stress decreases quickly to zero, and its effective zone is about 3–4 times the size of the inclusion.

To examine the geometrical influence of the inclusion, the shear stress caused by an elliptical inclusion is plotted in Fig. 5 for several values of b/a, where we choose $\Gamma = 1$ and $\kappa_1 = \kappa_2 = 2.6$ (plane strain with $v_1 = v_2 = 0.1$). It shows that σ_{xy} increases as b/a increases. This is because the mismatch increases as b/a increases. Also, the shear stress decays more quickly for smaller b/a.

An inclusion on the interface between the film and substrate can generate high shear stress. When the inclusion and matrix have the same elastic properties, $\Gamma = 1$ and $\kappa_1 = \kappa_2 = 2.6$ (plane strain with $v_1 = v_2 = 0.1$), the shear stress at a distance $0.1a$ ahead of

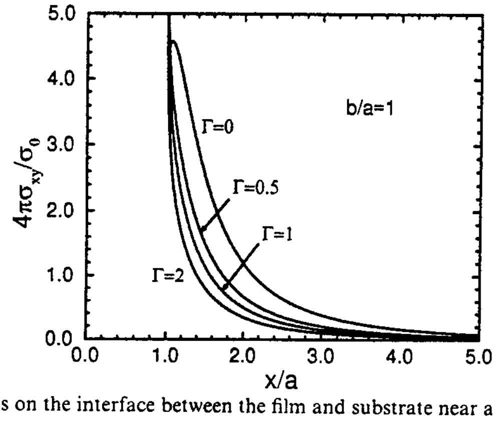

Fig. 4. Shear stress on the interface between the film and substrate near a circular inclusion.

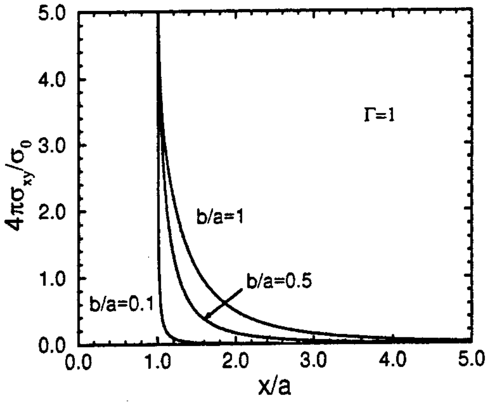

Fig. 5. The effect of inclusion geometry on shear stress.

the inclusion (the shear stress is singular at the intersection of the film, substrate and inclusion) is

$$\sigma_{xy} = 0.23\sigma_0 \tag{18}$$

for a circular inclusion. Consider growing a GaAs film on Si substrate, and neglect the difference in elastic properties between GaAs and Si. For these materials, $\varepsilon_0 = -0.04$ and $E_{\mathrm{GaAs}} = 85$ GPa. Then, (18) gives $\sigma_{xy} = -0.9$ GPa.

Near a circular inclusion, the normal stress on the interface between the film and substrate is

$$\sigma_{yy}(\rho, 0) = \frac{\sigma_0}{4}\frac{\kappa_2 - 1}{2\Gamma + \kappa_2 - 1}\frac{1}{\rho^2} - \frac{3\sigma_0}{4}\frac{1}{1 + \Gamma\kappa_1}\frac{1}{\rho^4}, \tag{19}$$

where $\rho = x/a$, and is either greater than 1 or less than -1. We note that it does not have a singularity as does σ_{xy}. For $\Gamma = 1$ and $\kappa_1 = \kappa_2 = 2.6$ (plane strain with $\nu_1 = \nu_2 = 0.1$), the maximum normal stress which occurs at $\rho = \pm 1$ is

$$\sigma_{yy} = -0.1\sigma_0. \tag{20}$$

If $\varepsilon_0 < 0$, the normal stress is a peeling stress. The above expression shows that a large compressive residual strain gives a large peeling stress on the interface, which is a driving force for adhesion failure of the interface. If $\varepsilon_0 > 0$, it is a compressive stress. For the GaAs/Si example, the maximum peeling stress is 0.4 GPa. Figure 6 shows σ_{yy} vs ρ for several values of Γ.

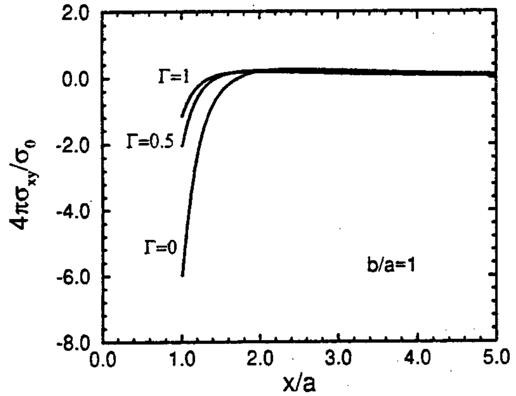

Fig. 6. Normal stress on the interface between the film and substrate near a circular inclusion.

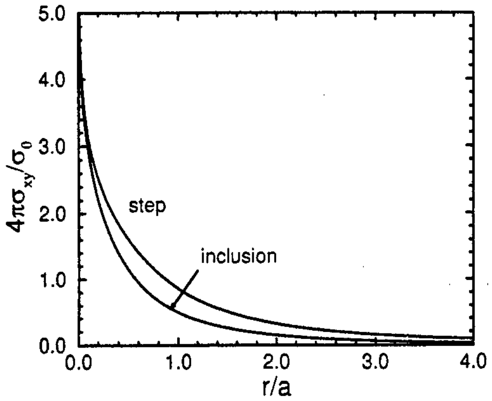

Fig. 7. Comparison of shear stresses near a circular inclusion and near a step irregularity, on the interface between the film and substrate.

Near a step irregularity, the shear stress on the interface between the film and substrate is

$$\sigma_{xy}(\rho, 0) = \frac{\sigma_0}{\pi(1+\kappa)}\left[\frac{1}{\rho^2+1} - \frac{1-\kappa}{4}\log\left(1+\frac{1}{\rho^2}\right)\right], \tag{21}$$

where $\rho = x/a$, and $\rho > 0$. The shear stresses on the interface near a step irregularity and near a circular inclusion are compared in Fig. 7. As expected, it shows that the step irregularity produces larger shear stress on the interface.

If there are no inclusions and step irregularities on the interface, there are no stresses acting on the interface. Therefore, adhesion failure may not occur. If the residual strain ε_0 in the thin film causes adhesion failure due to inclusions or step irregularities, we estimate it from above solutions. Suppose that the interfacial adhesion strength, i.e., the summation of all atomic bonding forces between the adjoining material surfaces for an ideal planar interface, is known, and let the critical normal stress be σ_b and the critical shear stress be τ_b. Then, from (18) and (20), the mismatch stress σ_0 to cause adhesion failure is given by the smaller of

$$|\sigma_0| = 4.35\tau_b,$$

$$|\sigma_0| = 10\sigma_b, \tag{22}$$

for compressive σ_0. For tensile σ_0, this prediction is

$$\sigma_0 = 4.35\tau_b. \tag{23}$$

In writing (22) and (23), we have assumed that adhesion failure caused by shear occurs at a distance $0.1a$ ahead of the inclusion. Besides calculating atomic bonding forces, the interface adhesion strength can be measured by a number of methods which have been discussed in Alexopoulos and O'Sullivan (1990). Due to the difficulty in handling these tests, the data obtained by these methods are usually considered to be qualitative in nature.

It is seen that either a large residual strain or poor interface bonding could lead to adhesion failure. In the GaAs/Si example discussed above, the film is subjected to compressive residual stress and the normal stress on the interface is a peeling stress. If we assume that the failure mode is the adhesion failure by the peeling stress, the criterion predicts that the adhesion failure occurs if σ_b is less than 0.4 GPa. The development of the initial failure could lead to large scale fracture, such as film buckling. The mechanics of film buckling has been studied by Evans and Hutchinson (1984), and the cracking and buckling processes of a film/substrate system have been characterized in terms of the behavior of the film and substrate, and the interface bonding by Evans *et al.* (1988).

The effect of the mismatch in the y direction can be estimated using the solution for a circular inclusion given by (14) and (15). The shear stress on the interface between the film and substrate near the inclusion is

$$\sigma_{xy}(\rho,0)=\frac{\mu_1\varepsilon_{yy}^*}{2\pi}\frac{\Gamma}{1+\Gamma\kappa_1}\left(-\frac{6}{\rho^3}+\frac{3-\rho^2}{\rho^4}\log\frac{\rho+1}{\rho-1}\right)$$

$$+\frac{\mu_1\varepsilon_{yy}^*}{2\pi}\frac{\Gamma}{\Gamma+\kappa_2}\left(-\frac{2}{\rho}+\frac{1+\rho^2}{\rho^2}\log\frac{\rho+1}{\rho-1}\right), \qquad (24)$$

where $\rho = x/a$, and is either greater than 1 or less than -1; the normal stress is

$$\sigma_{yy}(\rho,0)=\mu_1\varepsilon_{yy}^*\frac{\Gamma}{2\Gamma+\kappa_2-1}\frac{1}{\rho^2}+\frac{3\mu_1\varepsilon_{yy}^*}{2}\frac{\Gamma}{1+\Gamma\kappa_1}\frac{1}{\rho^4}. \qquad (25)$$

We examine the effect of the Poisson's ratio using (12) for ε_{yy}^*. Since the stresses are proportional to the Poisson's ratio ν_1, they can be neglected if the Poisson's ratio is small. The larger the Poisson's ratio, the larger its effect on the stress field. Few numerical examples for the stresses are given below when ν_1 is small, by taking $\Gamma = 1$ and $\kappa_1 = \kappa_2$. At $\rho = 1$, the normal stress is 0.006 σ_0 for $\nu_1 = 0.01$, and 0.06 σ_0 for $\nu_1 = 0.1$. At $\rho = 1.1$, the shear stress is 0.001 σ_0 for $\nu_1 = 0.01$, and 0.01 σ_0 for $\nu_1 = 0.1$. It appears that the normal stress is larger than the shear stress for the mismatch in the y direction.

4. BENDING EFFECT

If the film and substrate have finite thicknesses, the solution described in the preceding sections must be corrected. Four self-equilibrating bending moments are applied to the film and substrate, and two of them in the x-y plane are shown in Fig. 8. We assume the thickness of the substrate h_s is much larger than that of the film h, and the thickness of the film is much larger than the size of the inclusion $R = (a+b)/2$. The magnitude of these bending moments depends on the thicknesses of film and substrate, and is given by

$$M = \tfrac{1}{2}hh_s\sigma_0. \qquad (26)$$

These bending moments act at a distance $h_s/2$ from the bottom of the substrate. For $\Gamma = 1$ and $\kappa_1 = \kappa_2$, M does not cause shear and normal stresses at the interface between the film and substrate, and the stress and strain fields in the film and substrate are given by beam theory. For $\Gamma \neq 1$, the bending moments induce stresses at the interface, which we calculate as follows.

Note that the two moments in the x direction do not cause stresses on the interface if the inclusion and the matrix have the same curvature in the y-z plane (the z axis is perpendicular to the x and y axes shown in Fig. 1). Consequently, it is only necessary to consider the deformation caused by the two moments shown in Fig. 8. If we use the displacement field of a homogeneous problem ($\Gamma = 1, \kappa_1 = \kappa_2$) as a solution to the inhomogeneous problem there is a traction jump on the inclusion boundary. The solution may be

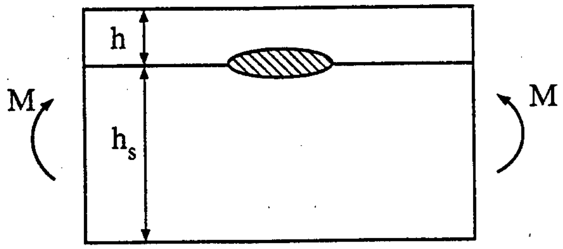

Fig. 8. Bending moments acting on the film substrate system.

corrected by superposing an equal and opposite traction jump on the inclusion boundary. The traction jump, expressed as a resultant force on the inclusion boundary, is

$$\begin{aligned} g(\tau) &= \mathrm{i}c_1\tau^2+\mathrm{i}c_1\frac{1}{\tau^2}-2\mathrm{i}c_1+c_2\tau-c_2\frac{1}{\tau}, \\ c_1 &= \frac{1}{8}R^2(1-m)^2(1-\Gamma)\frac{M}{I}, \\ c_2 &= -\frac{1}{2}R(1-m)(1-\Gamma)\frac{Mh_s}{2I}, \end{aligned} \tag{27}$$

where $I=(h_s+h)^3/12$. For simplicity, we have taken $\kappa_1 = \kappa_2$ to derive (27). When $h_s \to \infty$, $g(\tau) = 0$, which states the fact that a substrate with infinite thickness does not induce bending curvature. The function $g(\tau)$ plays the same role as that in Section 2, so that the solution can be obtained by the same way as that in the Appendix. For a circular inclusion, the solution is

$$\begin{aligned} \phi_1(\zeta) &= \frac{1}{\Gamma\kappa+1}\left(\mathrm{i}c_1\frac{1}{\zeta^2}-c_2\frac{1}{\zeta}\right), \\ \psi_1(\zeta) &= -\frac{\kappa}{\Gamma+\kappa}\mathrm{i}c_1\frac{1}{\zeta^2}-\frac{1-\kappa}{2\Gamma+\kappa-1}c_2\frac{1}{\zeta}-\frac{1}{\zeta}\phi_1'(\zeta), \end{aligned} \tag{28}$$

where $\kappa = \kappa_1 = \kappa_2$. Then, the normal and shear stresses on the interface between the film and substrate near the inclusion are

$$\begin{aligned} \sigma_{xy}(\rho,0) &= \frac{3Rh}{4h_s^2}\sigma_0(1-\Gamma)\left(\frac{1}{\Gamma\kappa+1}\frac{6\rho^2-8}{\rho^5}+\frac{\kappa}{\Gamma+\kappa}\frac{2}{\rho^3}\right), \\ \sigma_{yy}(\rho,0) &= -\frac{3h}{2h_s}\sigma_0(1-\Gamma)\left(\frac{1}{\Gamma\kappa+1}\frac{3}{\rho^4}+\frac{1-\kappa}{2\Gamma+\kappa-1}\frac{1}{\rho^2}\right). \end{aligned} \tag{29}$$

The condition, h, $h_s \gg R$, must be satisfied for the solution to be valid as explained at the beginning of the section. The normal stress is in compression for a soft inclusion ($\Gamma < 1$), and the shear stress is proportional to a coefficient in (29), i.e.,

$$\sigma_{xy}(\rho,0) \sim \frac{3Rh}{4h_s^2}\sigma_0. \tag{30}$$

Suppose that

$$h_s > 10h > 1000R, \tag{31}$$

we have from (30) that

$$\sigma_{xy}(\rho,0) \sim \frac{9}{80000}\sigma_0. \tag{32}$$

The shear stress may be neglected.

5. THREE-DIMENSIONAL PROBLEM

In general, the problem of an inclusion on the interface between the film and substrate is likely to be a three-dimensional problem. The analytical solution to a three-dimensional

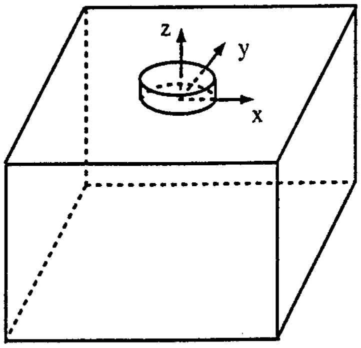

Fig. 9. Three-dimensional problem.

inclusion problem is difficult and available solutions can be found in Mura (1987). In this section, by assuming that the elastic properties of the inclusion, film and substrate are the same, we find an exact solution to the three-dimensional inclusion problem for the case that the loading is lattice parameter mismatch between the film and substrate. As before, we assume that the film thickness is much larger than the size of the inclusion.

The three-dimensional problem can be decomposed into two problems. One represents the lattice parameter mismatch in the x and y directions, and the other represents the mismatch in the z direction (the x, y, z axes are shown in Fig. 9, and the film thickness direction is designated as z). As in Section 2, we shall assume that there is no lattice parameter mismatch in the z direction and the Poisson's ratio of the film is very small. In other words, the mismatch in the z direction can be neglected. Following the argument given in Section 2, the solution to the three-dimensional problem can be obtained by integrating a point force solution over the inclusion boundary. To do this, we write the solution of a point force in the following form

$$\sigma_{ij}^{k}(x,y,z)=\frac{P^{k}}{8\pi(1-\nu)}\hat{\sigma}_{ij}^{k}(x-x_{0},y-y_{0},z-z_{0}), \tag{33}$$

where indices i, j and k vary from 1 to 3, designating the x, y and z in turn; P^k is a vector force in the k direction. The function $\hat{\sigma}_{xy}^{k}$ has the dimension 1/[length]^2. Equation (33) represents the stress field due to a point force in the direction k acting at (x_0, y_0, z_0). The stresses induced by an inclusion or a step irregularity can be written as

$$\sigma_{ij}(x,y,z)=\frac{\sigma_{0}}{8\pi(1-\nu)}\left[\int\!\!\int_{(x_{0},y_{0},z_{0})\in S}n_{x}\hat{\sigma}_{ij}^{1}(x-x_{0},y-y_{0},z-z_{0})\,\mathrm{d}S\right.$$
$$\left.+\int_{(x_{0},y_{0},z_{0})\in S}n_{y}\hat{\sigma}_{ij}^{2}(x-x_{0},y-y_{0},z-z_{0})\,\mathrm{d}S\right], \tag{34}$$

where S is the inclusion boundary that is surrounded by the film, or the vertical part of the step irregularity, and $\mathbf{n}=(n_x, n_y, n_z)$ is the unit outward normal to the inclusion boundary at (x_0, y_0, z_0). For the two normal stresses parallel to the interface between the film and substrate, σ_{xx} and σ_{yy}, the residual stress σ_0 has to be added to obtain the total stresses. The two surface integrals in (34) can not be evaluated analytically for an arbitrary inclusion shape. They cannot even be evaluated exactly for some simple shapes like a sphere. However, the surface integrals can be reduced to line integrals to simplify them in many cases. Two examples will be given below.

The first example is a corner step irregularity, as shown in Fig. 10. The corner step irregularity occupies the region, $x \leqslant 0$, $y \leqslant 0$ and $0 \leqslant z \leqslant a$. Note that, if we extend the above step irregularity region in the y direction and let it occupy $x \leqslant 0$, $-\infty \leqslant y \leqslant \infty$ and $0 \leqslant z \leqslant a$, it becomes the two-dimensional problem which was solved in Section 2. The purpose of this example is to examine the effect of a corner on the stress distribution. In

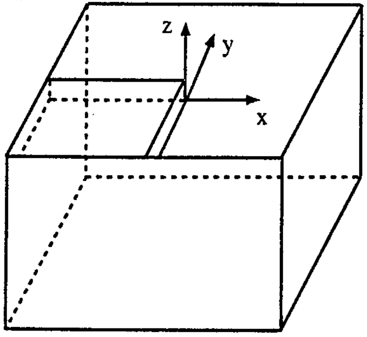

Fig. 10. A corner step irregularity.

this case, the integrations in (34) can be evaluated analytically. The two shear stresses on the plane $z = 0$ are given by

$$\begin{aligned}
\sigma_{xz}(x,y,0) &= \frac{\sigma_0}{8\pi(1-\nu)}\left[-\frac{a^2 y}{(x^2+a^2)\sqrt{x^2+y^2+a^2}}+\frac{a^2}{x^2+a^2}\right.\\
&\quad\left.+(1-2\nu)\log\frac{y+\sqrt{x^2+y^2+a^2}}{y+\sqrt{x^2+y^2}}\right],\\
\sigma_{yz}(x,y,0) &= \frac{\sigma_0}{8\pi(1-\nu)}\left[-\frac{a^2 x}{(y^2+a^2)\sqrt{x^2+y^2+a^2}}+\frac{a^2}{y^2+a^2}\right.\\
&\quad\left.+(1-2\nu)\log\frac{x+\sqrt{x^2+y^2+a^2}}{x+\sqrt{x^2+y^2}}\right].
\end{aligned}\tag{35}$$

The shear stress σ_{xz} in (35) has a logarithmic singularity on the straight line, $x = 0$ and $y \leqslant 0$, as in the two-dimensional case. The corner introduces a stress σ_{yz}, which is zero in the two-dimensional case. Far away from the corner, its influence vanishes so that σ_{yz} approaches zero as $y \to \pm\infty$. A plot of σ_{yz} vs y when $x = 0.01a$ is given in Fig. 11. We observe that the σ_{yz} is negligible for $|x| > 5a$. On the other hand, σ_{xz} approaches the two-dimensional solution given in Section 2 as $y \to -\infty$, and vanishes when $y \to +\infty$. The variation of σ_{xz} along the y axis when $x = 0.01a$ is also shown in Fig. 11. The two shear stresses at $y = 0$, $z = 0$ are given by

$$\sigma_{xz}(x,0,0) = \frac{\sigma_0}{8\pi(1-\nu)}\left(\frac{a^2}{x^2+a^2}+(1-2\nu)\log\sqrt{\frac{x^2+a^2}{x^2}}\right),$$

$$\sigma_{yz}(x,0,0) = \frac{\sigma_0}{8\pi(1-\nu)}\left(\frac{a^2}{\sqrt{x^2+a^2}(x+\sqrt{x^2+a^2})}\right)$$

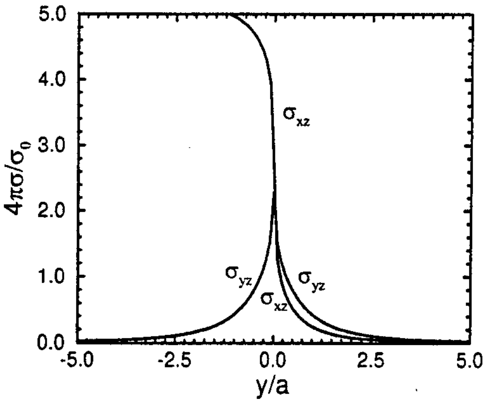

Fig. 11. Shear stresses near a corner step irregularity.

$$+(1-2\nu)\log\frac{x+\sqrt{x^2+a^2}}{2x}\Bigg) \tag{36}$$

for $x > 0$. Comparing $\sigma_{xz}(x,0,0)$ with $\sigma_{xz}(x,-\infty,0)$, we see that there is a simple relationship between them,

$$\sigma_{xz}(x,-\infty,0) = 2\sigma_{xz}(x,0,0). \tag{37}$$

This tells us that by traveling from $y = -\infty$ to $y = 0$, σ_{xz} reduces to half of its value at $y = -\infty$, and σ_{yz} rises from zero to the one given in (36). Also, we have another relationship,

$$\sigma_{xz}^2(x,0,0)+\sigma_{yz}^2(x,0,0) < \sigma_{xz}^2(x,-\infty,0) \tag{38}$$

for $x > 0$. This says that on the interface between the film and substrate the total shear stress at $(x,0,0)$ is less than the total shear stress at $(x,-\infty,0)$, because the corner relieves stress concentration.

The second example is a circular plate above the interface of the film and substrate, as shown in Fig. 9. Both the thickness and radius of the circular plate are a. The axisymmetry of the problem renders σ_{rz} (r,θ and z are used instead of x, y and z) is the only nontrial shear stress, which on the interface is given by

$$\begin{aligned}\sigma_{rz}(r,0,0) = & -\frac{\sigma_0 a}{4\pi(1-\nu)}\int_0^\pi (r-a\cos\theta)(r\cos\theta-a)\\ & \times\left[\frac{1}{(r^2-2ar\cos\theta+2a^2)^{3/2}}-\frac{1}{(r^2-2ar\cos\theta+a^2)^{3/2}}\right]\mathrm{d}\theta\\ & -\frac{\sigma_0 a}{4\pi(1-\nu)}(1-2\nu)\int_0^\pi \cos\theta\left[\frac{1}{(r^2-2ar\cos\theta+2a^2)^{1/2}}\right.\\ & \left.-\frac{1}{(r^2-2ar\cos\theta+a^2)^{1/2}}\right]\mathrm{d}\theta,\end{aligned} \tag{39}$$

after evaluating the integrals in (34) along the z direction. Further derivation shows that the line integrals in above expression can be written in terms of elliptical integrals. The σ_{rz} has a logarithmic singularity at $r = a$, and a plot of σ_{rz} vs r is shown in Fig. 12.

We can also give the expressions for other stress components in the above two examples by evaluating the integrals in (34). The inclusion shape has a strong effect on the stresses near the inclusion. For the circular plate, $\sigma_{rz}(1.1a,0,0) = 0.186\sigma_0$ and σ_{zz}

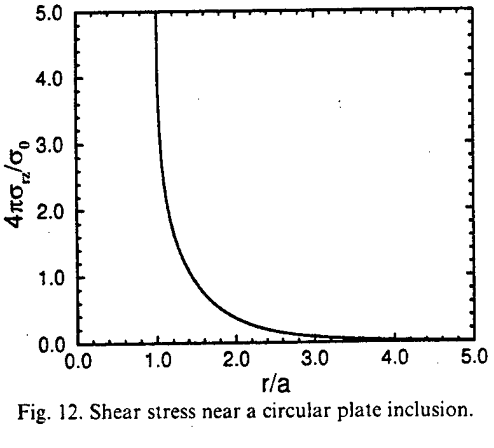

Fig. 12. Shear stress near a circular plate inclusion.

$(a, 0, 0) = -0.02\sigma_0$, whereas for the two-dimensional circular inclusion in Section 2, the two stresses on the interface between the film and substrate are $0.23\sigma_0$ and $-0.1\sigma_0$, respectively.

6. DISLOCATIONS IN THIN FILMS

Over the past few decades, the so-called threading dislocations which form in epitaxial layers used for semiconductor materials have received attention. Threading dislocations occur when the thickness of an epitaxial layer reaches a critical value. The critical thickness has been treated by a number of authors, including Matthews and Blakeslee (1974), People and Bean (1985) and Freund (1990). But the mechanism responsible for forming such dislocations has not yet been fully understood. Eaglesham *et al.* (1989) have discussed the diamond defect as a source for dislocation nucleation. Dodson (1988) has argued that the stress concentration around clusters of impurity atoms is a good source to generate dislocations. The experiments by Perovic *et al.* (1989) have shown that, for films grown by molecular beam epitaxy, there are precipitates on the interface between the film and substrate, and V-shaped threading dislocations are emitted from the heterogeneous particles if their size exceeds critical value, while particles below the critical size are coherent with surrounding matrix. Among the two types of heterogeneous precipitates on the interface, it was found that β-SiC precipitates tend to generate dislocations, whereas SiO_x precipitates are dislocation-free (Hull, 1986) because they are in an amorphous state which eliminates misfit strains. In this section, we consider these observations in the light of our solutions to the state of stresses near inclusions in strained layer systems.

We examine the shear stress, which provides the glide force for dislocation motion, on possible slip planes around the inclusion. Two representatives of the slip planes shown in Fig. 13 are chosen for the two-dimensional problems (circular inclusion and step irregularity) whose solutions have been obtained in Section 2. The orientation of these slip planes is chosen here to form the angle, $\theta = \sin^{-1}(1/\sqrt{3})$, with the interface between the film and substrate. We neglect the difference in elastic properties among the inclusion, film and substrate. Figure 14 shows the shear stress for the circular inclusion, where r/a is the distance from the inclusion; it has the same trend for the step irregularity. The shear stress at the inclusion boundary on slip plane #1 for the step irregularity has a logarithmic singularity, and for the circular inclusion it is nearly twice as large as that far away from the inclusion, the homogeneous solution. The high shear stress state provides a good condition to generate dislocations. The shear stress on slip plane #2 is somewhat different from slip plane #1. Although there is a logarithmic singularity at the inclusion boundary, the shear stress changes sign at a distance very close to the inclusion, and increases to the homogeneous solution as the distance increases. The shear stress near the inclusion on any

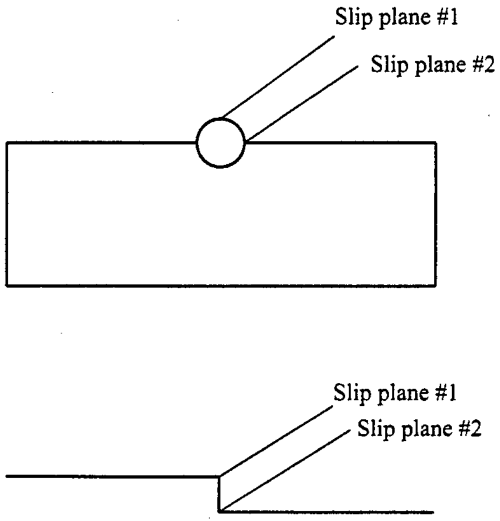

Fig. 13. Two possible slip planes which intersect the circular inclusion and the step irregularity.

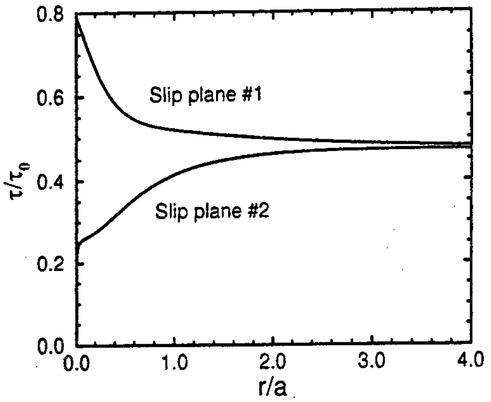

Fig. 14. Shear stress near the circular inclusion on the two slip planes shown in Fig. 13.

slip plane, which is between slip planes #1 and #2 and is parallel to these two slip planes, is less than that on slip plane #1.

If the inclusion is admitted as a source for dislocation nucleation in a thin film, the driving force for the emitted dislocation can be derived as follows. The energy dissipation associated with the dislocation motion is expressed as

$$W(S) = -\frac{1}{2}\int_S \sigma^D_{ij} n_j b_i \, \mathrm{d}s - \int_S \sigma^A_{ij} n_j b_i \, \mathrm{d}s, \tag{40}$$

where S is the glide plane; n_j is the outward normal of the left portion of the film divided by the slip plan; the Burgers vector b_i is the displacement of the left side of the glide plane minus that of the right side of the glide plan. In the expression, the stress field σ^D_{ij} is due to the dislocation, and σ^A_{ij} is due to the applied load, namely the lattice parameter mismatch. Define the driving force G from the time rate of the energy dissipation as

$$\dot{W}(S) = Gv, \tag{41}$$

where v the speed of the emitted dislocation. The driving force is derived in the same way as that in Freund (1990) for threading dislocation, and is given by

$$G = -\tfrac{1}{2}\sigma^D_{ij}(A) n_j b_i - \sigma^A_{ij}(B) n_j b_i, \tag{42}$$

where $\sigma^D_{ij}(A)$ and $\sigma^A_{ij}(B)$ denote the corresponding stresses at the inclusion boundary and the position of the emitted dislocation, respectively. Note that since the difference in elastic properties between the inclusion and the matrix is neglected, there is no image force due to the mismatch of elastic properties acting on the dislocation. The first term in (42) can be calculated from the solution of a dislocation in a infinite body, and the second term can be calculated from the solution obtained in Section 2. We finally obtain

$$\frac{G}{\mu b} = -\frac{1}{4\pi(1-\nu)}\frac{b}{a}\left(\frac{r}{a}\right)^{-1} + \frac{2(1+\nu)}{1-\nu}\varepsilon_0 T\left(\frac{r}{a}\right), \tag{43}$$

where r is the distance between the dislocation and the inclusion boundary, a is the size of the inclusion, b is the magnitude of the Burgers vector, and $T(r/a)$ is a nondimensional function obtained from the stresses $\sigma^A_{ij}(B)$. Given the inclusion size, the magnitude of the Burgers vector and the misfit strain, the distance from the inclusion at which $G = 0$ (equilibrium point), namely r^*, is determined from (43). For $r > r^*$, $G > 0$; for $r < r^*$, $G < 0$. If the dislocation is formed at the distance less than r^* from the inclusion, it will be driven back to the inclusion boundary; otherwise, it will be emitted. We take the circular inclusion as an example, and consider slip plane #1. For $b = 0.4$ nm and $\varepsilon_0 = 0.04$,

$r^* = 0.458$ nm if $a = 100$ nm; $r^* = 0.473$ nm if $a = 10$ nm; $r^* = 0.673$ nm if $a = 1$ nm. When ε_0 is increased to 0.06, r^* is 0.305 nm, 0.311 nm and 0.415 nm for the above three cases, respectively. The larger the misfit strain and the inclusion size, the smaller the critical distance r^*. When r^* is less than the core cut-off radius, we have the case that the dislocation formed at the inclusion boundary is emitted spontaneously (see Rice and Thomson (1974) for dislocation emission from a crack tip). The numerical results here show that dislocation emission is favored for large misfit strain. For inclusions in shapes other than the two we have treated here, the driving force may be obtained in the same manner. Zhang and Yang (1994) have studied the process of dislocation emission from a spherical cavity on the interface between the film and substrate.

7. CONCLUDING REMARKS

Solutions are presented for several boundary value problems involving various shaped inclusions located on the interface between a thin film and a substrate. The film and the substrate have different lattice parameters. The solutions exhibit stress concentrations around the inclusions. There is a logarithmic stress singularity at the intersection of the film, substrate and inclusion. Moreover, the shear stress around the inclusion can be nearly twice as large as the remote field given by the homogeneous solution. High stresses around inclusions and on the interface between film and substrate could cause dislocation nucleation and adhesion failure. A theoretical prediction of the misfit strain to cause adhesion failure is obtained. The driving force for dislocation emission from the inclusion is calculated, and it is shown that dislocation emission from inclusions is favored for sufficiently large misfit strain. The results suggest that small inclusions (compared to film thickness) on the interface between a film and a substrate can be the sources for failure initiation in the layered system. These failures can be precursors to failures on a larger scale: adhesion failure can lead to film buckling; and dislocation emission eventually causes threading dislocations as shown by Zhang and Yang (1994) for a spherical cavity.

Acknowledgements—PG and CFS acknowledge the support from the Office of Naval Research through Grant N00014-90-J-1380. PG and RJA acknowledge the support from the Office of Naval Research through Grant N00014-93-1-1164.

REFERENCES

Alexopoulos, P. S. and O'Sullivan, T. C. (1990) Mechanical properties of thin films. *A. Rev. Mat. Sci.* **20**, 391–420.

Dodson, B. W. (1988) Nature of misfit dislocation sources in strained-layer semiconductor structures. *Appl. Phys. Lett.* **53**, 394–396.

Eaglesham, D. J., Kvam, E. P., Maher, D. M., Humphreys, C. J. and Bean, J. C. (1989) Dislocation nucleation near the critical thickness in GeSi/Si strained layers. *Phil. Mag.* **A59**, 1059–1073.

Evans, A. G. and Hutchinson, J. W. (1984) On the mechanics of delamination and spalling in compressed films. *Int. J. Solids Structures* **20**, 455–466.

Evans, A. G., Drory, M. D. and Hu, M. S. (1988) The cracking and decohesion of thin films. *J. Mater. Res.* **3**, 1043–1049.

Freund, L. B. (1990) The driving force for glide of a threading dislocation in a strained epitaxial layer on a substrate. *J. Mech. Phys. Solids* **38**, 657–679.

Freund, L. B. (1993) The mechanics of dislocations in strained-layer semiconductor materials. *Adv. Appl. Mech.* **30**, 1–66.

Hu, S. M. (1991) Stress-related problems in silicon technology. *J. Appl. Phys.* **70**, R53–R80.

Hull, R., Bean, J. C., Gibson, J. M., Joy, D. C. and Twigg, M. E. (1986) Trapping of oxygen at homoepitaxial Si–Si interfaces. *Appl. Phys. Lett.* **49**, 1287–1289.

Hutchinson, J. W. and Suo, Z. (1991) Mixed mode cracking in layered materials. *Adv. Appl. Mech.* **29**, 63–191.

List, R. D. and Silberstein, J. P. O. (1966) Two-dimensional elastic inclusion problems. *Proc. Cambridge Phil. Soc.* Vol. 62, pp. 303–311.

Matthews, J. W. and Blakeslee, A. E. (1974) Defects in epitaxial multilayers. *J. Crystal Growth* **27**, 118–125.

Mura, T. (1987) *Micromechanics of Defects in Solids*, 2nd edn. Martinus Nijhoff Publishers.

Muskhelishivili, N. I. (1953) *Some Basic Problems of the Mathematical Theory of Elasticity*, 3rd edn, Noordhoff.

People, R. and Bean, J. C. (1985) Calculation of critical layer thickness versus lattice mismatch for Ge_xSi_{1-x}/Si strained-layer heterostructures. *Appl. Phys. Lett.* **47**, 322–324.

Perovic, D. D., Weatherly, G. C., Baribeau, J.-M. and Houghton, D. C. (1989) Heterogeneous nucleation sources in molecular beam epitaxy-grown Ge_xSi_{1-x}/Si strained layer superlattices. *Thin Solid Films*. **183**, 141–156.

Rice, J. R. and Thomson, R. (1974) Ductile versus brittle behaviour of crystals. *Phil. Mag.* **29**, 73–97.

Zhang, H. and Yang, W. (1994) Three-dimensional dislocation loops generated from a weak inclusion in a strained material heterostructure. *J. Mech. Phys. Solids* **42**, 913–930.

APPENDIX

After the conformal mapping, the two potentials for the matrix, $\phi_1(\zeta)$ and $\psi_1(\zeta)$, are analytical outside the unit circle $|\zeta| = 1$, and admit the forms,

$$\phi_1(\zeta) = \frac{a_1}{\zeta} + \frac{a_2}{\zeta^2} + \cdots,$$

$$\psi_1(\zeta) = \frac{b_1}{\zeta} + \frac{b_2}{\zeta^2} + \cdots. \tag{A.1}$$

The two potentials for the inclusion, $\phi_2(\zeta)$ and $\psi_2(\zeta)$, are not analytic inside unit circle, and are expressed by Laurent series,

$$\phi_2(\zeta) = \phi_{21}(\zeta) + \phi_{22}(\zeta), \quad \psi_2(\zeta) = \psi_{21}(\zeta) + \psi_{22}(\zeta), \tag{A.2}$$

where

$$\phi_{21}(\zeta) = c_0 + c_1\zeta + c_2\zeta^2 + \cdots, \quad \phi_{22}(\zeta) = c_{-1}\frac{1}{\zeta} + c_{-2}\frac{1}{\zeta^2} + \cdots,$$

$$\psi_{21}(\zeta) = d_0 + d_1\zeta + d_2\zeta^2 + \cdots, \quad \psi_{22}(\zeta) = d_{-1}\frac{1}{\zeta} + d_{-2}\frac{1}{\zeta^2} + \cdots. \tag{A.3}$$

The following relations hold because of the mapping,

$$\phi_{21}\left(\frac{m}{\zeta}\right) - \phi_{21}(0) = \phi_{22}(\zeta),$$

$$\psi_{21}\left(\frac{m}{\zeta}\right) - \psi_{21}(0) = \psi_{22}(\zeta). \tag{A.4}$$

Taking the integrations, $(1/2\pi i)\int_\gamma 1/(\tau-\zeta)\,d\tau$, where $|\zeta| > 1$ and γ denotes the unit circle $|\zeta| = 1$, on (6), we obtain

$$-\phi_1(\zeta) + \phi_{22}(\zeta) + \frac{\zeta^2+m}{\zeta(1-m\zeta^2)}\bar{\phi}'_{21}\left(\frac{1}{\zeta}\right) + \frac{1+m^2}{2m}\frac{1}{\zeta - \dfrac{1}{\sqrt{m}}}\bar{\phi}'_{21}(\sqrt{m})$$
$$+ \frac{1+m^2}{2m}\frac{1}{\zeta + \dfrac{1}{\sqrt{m}}}\bar{\phi}'_{21}(-\sqrt{m}) + \bar{\psi}_{21}\left(\frac{1}{\zeta}\right) - \bar{\psi}_{21}(0) = g_1(\zeta),$$

$$-\frac{\kappa_1}{2\mu_1}\phi_1(\zeta) + \frac{\kappa_2}{2\mu_2}\phi_{22}(\zeta) - \frac{1}{2\mu_2}\frac{\zeta^2+m}{\zeta(1-m\zeta^2)}\bar{\phi}'_{21}\left(\frac{1}{\zeta}\right)$$
$$-\frac{1}{2\mu_2}\frac{1+m^2}{2m}\frac{1}{\zeta - \dfrac{1}{\sqrt{m}}}\bar{\phi}'_{21}(\sqrt{m}) - \frac{1}{2\mu_2}\frac{1+m^2}{2m}\frac{1}{\zeta + \dfrac{1}{\sqrt{m}}}\bar{\phi}'_{21}(-\sqrt{m})$$
$$-\frac{1}{2\mu_2}\bar{\psi}_{21}\left(\frac{1}{\zeta}\right) + \frac{1}{2\mu_2}\bar{\psi}_{21}(0) = 0, \tag{A.5}$$

where

$$g_1(\zeta) = \frac{1}{2\pi i}\int_\gamma \frac{g(\tau)}{\tau - \zeta}\,d\tau. \tag{A.6}$$

The same integrations on the conjugates of the two equations in (6) give

$$-\frac{\zeta(1+m\zeta^2)}{\zeta^2-m}\phi'_1(\zeta) - \psi_1(\zeta) + \bar{\phi}_{21}\left(\frac{1}{\zeta}\right) - \bar{\phi}_{21}(0) + \frac{1+m^2}{2}\left[\frac{1}{\zeta-\sqrt{m}}\phi'_{21}(\sqrt{m}) + \frac{1}{\zeta+\sqrt{m}}\phi'_{21}(\sqrt{-m})\right]$$
$$+ \frac{\zeta(1+m\zeta^2)}{\zeta^2-m}\phi'_{22}(\zeta) + \psi_{22}(\zeta) = g_2(\zeta),$$

$$\frac{1}{2\mu_1}\frac{\zeta(1+m\zeta^2)}{\zeta^2-m}\phi_1'(\zeta)+\frac{1}{2\mu_1}\psi_1(\zeta)+\frac{\kappa_2}{2\mu_2}\bar{\phi}_{21}\left(\frac{1}{\zeta}\right)-\frac{\kappa_2}{2\mu_2}\bar{\phi}_{21}(0)$$

$$-\frac{1}{2\mu_2}\frac{1+m^2}{2}\left[\frac{1}{\zeta-\sqrt{m}}\phi_{21}'(\sqrt{m})+\frac{1}{\zeta+\sqrt{m}}\phi_{21}'(\sqrt{-m})\right]-\frac{1}{2\mu_2}\frac{\zeta(1+m\zeta^2)}{\zeta^2-m}\phi_{22}'(\zeta)-\frac{1}{2\mu_2}\psi_{22}(\zeta)=0, \quad (A.7)$$

where

$$g_2(\zeta)=\frac{1}{2\pi\mathrm{i}}\int_{\gamma}\frac{\overline{g(\tau)}}{\tau-\zeta}\mathrm{d}\tau. \quad (A.8)$$

The following equation is obtained by (A.5.1) – (A.5.2) × $2\mu_1/\kappa_1$,

$$\frac{\mu_2\kappa_1-\mu_1\kappa_2}{\mu_2\kappa_1+\mu_1}\bar{\phi}_{22}(\zeta)+\frac{1+m^2}{2m}\left[\frac{1}{\zeta-\frac{1}{\sqrt{m}}}\phi_{21}'(\sqrt{m})+\frac{1}{\zeta+\frac{1}{\sqrt{m}}}\phi_{21}'(\sqrt{-m})\right]$$

$$-\frac{m\zeta(\zeta^2+m)}{1-m\zeta^2}\phi_{22}'(m\zeta)+\psi_{22}(m\zeta)=\frac{\mu_2\kappa_1}{\mu_2\kappa_1+\mu_1}\overline{g_1}(\zeta). \quad (A.9)$$

Similarly, (A.7.1) + (A.7.2) × $2\mu_1$ gives

$$\frac{\mu_1\kappa_2+\mu_2}{\mu_2-\mu_1}\bar{\phi}_{22}(m^2\zeta)+\frac{1+m^2}{2m}\left[\frac{1}{\zeta-\frac{1}{\sqrt{m}}}\phi_{21}'(\sqrt{m})+\frac{1}{\zeta+\frac{1}{\sqrt{m}}}\phi_{21}'(\sqrt{-m})\right]$$

$$+\frac{\zeta(1+m^3\zeta^2)}{m\zeta^2-1}\phi_{22}'(m\zeta)+\psi_{22}(m\zeta)=\frac{\mu_2}{\mu_2-\mu_1}g_2(m\zeta). \quad (A.10)$$

In obtaining (A.9) and (A.10), we have made use of (A.4). Also, we have replaced the variable ζ by $m\zeta$ in (A.10). By (A.9) – (A.10), an ordinary differential equation for $\phi_{22}(\zeta)$ is obtained,

$$\frac{\mu_1\kappa_2+\mu_2}{\mu_2-\mu_1}\bar{\phi}_{22}(\zeta)+\frac{\mu_1\kappa_2-\mu_2\kappa_1}{\mu_2\kappa_1+\mu_1}\bar{\phi}_{22}\left(\frac{\zeta}{m^2}\right)-(1-m^2)\frac{\zeta}{m^2}\phi_{22}'\left(\frac{\zeta}{m}\right)=q(\zeta), \quad (A.11)$$

where

$$q(\zeta)=-\frac{\mu_2\kappa_1}{\mu_2\kappa_1+\mu_1}\overline{g_1}\left(\frac{\zeta}{m^2}\right)+\frac{\mu_2}{\mu_2-\mu_1}g_2\left(\frac{\zeta}{m}\right). \quad (A.12)$$

Using (7), we evaluate the integrals in (A.6) and (A.8) to obtain

$$q(\zeta)=\frac{-\kappa_1\mu_2}{\kappa_1\mu_2+\mu_1}\frac{C}{2\pi\mathrm{i}}\left(-2-\frac{\pi\mathrm{i}m^2}{\zeta}+\frac{\zeta^2-m^4}{m^2\zeta}\log\frac{\zeta+m^2}{\zeta-m^2}\right)$$

$$+\frac{\mu_2}{\mu_2-\mu_1}\frac{C}{2\pi\mathrm{i}}\left(-2+\frac{\pi\mathrm{i}m}{\zeta}+\frac{\zeta^2-m^2}{m\zeta}\log\frac{\zeta+m}{\zeta-m}\right). \quad (A.13)$$

Generally, the solution for $\phi_{22}(\zeta)$ in (A.11) is expressed in terms of series. We write

$$q(\zeta)=\sum_{n=1}^{\infty}f_n\frac{1}{\zeta^n},$$

$$\phi_{22}(\zeta)=\sum_{n=1}^{\infty}a_n\frac{1}{\zeta^n}, \quad (A.14)$$

where f_n ($n=1,2,\ldots$) are the known coefficients from the series expansion of (A.13). We obtain $\phi_{22}(\zeta)$ by substituting (A.14) into (A.11) and comparing the coefficients of both sides.

By (A.5.1) + (A.5.2) × $2\mu_2$, the potential $\phi_1(\zeta)$ is obtained as

$$\phi_1(\zeta)=-\frac{\mu_1}{\mu_2\kappa_1+\mu_1}g_1(\zeta)+\frac{\mu_1(1+\kappa_2)}{\mu_2\kappa_1+\mu_1}\phi_{22}(\zeta). \quad (A.15)$$

Similarly, (A.7.1) + (A.7.2) × $2\mu_2$ gives

$$\psi_1(\zeta) = -\frac{\mu_1}{\mu_1-\mu_2}g_2(\zeta)-\zeta\frac{1+m\zeta^2}{\zeta^2-m}\phi_1'(\zeta)+\frac{\mu_1(1+\kappa_2)}{\mu_1-\mu_2}\bar{\phi}_{22}(m\zeta). \tag{A.16}$$

Evaluating the integrals in (A.15) and (A.16), we have the final result,

$$\phi_1(\zeta) = \frac{1}{\Gamma\kappa_1+1}\frac{C}{2\pi i}\left[-2+\frac{i\pi}{\zeta}+\frac{\zeta^2-1}{\zeta}\log\frac{\zeta+1}{\zeta-1}\right]+\frac{1+\kappa_2}{\Gamma\kappa_1+1}\frac{C}{2}\frac{(P_3m+P_4)m}{P_1+P_2m^2+1-m^2}\frac{1}{\zeta}-\frac{1+\kappa_2}{\Gamma\kappa_1+1}\frac{2C}{\pi i}\sum_{n=1}^{\infty}a_{2n}m^{2n}\frac{1}{\zeta^{2n}},$$

$$\begin{aligned}\psi_1(\zeta) = {}& \frac{1}{\Gamma-1}\frac{C}{2\pi i}\left[-2+\frac{i\pi}{\zeta}+\frac{\zeta^2-1}{\zeta}\log\frac{\zeta+1}{\zeta-1}\right] \\ & -\frac{\zeta+m\zeta^3}{\zeta^2-m}\phi_1'(\zeta)+\frac{1+\kappa_2}{1-\Gamma}\frac{C}{2}\frac{(P_3m+P_4)}{P_1+P_2m^2+1-m^2}\frac{1}{\zeta}+\frac{1+\kappa_2}{1-\Gamma}\frac{2C}{\pi i}\sum_{n=1}^{\infty}a_{2n}\frac{1}{\zeta^{2n}},\end{aligned} \tag{A.17}$$

where $\Gamma = \mu_2/\mu_1$ and

$$\begin{aligned} a_{2n} &= \frac{2(1-m^2)nm^{2n-1}+(P_1+P_2m^{4n})}{(P_1+P_2m^{4n})^2-4n^2(1-m^2)^2m^{4n-2}}(P_3m^{2n}-P_4)\frac{1}{4n^2-1}, \\ P_1 &= \frac{\Gamma+\kappa_2}{\Gamma-1}, \quad P_2 = -\frac{\Gamma\kappa_1-\kappa_2}{\Gamma\kappa_1+1}, \\ P_3 &= \frac{\Gamma\kappa_1}{\Gamma\kappa_1+1}, \quad P_4 = \frac{\Gamma}{\Gamma-1}. \end{aligned} \tag{A.18}$$

The two potentials for the inclusion, $\phi_2(\zeta)$ and $\psi_2(\zeta)$, can also be obtained.

Pergamon

Int. J. Solids Structures Vol. 34, No. 1, pp. 1–17, 1997
Copyright © 1996 Elsevier Science Ltd
Printed in Great Britain. All rights reserved
0020–7683/97 $15.00 + .00

0020–7683(95)00289–8

CRACKS IN FUNCTIONALLY GRADED MATERIALS

PEI GU and R. J. ASARO
Department of Applied Mechanics and Engineering Sciences,
University of California at San Diego, La Jolla, CA 92093-0411, U.S.A.

(*Received* 25 *October* 1995; *in revised form* 13 *November* 1995)

Abstract—A semi-infinite crack in a strip of an isotropic, functionally graded material under edge loading and in-plane deformation conditions is analyzed. Mixed mode stress intensity factors are analytically solved for up to a numerically determined parameter. The effects of material gradients on the mode I and mode II stress intensity factors and the phase angle used to measure mode mixity are determined. The solution is extended to the case where the strip is made of an orthotropic, functionally graded material. These results are applied to solve a four-point bending specimen configuration that may be used to test the fracture behavior of functionally graded materials. The nature of the crack tip fields and possible fracture criterion for functionally graded materials are discussed. Copyright © 1996 Elsevier Science Ltd

1. INTRODUCTION

Functionally graded materials (FGMs) to be used as, *inter alia*, superheat-resistive materials have promised attractive applications in furnace liners, space structures, and fusion reactors. FGMs consist of two distinct material phases, such as ceramic and metal alloy phases, and are the mixture of them such that the composition of each changes continuously along one direction. The change in microstructure induces chemical, material, and microstructural gradients, and makes functionally graded materials different in behavior from homogeneous materials and traditional composite materials (Yamanouchi *et al.*, 1990; Holt *et al.*, 1993). These materials are tailorable in their properties *via* the design of the gradients in chemistry and microstructure that is possible within them.

Experiments have shown that cracks occur in functionally graded materials (see above references) although the absence of sharp interfaces does alleviate problems with interface fracture. For cracks in this type of material, stress intensity factors are affected by the material gradients. Moreover, the fracture modes of the cracks in FGMs are inherently mixed when they are not parallel to the direction of material property variation, *i.e.*, there are typically both normal and shear tractions ahead of the crack tips because of the non-symmetry in the material properties. To characterize the material, fracture toughness data is required. To obtain the fracture toughness data, stress intensity factors for specimens subjected to variable external loads are needed. Most previous works on FGM crack configurations have concentrated on finite crack problems, *e.g.*, Delale and Erdogan (1983, 1988) and Noda and Jin (1993) have analyzed a finite crack in a plate subjected to mechanical and thermal loads. A semi-infinite crack in an interlayer between two dissimilar materials was considered by Yang and Shih (1994), and they obtained an approximate solution from a known bimaterial solution. We consider herein a semi-infinite crack in a strip of an isotropic, functionally graded material under edge loading and in-plane deformation conditions. Stress intensity factors for the crack tip are obtained. The solution is analytical up to a parameter which is obtained numerically. The solution is extended to the case where the strip is made of an orthotropic, functionally graded material. The results are applied to analyze a four-point bending specimen configuration that may be used to test the fracture behavior of functionally graded materials. The mode III stress intensity factor in the cracked plate subjected to anti-plane deformation is obtained. The nature of the crack tip fields and possible fracture criterion for functionally graded materials are discussed.

The main emphasis here is to analyze fracture behavior in materials that possess continuously graded microstructures. On the other hand, the physical picture developed for the cracked microstructure actually provides a more realistic model for cracks along interfaces, in general, at least for those that have any but atomic-scale width.

2. FIELD EQUATIONS FOR ISOTROPIC MEDIA

In this study, we take the elastic properties to be of following exponential forms

$$\begin{aligned} E'(y) &= E_0\,\mathrm{e}^{\gamma y}, \\ \nu'(y) &= \nu_0(1+\varepsilon y)\,\mathrm{e}^{\gamma y}, \end{aligned} \tag{1}$$

where γ and ε are material constants representing the material gradients; E_0 and ν_0 are the values of these elastic properties at $y = 0$. For plane stress problems, $E'(y) = E(y)$ and $\nu'(y) = \nu(y)$, where $E(y)$ and $\nu(y)$ are Young's modulus and Poisson's ratio, respectively; for plane strain problems, $E'(y) = E(y)/[1-\nu(y)^2]$ and $\nu'(y) = \nu(y)/[1-\nu(y)]$. The parameters γ and ε have a dimension $[\text{length}]^{-1}$. These forms for the material properties have been previously used by Delale and Erdogan (1988) and Noda and Jin (1993); they provide, on the one hand, analytical flexibility and yet lead to somewhat simple forms for the field equations. The shear modulus, $\mu(y)$, relates to Young's modulus and Poisson's ratio by

$$\mu(y) = \frac{E'(y)}{2[1+\nu'(y)]}. \tag{2}$$

Using (1) and (2), the stress function $\Phi(x, y)$ defined in the same way as that for homogeneous materials, *i.e.*, stresses are obtained from the second derivatives of the stress function, satisfies the following equation

$$\frac{\partial^4\Phi}{\partial x^4} + 2\frac{\partial^4\Phi}{\partial x^2\,\partial y^2} + \frac{\partial^4\Phi}{\partial y^4} - 2\gamma\frac{\partial}{\partial y}\left(\frac{\partial^2\Phi}{\partial x^2} + \frac{\partial^2\Phi}{\partial y^2}\right) + \gamma^2\frac{\partial^2\Phi}{\partial y^2} = 0. \tag{3}$$

For a traction problem, the solution satisfies (3) and boundary conditions. The material constant γ enters the stress field of the traction problem, whereas the other material parameters E_0, ν_0 and ε do not. In (3), the fourth-order differential terms do not involve γ, and constitute the biharmonic equation, which is the equation for homogeneous materials.

By dimensional analysis, the stress field has the following generic form

$$\sigma_{ij}(x, y) = T\sigma^*_{ij}\left(\gamma h, \frac{\mathscr{L}}{h}, \frac{x}{h}, \frac{y}{h}\right), \tag{4}$$

where $i, j = 1, 2$; T is a representative stress magnitude; h is a characteristic length in the problem; $\mathscr{L}$ is the group of lengths which represents the geometry of the problem. This differs from the case of a homogeneous material in which material properties do not enter the stress field of a traction problem, and also differs from the case of a bimaterial in which Dundurs' parameters (Dundurs, 1969) measuring the material mismatch enter the stress field of a traction problem.

The parameters γh in the solution is dependent on the thickness of a functionally graded material, L, the Young's moduli at the upper and the lower boundaries of the material, E'_u and E'_l, and the characteristic length, h. From (1),

$$\gamma h = \frac{h}{L}\ln\frac{E'_u}{E'_l}. \tag{5}$$

It is seen that γh is proportional to h/L, and increases logarithmically with the ratio of the two Young's moduli. For example, if $h/L = 1$, $\gamma h = 0.35$ for $E'_u/E'_l = 0.5$, and $\gamma h = 0.97$ for $E'_u/E'_l = 7$. The choice of h is arbitrary. If h_1 and h_2 denote two choices for the characteristic length, the corresponding stresses obtained satisfy the relation

$$\sigma^{*1}_{ij}\left(\gamma h_1, \frac{\mathscr{L}}{h_1}, \frac{x}{h_1}, \frac{y}{h_1}\right) = \sigma^{*2}_{ij}\left(\gamma h_2, \frac{\mathscr{L}}{h_2}, \frac{x}{h_2}, \frac{y}{h_2}\right). \tag{6}$$

3. CRACK TIP FIELDS

A brief review of the crack tip fields in functionally graded materials is given in this section. Consider a crack in a strip of a functionally graded material, as illustrated in Fig. 1. Stresses near the crack tip have a square-root singularity, and singular terms of the stresses (Jin and Noda, 1994) are of the form

$$\sigma_{ij} = \frac{K_{\mathrm{I}}}{\sqrt{2\pi r}}\bar{\sigma}^{\mathrm{I}}_{ij}(\theta) + \frac{K_{\mathrm{II}}}{\sqrt{2\pi r}}\bar{\sigma}^{\mathrm{II}}_{ij}(\theta) + \frac{K_{\mathrm{III}}}{\sqrt{2\pi r}}\bar{\sigma}^{\mathrm{III}}_{ij}(\theta), \tag{7}$$

where $i, j = 1, 2$; r and θ are the polar coordinates shown in Fig. 1. The dimensionless angular functions $\bar{\sigma}^{\mathrm{I}}_{ij}(\theta)$, $\bar{\sigma}^{\mathrm{II}}_{ij}(\theta)$ and $\bar{\sigma}^{\mathrm{III}}_{ij}(\theta)$ are the same as those for homogeneous materials. This can be easily proved by expanding the stress function as $\Sigma_{i=0} r^{i+\rho}\Phi_j(\theta,\gamma)$, and substituting the series into (3). The resulting equation for $\Phi_0(\theta,\gamma)$ and the eigen-value problem used to determine ρ do not involve γ and are the same as those for homogeneous materials. In fact, for any form of material properties and any orientation of the crack, the highest order differential terms in the equation which the stress function satisfies are the three fourth-order differential terms which constitute the biharmonic equation, and the terms in the equation involving material gradients are the lower order differential terms. These lead to that the equations for $\Phi_0(\theta,\gamma)$ and ρ are the same as those for homogeneous materials. The stress intensity factors K_{I}, K_{II} and K_{III} are functions of the material gradients, external load, and geometry. Material gradients do not affect the order of the singularity and the angular functions, but do affect the stress intensity factors. As a result the near-tip stresses have the same form as that for a homogeneous material. For an interface crack, stresses have an oscillatory singularity, and both the stress intensity factors and angular functions involve Dundurs' parameters, *i.e.*,

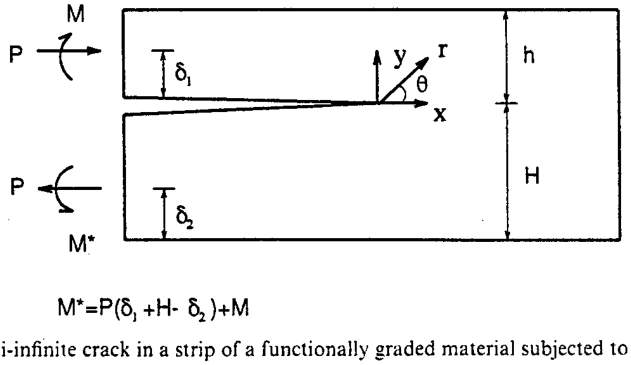

$M^* = P(\delta_1 + H - \delta_2) + M$

Fig. 1. A semi-infinite crack in a strip of a functionally graded material subjected to edge loading.

$$\sigma_{ij} = \frac{\mathrm{Re}(Kr^{i\varepsilon})}{\sqrt{2\pi r}}\bar{\sigma}^{\mathrm{I}}_{ij}(\theta, \varepsilon) + \frac{\mathrm{Im}(Kr^{i\varepsilon})}{\sqrt{2\pi r}}\bar{\sigma}^{\mathrm{II}}_{ij}(\theta, \varepsilon) + \frac{K_{\mathrm{III}}}{\sqrt{2\pi r}}\bar{\sigma}^{\mathrm{III}}_{ij}(\theta), \tag{8}$$

where $K = K_{\mathrm{I}} + iK_{\mathrm{II}}$ is complex stress intensity factor, and

$$\varepsilon = \frac{1}{2\pi}\ln\frac{1-\beta}{1+\beta}. \tag{9}$$

In (9), β is one of the two Dundurs' parameters. The Dundurs' parameters, α and β, are defined as

$$\begin{aligned} \alpha &= \frac{\mu_1(\kappa_2+1)-\mu_2(\kappa_1+1)}{\mu_1(\kappa_2+1)+\mu_2(\kappa_1+1)}, \\ \beta &= \frac{\mu_1(\kappa_2-1)-\mu_2(\kappa_1-1)}{\mu_1(\kappa_2+1)+\mu_2(\kappa_1+1)}, \end{aligned} \tag{10}$$

where μ_1 and μ_2 are the shear moduli of the two bulk materials; $\kappa_i = 3-4\nu_i$ for plane strain and $\kappa_i = (3-\nu_i)/1+\nu_i)$ for plane stress (i = 1, 2), with ν_1 and ν_2 being the Poisson's ratios of the two bulk materials. It is noted that, by considering material gradients near the tip of an interface crack, the oscillatory behavior is removed, and the angular functions become independent of material properties. In this sense, the solutions presented here represent a more physically acceptable description of interface crack tip fields, at least for interfaces that have a finite width.

The strains obtained from the stresses given in (7) are

$$\varepsilon_{ij} = S_{ijkl}(0)\sigma_{kl} + [S_{ijkl}(y) - S_{ijkl}(0)]\sigma_{kl}, \tag{11}$$

where $S_{ijkl}(y)$ is the compliance tensor, and $S_{ijkl}(0)$ is the tensor at the crack tip. The second term in the above equation is in the order of $r^{3/2}$. So the singular strain field is

$$\varepsilon_{ij} = S_{ijkl}(0)\sigma_{kl}. \tag{12}$$

From (12), one is able to show that the near-tip displacement field is the same as that for the homogeneous materials.

From (7), the traction at the distance r ahead of the crack tip is

$$\sigma_{yy} + i\sigma_{xy} = \frac{K}{\sqrt{2\pi r}} \tag{13}$$

for an in-plane problem. For a mode III problem, the traction is, likewise,

$$\sigma_{yz} = \frac{K_{\mathrm{III}}}{\sqrt{2\pi r}}. \tag{14}$$

Having the near tip stress and displacement fields, the energy release rate of the crack tip is obtained as

$$\mathscr{G} = \frac{K_{\mathrm{I}}^2}{E'(0)} + \frac{K_{\mathrm{II}}^2}{E'(0)} + \frac{K_{\mathrm{III}}^2}{2\mu(0)}, \tag{15}$$

where $E'(0)$ and $\mu(0)$ are the Young's modulus and the shear modulus at the crack tip, respectively. It can be seen that the above eqns. (7) and (12)–(15), are independent of the forms of the material properties and the orientation of the crack, and they all have the same forms as those for homogeneous materials. The path-independence of the J integral (Rice, 1968) holds if the crack is perpendicular to the direction along which material properties change; this is implied in Rice's original proof for homogeneous materials. Using the near tip fields obtained above, it can be shown that the J integral is equal to the energy release rate for the crack perpendicular to the direction along which material properties change.

The complex stress intensity $K = K_{\rm I} + iK_{\rm II}$ for FGMs has the following generic form

$$K = |K|\,e^{i\psi}, \tag{16}$$

where

$$\psi = \tan^{-1}\frac{K_{\rm II}}{K_{\rm I}} \tag{17}$$

is the phase angle of the complex stress intensity factor. The phase angle measures mode mixity, *i.e.*, the proportion of the shear traction to the normal traction ahead of the crack tip, since

$$\psi = \tan^{-1}\left(\frac{\sigma_{xy}}{\sigma_{yy}}\right)_{\theta=0,r\to 0}. \tag{18}$$

As a result of the regular singularity, this, again, is consistent with the phase angle defined for cracks in homogeneous materials. In the case of interface cracks, a material length is needed to define the phase angle.

As a starting point, we postulate that the crack starts to propagate when the energy release rate reaches a critical value Γ, the *toughness* of the FGM. The toughness is likely dependent on the material gradients, the position of the crack tip, namely h/H for the configuration shown in Fig. 1, and the mode mixity ψ. It is also possibly dependent on the propagation direction $\phi(-\pi < \phi < \pi)$ which is the angle between the propagation direction and the x axis in Fig. 1. The energy release rate is a function of the external load, elastic constants, the angle ϕ and the mode mixity ψ. Now, the fracture criterion is stated as

$$\mathcal{G} = \Gamma, \quad \frac{\partial}{\partial\phi}(\mathcal{G} - \Gamma) = 0. \tag{19}$$

The criterion also determines the propagation direction (kink angle). If toughness in the direction $\phi \neq 0$ is relatively larger than that in the direction $\phi = 0$, the crack would propagate along its original orientation. In this case, the fracture criterion is

$$\mathcal{G} = \Gamma\left(\frac{h}{H}, \psi\right). \tag{20}$$

where $\Gamma(h/H, \psi)$ is the toughness along the direction $\phi = 0$. The toughness of FGMs may be measured by experiments or obtained from micromechanics by considering their microstructures.

4. THE IN-PLANE PROBLEM

The in-plane crack problem is illustrated in Fig. 1, where a semi-infinite crack in a strip occupies the negative x axis and the crack tip is at the origin. The material properties change along the y axis. The geometry is specified by h, the distance between the crack face and the upper boundary, and H, the distance between the crack face and the lower boundary. The body extends infinitely in both the positive and negative x axes, and is loaded at the left side far behind the crack tip. The deformation far behind the crack tip consists of bending and compression in the upper arm, and bending and tension in the lower arm. The external load results in two forces which are of the same magnitude P but which act in opposite directions, and two bending moments, M and M^*. The compressive and tensile forces act at the neutral axes of the upper and lower arms, respectively. One of the two moments, M, is given independently, and the other is $M^* = M+P(\delta_1+H-\delta_2)$ by equilibrium, where δ_1 is the distance between the neutral axis of the upper arm and the crack face and δ_2 is the distance between the neutral axis of the lower arm and the lower boundary. According to the small-strain compatibility equations, the only non-zero strain, ε_{xx}, in the two arms far behind the crack tip varies linearly along the y axis.

We consider bending deformation in the two arms far behind the crack tip resulting from the two bending moments. The strain ε_{xx} can be expressed as

$$\varepsilon_{xx} = -\kappa(y-\delta_1) \tag{21}$$

in the upper arm, where κ is the curvature of the upper arm. The moment M relates to the curvature by

$$M = \kappa E_0 I_1. \tag{22}$$

In (22), I_1 is the moment of inertia and is given by

$$I_1 = \int_0^h e^{\gamma y}(y-\delta_1)^2\,dy = \frac{h^3}{12}\alpha_1(\gamma h), \tag{23}$$

where

$$\alpha_1(\gamma h) = 12\left[\frac{1}{\gamma h}\left(1-\frac{\delta_1}{h}\right)^2 e^{\gamma h} - \frac{2}{(\gamma h)^2}\left(1-\frac{\delta_1}{h}\right)e^{\gamma h} + \frac{2}{(\gamma h)^3}e^{\gamma h} - \frac{1}{\gamma h}\left(\frac{\delta_1}{h}\right)^2 - \frac{2}{(\gamma h)^2}\frac{\delta_1}{h} - \frac{2}{(\gamma h)^3}\right]. \tag{24}$$

When $\gamma = 0$, $\alpha_1 = 1$ so that $I_1 = h^3/12$, a standard result for homogeneous materials. The only non-zero stress in the arm is the normal stress in the cross section,

$$\sigma_{xx} = -\frac{M(y-\delta_1)}{I_1}e^{\gamma y}. \tag{25}$$

By the equilibrium requirement $\int_0^h \sigma_{xx}\,dy = 0$, the position of the neutral axis is obtained as

$$\frac{\delta_1}{h} = \frac{\gamma h\, e^{\gamma h} - e^{\gamma h} + 1}{\gamma h(e^{\gamma h} - 1)}. \tag{26}$$

Similarly, results for the lower arm are

$$\begin{aligned} \sigma_{xx} &= \frac{M^*(y+H-\delta_2)}{I_2}e^{\gamma h}, \\ I_2 &= \int_0^H e^{\gamma(h-H)}(y-\delta_2)^2\,dy = \frac{H^3}{12}\alpha_2, \\ \frac{\delta_2}{H} &= \frac{\gamma H\, e^{\gamma H} - e^{\gamma H} + 1}{\gamma H(e^{\gamma H} - 1)}, \end{aligned} \tag{27}$$

where

$$\alpha_2(\gamma H) = \alpha_1(\gamma H)\,\mathrm{e}^{-\gamma H}. \tag{28}$$

We next consider axial deformation in the two arms resulting from the two forces. Since the compressive force acts on the neutral axis of the upper arm, the deformation caused by it is uniform compression. The stress distribution in the cross section to produce the uniform compression is

$$\sigma_{xx} = -\frac{P\gamma}{\mathrm{e}^{\gamma h}-1}\mathrm{e}^{\gamma y}. \tag{29}$$

Similarly, the stress distribution in the cross section of the lower arm due to the tensile force is

$$\sigma_{xx} = \frac{P\gamma}{1-\mathrm{e}^{-\gamma H}}\mathrm{e}^{\gamma y}. \tag{30}$$

It is seen that in the cross sections the strains vary linearly with y, whereas the stresses vary exponentially with y. Expressions for the stresses and strains for the case that material properties change linearly along the y axis have been derived by Freund (1993) and Giannakopoulos *et al.* (1994) in studying thermal and mechanical responses in a compositionally graded layer sandwiched between two dissimilar materials without cracks, where a linear stress distribution along the thickness of the compositionally graded layer is obtained from the linear variation of material properties. Giannakopoulos *et al.* (1994) have also investigated plastic deformation in the compositionally graded layer. More recently Maewal *et al.* (1995) have developed a more general framework for analyzing thermally induced stresses in generally orthotropic FGMs with arbitrary gradients.

Having the remote field, the complex stress intensity factor K is obtained by the application of the J integral, dimension analysis and linearity consideration. The procedure is similar to that in Suo and Hutchinson (1990) for an interface crack. The complex stress intensity factor is obtained as

$$K = K_{\mathrm{I}} + iK_{\mathrm{II}} = \frac{1}{\sqrt{2}}\left(\sqrt{\frac{A}{h}}P - i\,\mathrm{e}^{i\varphi}\sqrt{\frac{I}{h^3}}M\right)\mathrm{e}^{i\omega}, \tag{31}$$

where

$$A = \gamma h\left(\frac{1}{\mathrm{e}^{\gamma h}-1} + \frac{1}{1-\mathrm{e}^{-\gamma H}}\right) + \frac{12}{\alpha_2}\left(\frac{h}{H}\frac{\delta_1}{h} + 1 - \frac{\delta_2}{H}\right)^2\frac{h}{H},$$

$$I = \frac{12}{\alpha_1} + \frac{12}{\alpha_2}\left(\frac{h}{H}\right)^3,$$

$$\sin\varphi = \frac{12}{\alpha_2\sqrt{AI}}\left(\frac{h}{H}\frac{\delta_1}{h} + 1 - \frac{\delta_2}{H}\right)\left(\frac{h}{H}\right)^2. \tag{32}$$

In (31), $\omega = \omega(\gamma h, h/H)$ is to be determined, and is in the range $0 \leqslant \omega \leqslant \pi/2$. The complex stress intensity factor is fully obtained apart from the dimensionless real scalar $\omega(\gamma h, h/H)$. The expression for K has a similar form as that for an interface crack. In the interface crack case, Dundurs' parameters enter the solution as variables of A, I, φ and ω, whereas the material constant γ enters the solution as a variable of those parameters in our case.

To determine $\omega(\gamma h, h/H)$, we solve the full boundary value problem for given γh and h/H, using the integral equation method. Integral equations for this problem can be obtained by Fourier transforms. The numerical procedure is to distribute dislocation densities simulating opening and sliding displacements of the crack in terms of Chebyshev polynomials, Table 1. $\omega(\gamma h, h/H)$ (in degrees)

	γh											
h/H	0.2	0.4	0.6	0.8	1.0	1.2	1.4	1.6	1.8	2.0	2.2	2.4
0.0	53.8	54.9	56.0	56.9	57.5	58.0	58.3	58.5	58.6	58.6	58.5	58.4
0.1	53.5	54.8	56.0	56.9	57.5	58.0	58.3	58.5	58.6	58.6	58.5	58.4
0.5	51.6	52.4	53.2	54.0	54.7	55.3	55.9	56.4	56.8	57.1	57.4	57.5
1.0	49.6	50.1	50.7	51.2	51.7	52.2	52.7	53.1	53.5	53.8	54.1	54.4
2.0	47.0	47.3	47.6	47.9	48.2	48.5	48.8	49.1	49.4	49.6	49.9	50.2
10	40.8	40.9	40.9	41.0	41.1	41.2	41.2	41.3	41.4	41.5	41.6	41.7
100	39.0	39.0	39.0	39.1	39.1	39.1	39.1	39.1	39.1	39.1	39.1	39.1

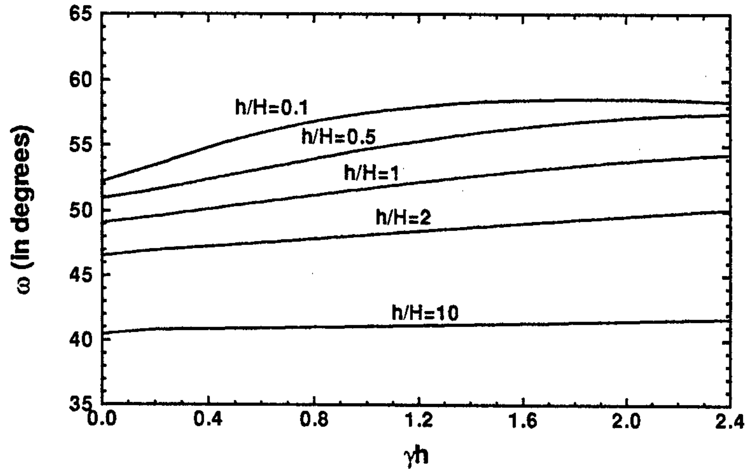

Fig. 2. Numerical results for $\omega(\gamma h, h/H)$.

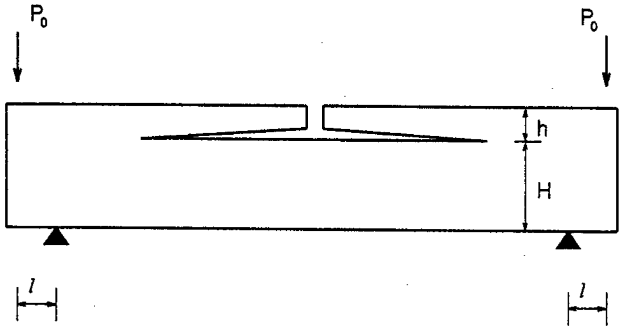

Fig. 3. A four-point bending specimen.

and to adjust the coefficients of these polynomials to satisfy the integral equations which are expressions of equilibrium (see Thouless *et al.*, 1987). Table 1 gives numerical results for ω when $0 \leqslant \gamma h \leqslant 2.4$ and $h/H = 0, 0.1, 0.5, 1, 2, 10$ and 100, which are also shown in Fig. 2. For most cases, the ω increases as γh increases, and the increase is larger for smaller h/H. For $h/H = 100$, the numerical solution shows little change of ω when γh varies between 0 and 2.4.

When $M = 0$, the phase angle $\psi = \omega$; when $P = 0$ (double-cantilever beam), $\psi = \omega + \varphi - 90°$. A four-point bending specimen configuration shown in Fig. 3 can be reduced to the present problem by cutting it from the middle. By a superposition scheme (Suo and Hutchinson, 1990) and above deformation analysis, the force P and the moment M are

$$P=\frac{P_0 l}{I}\int_0^h (y+H-\delta_3)\,e^{\gamma y}\,dy,$$

$$M=\frac{P_0 l}{I}\int_0^h (y+H-\delta_3)(y-\delta_1)\,e^{\gamma y}\,dy, \tag{33}$$

where

$$I=\int_0^{H+h}(y-\delta_3)^2\,e^{\gamma(y-H)}\,dy. \tag{34}$$

In (33) and (34), δ_3 is the neutral axis of the right side of the plate, and is given by replacing h by $H+h$ in (26). Figure 4 shows that the phase angle and the magnitude of the complex stress intensity factor for the four-point bending specimen. The phase angle varies as γh varies between 0 and 2.4. The variation is larger for smaller h/H, and is quite small when h/H increases to 10. The magnitude of the complex stress intensity factor increases as γh increases, and significantly increases as h/H increases. Figure 5 shows the phase angle and the magnitude of the complex stress intensity of the double-cantilever beam. In this figure,

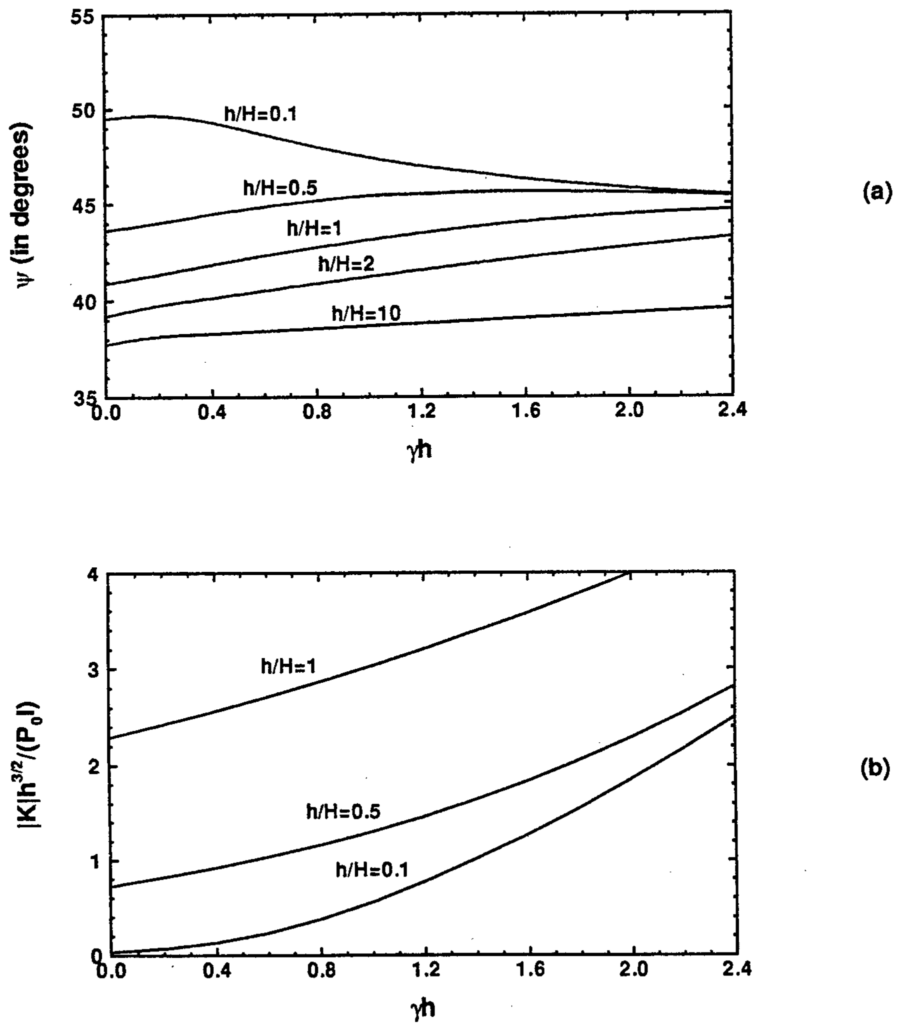

Fig. 4. The phase angle ψ and the magnitude of the complex stress intensity factor $|K|$ for four-point bending specimen.

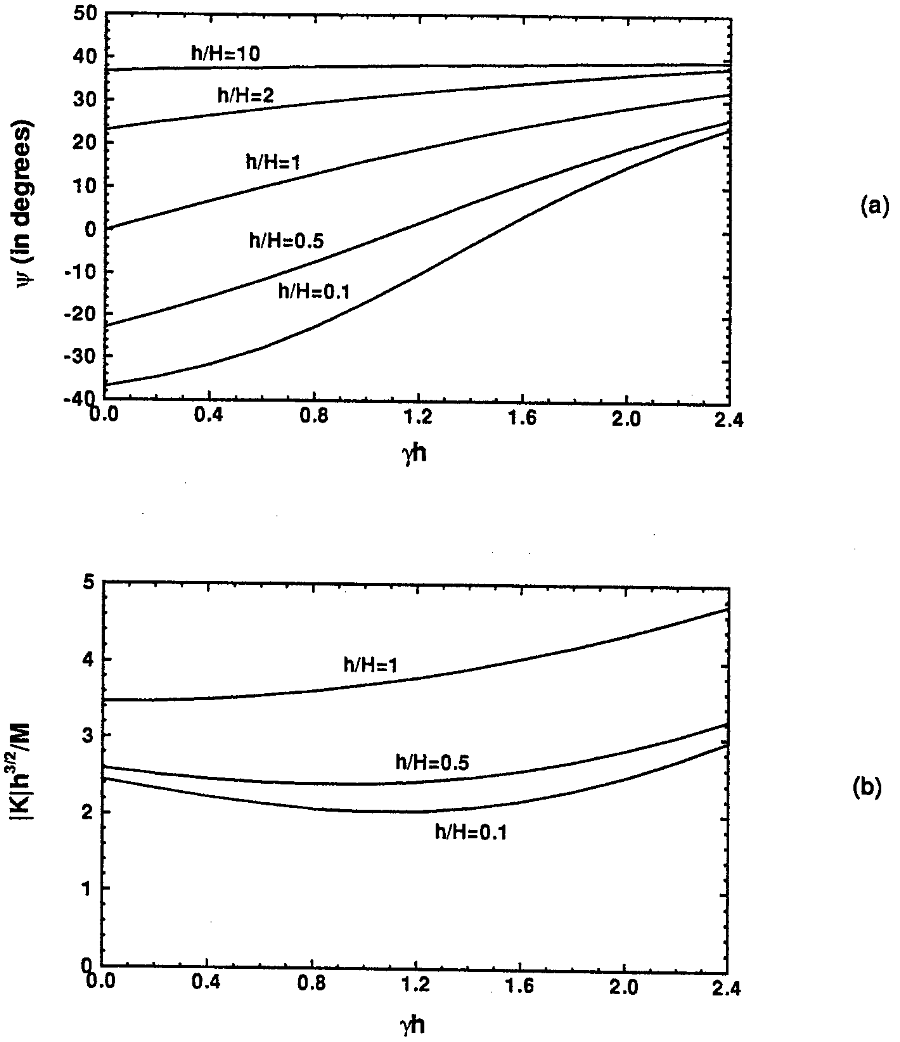

Fig. 5. The phase angle ψ and the magnitude of the complex stress intensity factor $|K|$ for double-cantilever beam.

the phase angle increases as γh or h/H increases. Similar to Fig. 5(a), the variation of the phase angle for γh between 0 and 2.4 is insignificant when h/H increases to 10.

The ratio of the Young's moduli of the two material phases in a FGM, E_u' and E_l', is usually less than 10. From (5),

$$\gamma h = \frac{\ln (E_u'/E_l')}{1+H/h} \leqslant \ln 10 < 2.4. \tag{35}$$

This tells us that the numerical results for γh between 0 and 2.4 given here provide a complete solution for the semi-infinite crack in FGMs, shown in Fig. 1.

To obtain a quantitative feel for the behavior of the solution, consider the double-cantilever beam (*i.e.*, $P = 0$) with $E_u'/E_l' = 7$. If $h/H = 1$, from (35), $\gamma h \approx 1$. The stress intensity factors are $K_I h^{3/2}/M = 3.55$ and $K_{II} h^{3/2}/M = 1.02$, whereas for a homogeneous material with $h/H = 1$, they are 3.46 and 0, respectively. If $h/H = 0.1$, $\gamma h \approx 0.18$. The stress intensity factors are $K_I h^{3/2}/M = 1.92$ and $K_{II} h^{3/2}/M = -1.34$, whereas for a homogeneous material with $h/H = 0.1$, they are 1.96 and -1.47, respectively. If $h/H = 10$, $\gamma h \approx 1.8$. The stress intensity factors are $K_I h^{3/2}/M = 63.23$ and $K_{II} h^{3/2}/M = 50.71$, whereas for a homogeneous material with $h/H = 10$, they are 62.09 and 46.52, respectively. This shows that the change of K_{II} is larger than that of K_I due to the change of material gradients. Also, the stress intensity factors at $E'_u/E'_l = 7$ are larger than those of a homogeneous material except the case for $h/H = 0.1$.

For the four-point bending configuration with $E'_u/E'_l = 7$ and $h/H = 1$, the stress intensity factors are $K_I h^{3/2}/(P_0 l) = 2.21$ and $K_{II} h^{3/2}/(P_0 l) = 2.07$; they are 1.73 and 1.50, respectively, for a homogeneous material. If $h/H = 0.1$, the stress intensity factors are $K_I h^{3/2}/(P_0 l) = 0.05$ and $K_{II} h^{3/2}/(P_0 l) = 0.06$; they are 0.03 and 0.03, respectively, for a homogeneous material. If $h/H = 10$, the stress intensity factors are $K_I h^{3/2}/(P_0 l) = 62.79$ and $K_{II} h^{3/2}/(P_0 l) = 51.21$; they are 61.30 and 47.45, respectively, for a homogeneous material. Similar to the double-cantilever beam, the change of K_{II} is larger than that of K_I due to the change of material gradients; and the stress intensity factors at $E'_u/E'_l = 7$ are larger than those of a homogeneous material.

5. SOLUTION FOR ORTHOTROPIC, FUNCTIONALLY GRADED MATERIALS

In this section, we consider the strip in Fig. 1 is made of an orthotropic, functionally graded material. The problem is solved by orthotropy rescaling. In general, there are three material gradients associated with two Young's moduli and one shear modulus. The moduli can be written in following forms

$$\begin{aligned} E'_1(y) &= E_{10}\,e^{\gamma_1 y}, \\ E'_2(y) &= E_{20}\,e^{\gamma_2 y}, \\ \mu_{12}(y) &= \mu(y)\,e^{\gamma_3 y}, \end{aligned} \tag{36}$$

where γ_1, γ_2 and γ_3 are material constants; E_{10} and E_{20} are $E'_1(y)$ and $E'_2(y)$ at $y = 0$, respectively; $\mu_{12}(y)$ is the shear modulus in the x–y plane. For plane stress problems, $E'_1(y) = E_1(y)$ and $E'_2(y) = E_2(y)$, with $E_1(y)$ and $E_2(y)$ being Young's moduli in the directions parallel to the x axis and the y axis, respectively. For plane strain problems, $E'_1(y) = E_1(y)/[1-\nu_{13}(y)\nu_{31}(y)]$ and $E'_2(y) = E_2(y)/[1-\nu_{23}(y)\nu_{32}(y)]$, with $\nu_{13}(y)$ and $\nu_{31}(y)$, and $\nu_{23}(y)$ and $\nu_{32}(y)$ being four Poisson's ratios in the x–z and y–z planes, respectively. For isotropic materials, the elastic properties in (36) reduce to those in (1) and (2). The variation of Poisson's ratios can also be written in the exponential form similar to that of the Poisson's ratio in (1) for isotropic materials.

We consider a special set of elastic properties, which is given by

$$\begin{aligned} \gamma_1 &= \gamma_2 = \gamma_3 = \gamma, \\ \nu'_{21}(h) &= \nu_{210}(1+\varepsilon y)\,e^{\gamma y}, \\ \nu'_{12}(y) &= \nu_{120}(1+\varepsilon y)\,e^{\gamma y}, \\ \mu_{12}(y) &= \frac{E'_2(y)}{2[\sqrt{\lambda}+\nu'_{21}(y)]}, \end{aligned} \tag{37}$$

whereas ν_{210} and ν_{120} are $\nu'_{21}(y)$ and $\nu'_{12}(y)$ at $y = 0$, respectively; ε is a constant; and

$$\lambda = \frac{E_{20}}{E_{10}}. \tag{38}$$

For plane stress problems, $\nu'_{21}(y) = \nu_{21}(y)$ and $\nu'_{12}(y) = \nu_{12}(y)$, with $\nu_{21}(y)$ and $\nu_{12}(y)$ being two Poisson's ratios in the x–y plane. For plane strain problems, $\nu'_{12}(y) = [\nu_{12}(y)+\nu_{13}(y)\nu_{32}(y)][1-\nu_{13}(y)\nu_{31}(y)]$, and $\nu'_{21}(y) = [\nu_{21}(y)+\nu_{23}(y)\nu_{31}(y)]/[1-\nu_{23}(y)\nu_{32}(y)]$. These forms for the material properties of orthotropic, functionally graded materials provide analytical flexibility, and lead to somewhat simple forms for the field equations.

Using this set of elastic properties, the stress function $\Phi(x, y)$ satisfies the following equation

$$\frac{\partial^4 \Phi}{\partial x^4} + 2\sqrt{\lambda}\frac{\partial^4 \Phi}{\partial x^2 \partial y^2} + \lambda \frac{\partial^4 \Phi}{\partial y^4} - 2\gamma\sqrt{\lambda}\frac{\partial^3 \Phi}{\partial x^2 \partial y} - 2\gamma\lambda\frac{\partial^3 \Phi}{\partial y^3} + \gamma^2 \lambda \frac{\partial^2 \Phi}{\partial y^2} = 0. \tag{39}$$

Making a variable change

$$x = \lambda^{-1/4}\xi, \tag{40}$$

eqn (39) becomes

$$\frac{\partial^4 \Phi}{\partial \xi^4} + 2\frac{\partial^4 \Phi}{\partial \xi^2 \partial y^2} + \frac{\partial^2 \Phi}{\partial y^4} - 2\gamma\frac{\partial}{\partial y}\left(\frac{\partial^2 \Phi}{\partial \xi^2} + \frac{\partial^2 \Phi}{\partial y^2}\right) + \gamma^2 \frac{\partial^2 \Phi}{\partial y^2} = 0 \tag{41}$$

in the ξ–y plane. The above equation shows the orthotropy rescaling (Suo *et al.*, 1991) works for nonhomogeneous materials which obey (36) and (37), since it is the same as eqn (3) for isotropic materials. Stresses in terms of $\Phi(\xi, y)$ are

$$\sigma_{xx} = \frac{\partial^2 \Phi}{\partial y^2}, \quad \lambda^{-1/2}\sigma_{yy} = \frac{\partial^2 \Phi}{\partial \xi^2}, \quad \lambda^{-1/4}\sigma_{xy} = -\frac{\partial^2 \Phi}{\partial \xi\, \partial y}. \tag{42}$$

Stress intensity factors are expressed as

$$\begin{aligned} \lambda^{-3/8} K_{\mathrm{I}} &= \lim_{\xi \to 0, y=0} \sqrt{2\pi\xi}\frac{\partial \Phi}{\partial \xi^2}, \\ \lambda^{-1/8} K_{\mathrm{II}} &= -\lim_{\xi \to 0, y=0} \sqrt{2\pi\xi}\frac{\partial^2 \Phi}{\partial \xi\, \partial y}. \end{aligned} \tag{43}$$

According to above analysis and the solution for isotropic materials in Section 4, the stress factors to the orthotropic problem are given by

$$\lambda^{-3/8} K_{\mathrm{I}} + i\lambda^{-1/8} K_{\mathrm{II}} = \frac{1}{\sqrt{2}}\left(\sqrt{\frac{A}{h}}P - i\,\mathrm{e}^{i\varphi}\sqrt{\frac{I}{h^3}}M\right)\mathrm{e}^{i\omega}. \tag{44}$$

where A, I, φ and ω are the same as those in the solution for isotropic materials in Section 4.

From above expression, K_{I} and K_{II} are those of the isotropic solution modified by multipliers $\lambda^{3/8}$ and $\lambda^{1/8}$, respectively. The phase angle of the orthotropic problem, ψ_{orth}, relates to that of the corresponding isotropic problem, ψ_{is}, by

$$\tan(\psi_{\mathrm{orth}}) = \lambda^{-1/4}\tan(\psi_{\mathrm{is}}). \tag{45}$$

The effects of λ on the crack-tip field depend on its value. When $\lambda > 1$, the stress intensity factors are larger than those of the isotropic case, and the phase angle is smaller than that of the isotropic case; and when $\lambda < 1$, the stress intensity factors are smaller than those of

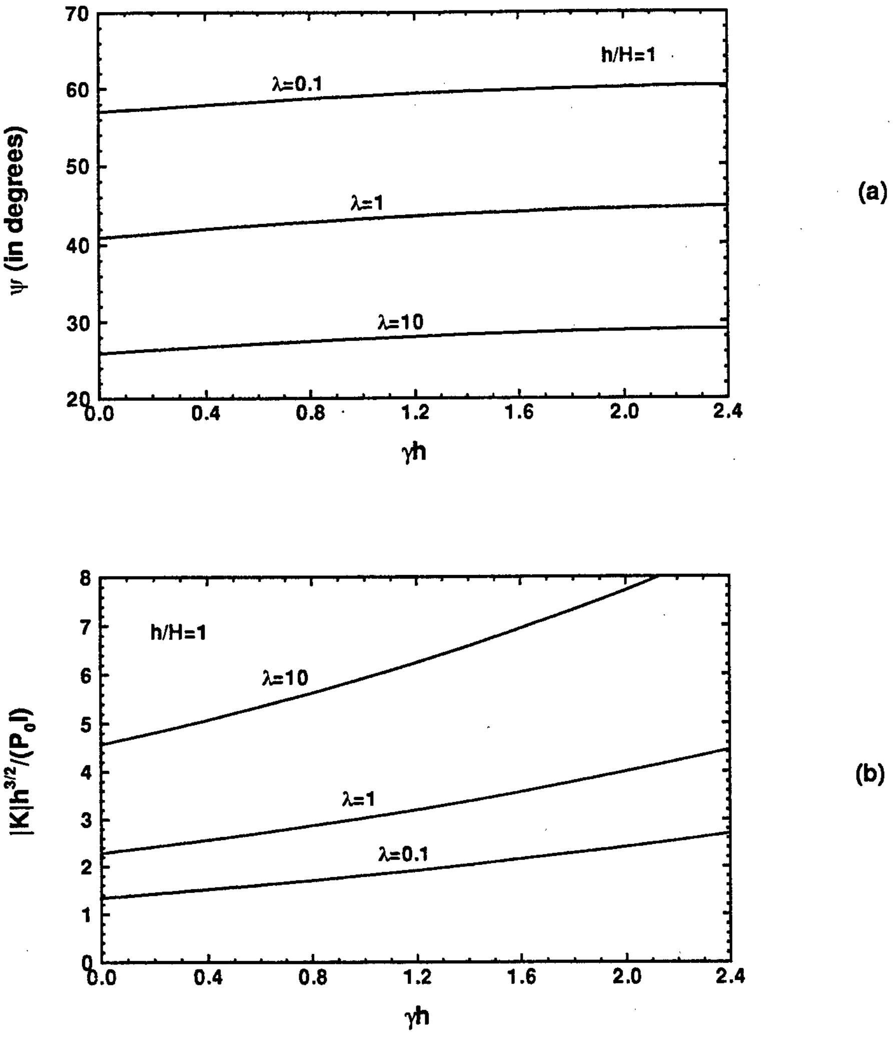

Fig. 6. The effects of λ on the phase angle and the magnitude of the complex stress intensity factor $|K|$ for four-point bending specimen.

the isotropic case, and the phase angle is larger than that of the isotropic case. For the four-point bending specimen configuration, these effects of λ are shown in Fig. 6.

6. THE ANTI-PLANE PROBLEM

The cracked strip shown in Fig. 1 subjected to anti-plane deformation (mode III problem) is considered in this section. For the mode III problem, we take the shear modulus in the following form

$$\mu(y) = \mu_0 \, e^{\gamma y}, \tag{46}$$

where μ_0 is the shear modulus at $y = 0$ and γ represents the material gradient. The strip is loaded at the left side far behind the crack tip, and the traction is

$$\sigma_{xz} = -\sigma_1 \, e^{\gamma y} \tag{47}$$

for $x \to -\infty$ and $y > 0$, and

$$\sigma_{xz} = \sigma_2 \, e^{\gamma y} \tag{48}$$

for $x \to -\infty$ and $y < 0$. The traction produces two uniform strains,

$$\varepsilon_{xz} = -\frac{\sigma_1}{2\mu_0} \tag{49}$$

for $x \to -\infty$ and $y > 0$, and

$$\varepsilon_{xz} = \frac{\sigma_2}{2\mu_0} \tag{50}$$

for $x \to -\infty$ and $y < 0$. From the equilibrium requirement,

$$P = \int_0^h \sigma_{xz} \, dy = \int_{-H}^0 \sigma_{xz} \, dy, \tag{51}$$

and (47) and (48), we have

$$\sigma_1 = \frac{P\gamma}{e^{\gamma h} - 1}, \qquad \sigma_2 = \frac{P\gamma}{1 - e^{-\gamma H}}. \tag{52}$$

Having the remote field, the stress intensity factor K_{III} is readily obtained from the J integral as

$$K_{\mathrm{III}} = \frac{P}{\sqrt{h}} \sqrt{\frac{\gamma h}{e^{\gamma h} - 1}\left(1 + \frac{e^{\gamma h} - 1}{1 - e^{-\gamma H}}\right)}. \tag{53}$$

The normalized stress intensity factor $K_{\mathrm{III}}\sqrt{h}/P$, which is equal to the second square root in above equation, is only related to the dimensionless group, γh and γH. It increases as γ increases. When $\gamma = 0$, the stress intensity factor recovers the solution for a homogeneous material; when $\gamma = \infty$ or $H = 0$, it is unbounded. A plot of the stress intensity factor is shown in Fig. 7.

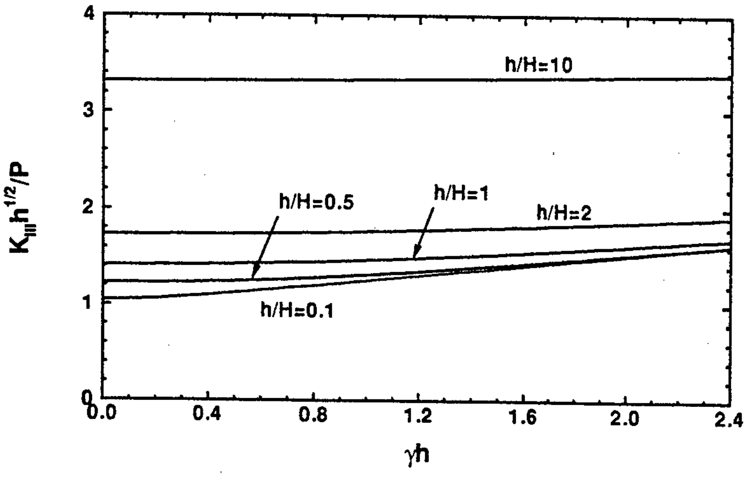

Fig. 7. The stress intensity factor K_{III} for the anti-plane problem.

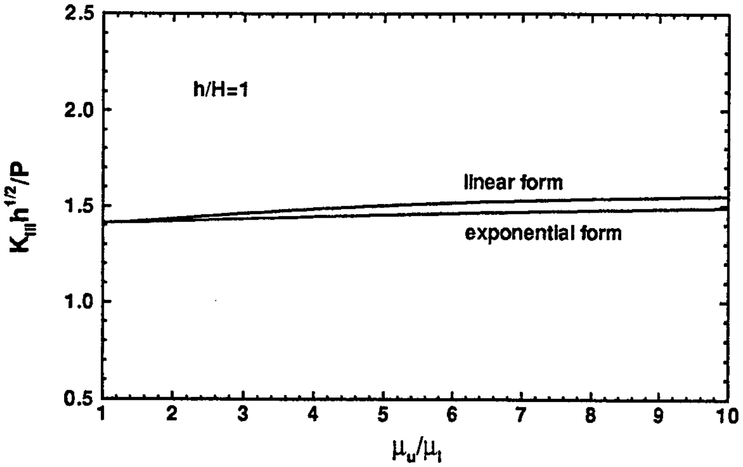

Fig. 8. A comparison of stress intensity factors obtained from different forms of the shear modulus.

When the shear modulus varies linearly along the y axis, it is written as

$$\mu(y) = \frac{\mu_u - \mu_l}{h+H} y + \frac{\mu_u H + \mu_l h}{h+H}, \tag{54}$$

where μ_u and μ_l are shear moduli at the upper and lower boundaries of the strip, respectively. The stress intensity factor for the linear variation of the shear modulus is

$$K_{\mathrm{III}} = \frac{P}{\sqrt{h}} \sqrt{\frac{2(r+\eta)}{r\eta+2r+\eta}\left(1+\eta\frac{r\eta+2r+\eta}{r+2\eta+1}\right)}, \tag{55}$$

where $r = \mu_u/\mu_l$ and $\eta = h/H$. A comparison of the stress intensity factor obtained from the linear variation of the shear modulus with that from the exponential variation of the shear modulus is shown in Fig. 8 for $h/H = 1$. The results show that the difference between them is quite small, less than 5% in the range considered. When the crack moves to the ceramic side, the difference between the two solutions becomes smaller, and when it moves to the metal side the difference becomes larger. The difference is less than 0.4% for $h/H = 0.1$; and is less than 8% for $h/H = 10$.

7. DISCUSSION

A complete solution to a semi-infinite crack in a strip of an isotropic, functionally graded material is obtained. It is shown that material gradients have strong effects on the stress intensity factors and the phase angle. For the double-cantilever beam, the mode I stress intensity factor is 3.55 and the mode II stress intensity factor is 1.02, when the crack is at the middle of the strip ($h/H = 1$) and the ratio of the Young's modulus at the upper boundary to that at the lower boundary is 7; for homogeneous material with the same geometry, they are 3.46 and 0, respectively. For the four-point bending specimen configuration, the mode I stress intensity factor is 2.21 and the mode II stress intensity factor is 2.07, when the crack is at the middle of the beam ($h/H = 1$) and the ratio of the Young's modulus at the upper boundary to that at the lower boundary is 7; for a homogeneous material with the same geometry, the two stress intensity factors are 1.73 and 1.50, respectively. These results show that the increase of the mode II stress intensity factor due to the increase of the material gradients is significant, in other words, the mode II stress intensity factor plays an important role in the fracture of FGMs.

The solution for isotropic materials is extended to orthotropic, functionally graded materials by orthotropy rescaling. The effects of the orthotropy on stress intensity factors and the phase angle are explicitly shown in the orthotropic solution. In the orthotropic solution, since we assume a special set of material properties, the orthotropy is measured by one parameter, the ratio of the Young's modulus in the direction of material property variation to that in the direction perpendicular to the above property variation direction. For general orthotropic, functionally graded materials, there are other parameters in addition to the ratio for characterizing the orthotropy. However, it seems that the ratio is the most important parameter to be considered.

The crack propagation is the competition between the driving force, the energy release rate, and the toughness of the material, *i.e.*. a crack starts to extend when the former one exceeds the latter one. The FGMs are expected to have considerably larger toughness than corresponding bimaterials because there are no large weak planes, such as interfaces, *e.g*, a layered structure with compositionally graded interlayers is expected to have a larger toughness than that obtained by bonding these layers with sharp interfaces. On the other hand, the energy release rate of a FGM is at the same level as that of the corresponding bimaterial. Consider a bimaterial which has the same configuration as the FGM shown in Fig. 1; above the x axis is material #1 with Young's modulus E'_u and below the x axis is material #2 with Young's modulus E'_l. Figure 9 shows the comparison of the energy release rate of the FGM with that of the bimaterial for the double-cantilever beam when $0 \leqslant h/H \leqslant 2$. In the calculation, $E'_u/E'_l = 7$, and the Poisson's ratios of the two bulk materials forming the bimaterial are taken to be 0.3. For the bimaterial, the two Dundurs' parameters are $\alpha = 0.75$ and $\beta = 0.21$. Our calculation shows, at $h/H = 1$, the energy release rate is 13.55 for the FGM, whereas it is 16.51 for the bimaterial; at $h/H = 0.1$, they are 5.51 and 4.61 for the FGM and the bimaterial, respectively; at $h/H = 10$, they are 6559 and 6517 for the FGM and the bimaterial, respectively. When the crack is at the middle of the plate ($h/H = 1$), the energy release rate of the FGM is smaller than that of the bimaterial; when the crack is very close to the upper or lower boundary, the former one is larger than the latter one. But in any case, the two energy release rates are at the same level. This fact reveals one of the advantages of using FGMs, *i.e.*, FGMs can be subjected to higher external loads than corresponding bimaterials.

The crack propagation direction follows different criteria for different kinds of materials. For homogeneous materials, a crack propagates along the direction in which the mode II stress intensity factor is vanished, and the toughness is independent of the propagation direction and the mode mixity. For bimaterials, the propagation direction of an interface crack is decided by the driving force and the toughness of the interface and the two bulk materials. If the toughness of the bulk materials is relatively large, the interface crack would extend along the interface, otherwise, kinking is favored. For FGMs, their toughness is likely dependent on the material gradients, the position of the crack tip, the

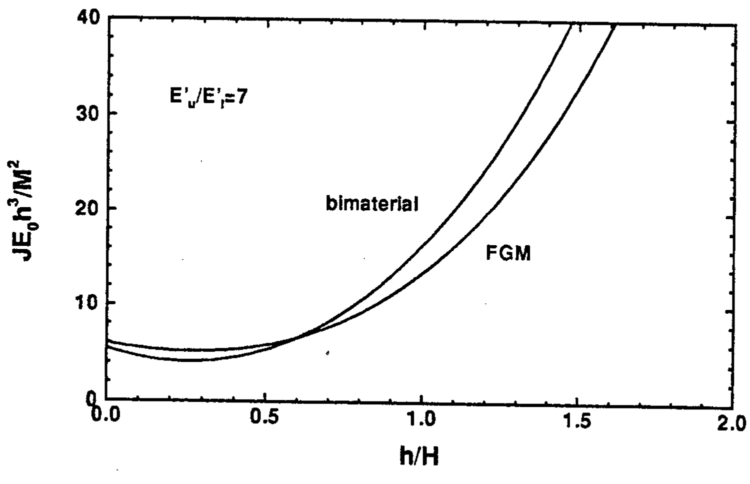

Fig. 9. A comparison of the energy release rate of the FGM with that of the corresponding bimaterial.

propagation direction and the mode mixity. From a continuum point of view, the propagation direction is the direction at which the difference of the energy release rate and the toughness reaches a maximum value, as discussed at the end of Section 3. For complete understanding of the fracture behavior of FGMs and a fully rationalized FGM characterization, experiments need to be carried out and more specimen configurations need to be calibrated.

Acknowledgements—This work is supported by the Office of Naval Research through Grant N00014-93-1-1164.

REFERENCES

Delale, F. and Erdogan, F. (1993). The crack problem for a nonhomogeneous plane. *J. Appl. Mech.* **50,** 609–614.

Delale, F. and Erdogan, F. (1988). On the mechanical modeling of the interfacial region in bonded half-planes. *J. Appl. Mech.* **55,** 317–324.

Dundurs, J. (1969). Edge-bonded dissimilar orthogonal elastic wedges. *J. Appl. Mech.* **36,** 650–652.

Freund, L. B. (1993). The stress distribution and curvature of a general compositionally graded semiconductor layer. *J. Crystal Growth* **132,** 341–344.

Giannakopoulos, A. E., Suresh, S., Finot, M. and Olsson, M. (1995). Elastoplastic analysis of thermal cycling: layered materials with compositional gradients. *Acta Metall.* **43,** 1335–1354.

Holt, J. B., Koizumi, M., Hirai, T. and Munir, Z. A. (eds) (1993). Functionally gradient materials. *Ceramic Transactions*, Vol. 34, The American Ceramic Society, Westerville, OH.

Jin, Z. and Noda, N. (1994). Crack-tip singular fields in nonhomogeneous materials. *J. Appl. Mech.* **61,** 738–740.

Maewal, A., Asaso, R. J. and Dao, M. (1995). Residual stresses in thin film structures with functionally graded materials. In preparation.

Noda, N. and Jin, Z. (1993). Thermal stress intensity factors for a crack in a strip of a functionally gradient material. *Int. J. Solids Structures* **30,** 1039–1056.

Rice, J. R. (1968). A path independent integral and approximate analysis of strain concentration by notches and cracks. *J. Appl. Mech.* **35,** 379–386.

Suo, Z. and Hutchinson, J. W. (1990). Interface crack between two elastic layers. *Int. J. Fract.* **43,** 1–18.

Suo, Z., Bao, G., Fan, B. and Wang, T. C. (1991). Orthotropy rescaling and implications for fracture in composites. *Int. J. Solids Structures* **28,** 235–248.

Thouless, M. D., Evans, A. G., Ashby, M. F. and Hutchinson, J. W. (1987). The edge cracking and spalling of brittle plates. *Acta Metall.* **35,** 1333–1341.

Yamanouchi, M., Koizumi, M., Hirai, T. and Shiota, I. (eds) (1990). *Proceedings of the First International Symposium on Functionally Gradient Materials*, Sendai, Japan.

Yang, W. and Shih C. F. (1994). Fracture along an interlayer. *Int. J. Solids Structures* **31,** 985–1002.

Pergamon

Acta mater. Vol. 45, No. 8, pp. 3265–3276, 1997
© 1997 Acta Metallurgica Inc.
Published by Elsevier Science Ltd. All rights reserved
Printed in Great Britain
PII: S1359-6454(96)00405-3
1359-6454/97 $17.00 + 0.00

A MICROMECHANICAL STUDY OF RESIDUAL STRESSES IN FUNCTIONALLY GRADED MATERIALS

MING DAO, PEI GU, AKHILESH MAEWAL and R. J. ASARO
Department of Applied Mechanics and Engineering Sciences, 0411, University of California, San Diego, La Jolla, CA 92093, U.S.A.

(Received 11 June 1996; accepted 27 November 1996)

Abstract—A physically based computational micromechanics model is developed to study *random* and *discrete* microstructures in functionally graded materials (FGMs). The influences of discrete microstructure on residual stress distributions at grain size level are examined with respect to material gradient and FGM volume percentage (within a ceramic–FGM–metal three-layer structure). Both thermoelastic and thermoplastic deformation are considered, and the plastic behavior of metal grains is modeled at the single crystal level using crystal plasticity theory. The results are compared with those obtained using a continuous model which does not consider the microstructural randomness and discreteness. In an *averaged* sense both the micromechanics model and the continuous model give practically the same macroscopic stresses; whereas the discrete micromechanics model predicts fairly high residual stress concentrations at the grain size level (i.e. higher than 700 MPa in 5–6 vol% FGM grains) with only a 300°C temperature drop in a Ni–Al_2O_3 FGM system. Statistical analysis shows that the residual stress concentrations are insensitive to material gradient and FGM volume percentage. The need to consider microstructural details in FGM microstructures is evident. The results obtained provide some insights for improving the reliability of FGMs against fracture and delamination. © *1997 Acta Metallurgica Inc.*

1. INTRODUCTION

Functionally graded materials (FGMs) are spatial composites within which the composition of each of the two material phases that form the FGMs varies along their thickness direction. The variation is designed to be tailorable so as to achieve predetermined responses to given mechanical and thermal–mechanical loadings. Within a FGM, the different material phases have different functions. In a metal–ceramic FGM, the metal-rich side is placed in the region where mechanical performance, such as toughness, needs to be stronger; and the ceramic-rich side, which has better thermal resistance, is exposed to high temperatures, or placed in the region where there is a potentially severe temperature variation. Also, FGMs can reduce the thermal mismatch at the interfaces of bimaterials and, therefore, largely reduce the possibility of fracture caused by the mismatch. Applications of FGMs include aerospace, power generation, furnaces and others where strong material performance, especially the ability to resist thermal shock, is required or expected.

Material gradients, induced by the change in material properties, make FGMs different in behavior from homogeneous materials and traditional composite materials. Over the past few years, there have been a number of works, both theoretical and experimental, to study the responses of FGMs to mechanical and thermal loads under various loading conditions, for various geometries and in various deformation and fracture mechanisms, including elastic and plastic aspects and crack propagation [1–11]. Most of the previous studies above focused on the continuous approach which considers that the material properties change continuously, as shown in Fig. 1(b). The continuous model gives correct solutions to such problems as elastic deformation in the ceramic-rich side and plastic deformation in the metal-rich side, when the scale considered is much larger than that of the grain sizes of the constituent material phases. It also gives a good prediction for damage initiation from an imperfection, such as a void or crack, when the size of the imperfection is much larger than the grain size.

The microstructures in FGMs are *discrete* and *random* in nature, as schematically shown in Fig. 1(a). The strongly heterogeneous microstructure is likely, at least possible, to cause locally concentrated residual stresses during thermal or mechanical loading. These locally concentrated stresses, especially those high in tension, may act to initiate small cracks and voids. The development of these small-scale failures may lead to large-scale failures and result in the fracture of the whole structure. Experiments on Si–C FGM by Sohda *et al.* [11] showed that the porous microstructure has a much better resistance against delamination and crack propagation than the companion dense microstructure, where the latter has a higher level of local stresses. Also pointed out by Finot *et al.* [6], to study the local stress distributions and concentrations within the FGM, microstructural details such as the heterogeneous microstructure and local plastic deformation must be considered carefully. The objective of this study is, therefore, to explore the microstructural *randomness* and *discreteness* vs macroscopic material gradients and geometries with respect to the thermal residual stresses and local residual stress concentrations within FGM microstructures. A discrete computational micromechanics model is developed. In our discrete micromechanics model, the ceramic grains are treated to be elastically deformed as the typical ceramic materials; the metal grains undergo thermo-elastoplastic, finite deformation, and are treated using crystal plasticity theory. The results, as will be seen in the later sections, show that local stress concentration at the grain size level is significant. For the purpose of comparison, we also solve the problem by the continuous model.

The plan of the paper is as follows. Both the continuous and discrete models are described in Section 2, where a brief description is given of the crystal plasticity theory used for metal grains. Numerical results are presented in Section 3. In Section 3.1, results using the continuous model are presented, where influences of different gradients on macroscopic residual stresses are reviewed. In Section 3.2, results using the discrete micromechanics model are presented, the macroscopic residual stresses as well as the local stress concentrations are explored using different material gradients and FGM volume percentages. In Section 3.3, the contribution of plastic deformation within the discrete micromechanics model is studied. In Section 3.4, a short summary is given on the statistical analysis of the residual stress concentrations with respect to material gradient, FGM volume percentage as well as the plastic relaxation. Finally, discussions and conclusions follow in Section 4.

2. THE CONTINUOUS AND DISCRETE MODELS

The model geometry, as shown in Fig. 2, consists of three layers: the ceramic layer is on the left side; the metal layer is on the right side; and the FGM is sandwiched between them. As a model system, we choose the metal to be Ni, and the ceramic to be Al_2O_3 in this study. The FGM is, therefore, Ni–Al_2O_3 FGM. Both continuous and discrete models for the FGM, including the numerical consideration, are described below.

2.1. *The continuous model*

We define x as the relative distance from the ceramic–FGM interface, i.e. $x = 0$ stands for the ceramic–FGM interface and $x = 1$ stands for the FGM–metal interface. For the continuous model for the FGM, the effective material properties are assumed to follow the "rule of mixture":

$$A(x) = V_{\mathrm{Metal}}(x)A_{\mathrm{Metal}} + V_{\mathrm{Ceramic}}(x)A_{\mathrm{Ceramic}}, \qquad (1)$$

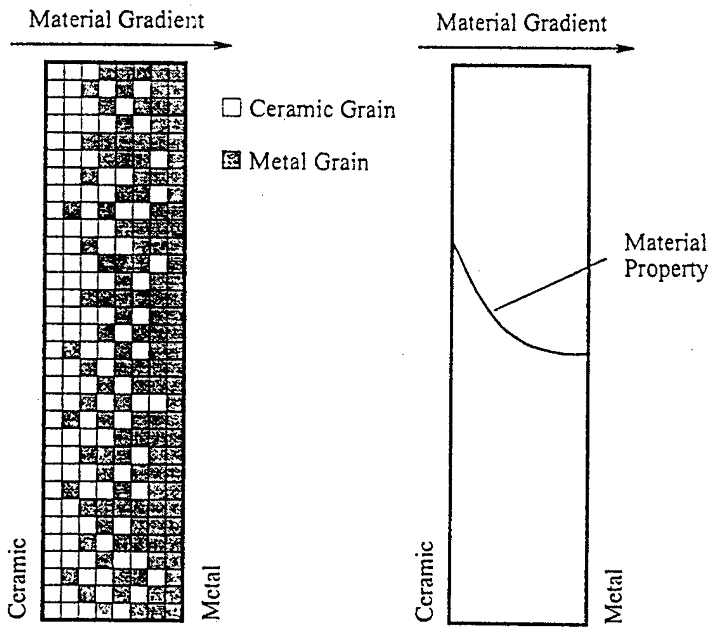

(a) Discrete Microstructure (b) Continuous Model

Fig. 1. Schematic drawings of functionally graded materials (FGMs): (a) discrete and random microstructure in reality, and (b) continuous gradient modeling often used.

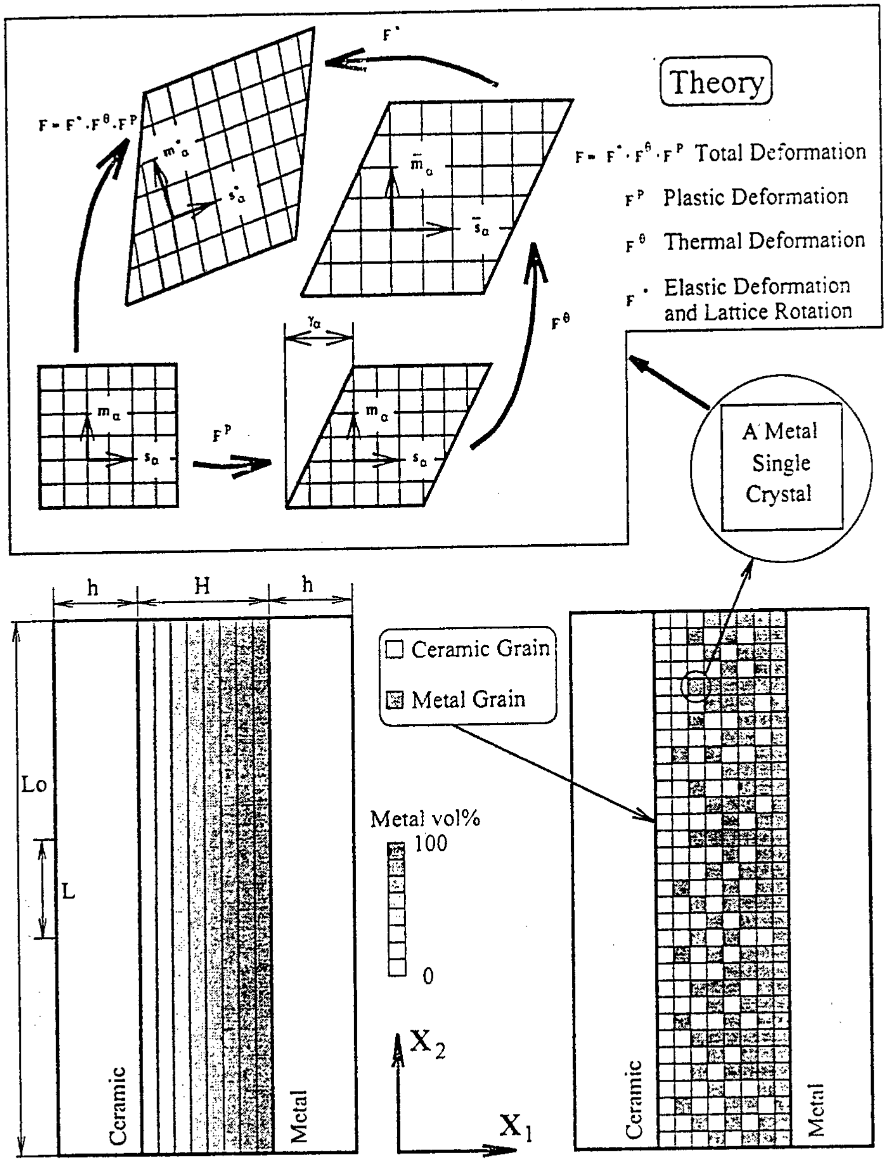
Theory
$F = F^* \cdot F^\theta \cdot F^P$ Total Deformation
F^P Plastic Deformation
F^θ Thermal Deformation
F^* Elastic Deformation and Lattice Rotation
$F = F^* \cdot F^\theta \cdot F^P$
F^*
F^θ
F^P
m_α
s_α
$\bar{m}_\alpha$
$\bar{s}_\alpha$
m^*_α
s^*_α
γ_α
A Metal Single Crystal
h
H
h
Lo
L
Ceramic
Metal
□ Ceramic Grain
▨ Metal Grain
Metal vol%
100
0
X_2
X_1
Ceramic
Metal

(a) Continuous Model

(b) Micromechanics Model

Fig. 2. Schematic drawings of ceramic–FGM–metal three-layer structures used to model the functionally graded materials, with (a) continuous model and (b) discrete micromechanics model. The insert to (b) shows the deformation gradient decomposition for a metal single crystal.

where A stands for either the elastic constants, E (Young's modulus) and ν (Poisson's ratio), or the thermal expansion coefficient α; $V_{\mathrm{Metal}}(x)$ and $V_{\mathrm{Ceramic}}(x)$ are the volume fractions of metal and ceramic, respectively, at the position x. The simplified material property form overlooks the interactions of the two material phases at the microscopic level, so it leads to an approximate solution. The more accurate material property variation form at the macroscopic level requires a better understanding of FGM microstructure and its deformation, which are the focus of this study. We will only obtain the elastic solution for the continuous model, and it is mainly for comparison with the solution obtained by the discrete model. Plastic deformation of the sandwich structure was studied using a continuous model in Giannakopoulos *et al.* [5] and Finot *et al.* [6].

The thermoelastic solution in this case may be obtained analytically [5]. Here, a finite element method is used for the purpose of examining its accuracy for FGMs. In the implementation, the FGM layer is divided into 30 micro-layers, as shown schematically in Fig. 2(a), and the material properties of each micro-layer are taken to be constants.

2.2. *The discrete micromechanics model*

We have developed a computational micromechanics model for FGMs using the crystal plasticity theory. Figure 2(b) shows the model geometry for a FGM consisting of the metallic and ceramic grains randomly distributed within it. The macroscopic material properties obtained by statistical processing of the random distribution of the metal and ceramic grains vary continuously along the thickness direction, and give their desired variation forms. Each of the metal grains has its own crystal orientation (also randomly distributed) which is shown by the angle ψ in Fig. 3, and its thermoplastic behavior is assumed to be governed by crystal plasticity theory. The ceramic grains are modeled using the standard linear elasticity theory.

The two-dimensional idealization shown in Fig. 3 was introduced by Harren *et al.* [12], Harren and Asaro [13] and McHugh *et al.* [14] for f.c.c. or b.c.c. polycrystals and their metal matrix composites. The three slip systems are arranged in an equilateral triangle, and the reference laboratory base vectors $\mathbf{X}_i$ are at an angle ψ with respect to reference crystal base vectors $\mathbf{a}_i$. The slip directions in this model geometry, $\mathbf{s}_1$, $\mathbf{s}_2$ and $\mathbf{s}_3$, represent the close-packed directions of an assemblage of close-packed circular cylinders. Since, in a two-dimensional model two independent slip systems can accommodate arbitrary increment of plastic strain, the three independent slip systems here resemble the redundancy exhibited by both f.c.c. and b.c.c. crystals. We note that using traditional metal plasticity theories (i.e. J_2 flow theory) would give us similar results for Ni (f.c.c.). If any low-symmetry crystals (say NiAl or TiAl) are involved, then crystal plasticity theory is necessary to account for the orientation dependent deformation behavior.

The single crystal constitutive theory, in its present form, was developed by Asaro and his coworkers [14–21]. The theory which will be briefly described below builds on the pioneering work by Taylor [22] and Hill and Rice [23].

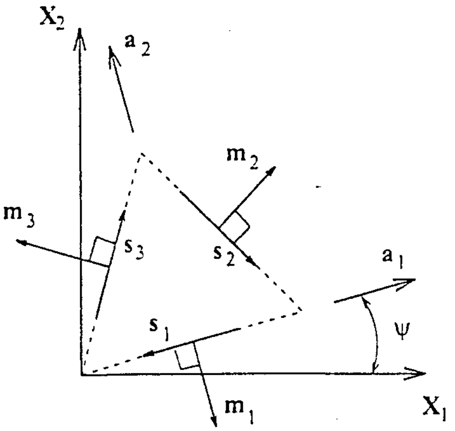

Fig. 3. Two-dimensional model single crystal slip geometry used for metal grains. The three slip systems are arranged in an equilateral triangle, and the reference laboratory base vectors $\mathbf{X}_i$ are at an angle ψ with respect to reference crystal base vectors $\mathbf{a}_i$.

The total deformation gradient is decomposed into plastic ($\mathbf{F}^p$), thermal ($\mathbf{F}^\theta$), and lattice ($\mathbf{F}^*$) parts, as shown in the insert of Fig. 2(b). If $\mathbf{u}$ is the displacement vector and $\mathbf{X}$ the material position vector with respect to the reference (undeformed) state, $\mathbf{F} = \mathbf{I} + \partial\mathbf{u}/\partial\mathbf{X}$ ($\mathbf{I}$ is the second-order identity tensor) and

$$\mathbf{F} = \mathbf{F}^* \cdot \mathbf{F}^\theta \cdot \mathbf{F}^p. \tag{2}$$

Plastic deformation occurs by the flow of material through the lattice, via simple shearing, across planes with unit normals $\mathbf{m}_\alpha$ and in directions $\mathbf{s}_\alpha$; here $\mathbf{m}_\alpha$ and $\mathbf{s}_\alpha$ represent a crystallographic slip plane normal and a slip direction, respectively, and α is an index that designates a slip system. If $\dot{\gamma}_\alpha$ is the slip rate on the α slip system, then the velocity gradients of this plastic shear flow can be written as

$$\dot{\mathbf{F}}^p \cdot \mathbf{F}^{p-1} = \sum_\alpha \dot{\gamma}_\alpha \mathbf{s}_\alpha \mathbf{m}_\alpha, \tag{3}$$

where the summation is over all active slip systems. The thermal parts of the velocity gradients are described as

$$\dot{\mathbf{F}}^\theta \cdot \mathbf{F}^{\theta-1} = \dot{\theta}\boldsymbol{\alpha}; \quad \boldsymbol{\alpha} = \sum_i \sum_j \alpha_{ij} \mathbf{a}_i \mathbf{a}_j, \tag{4}$$

where θ represents temperature and $\boldsymbol{\alpha}$ is a tensor whose components, α_{ij}, with respect to the time independent Cartesian base vectors, $\mathbf{a}_i$, are the thermal expansion coefficients. The base vectors are aligned with the crystal lattice in the reference configuration in some standard way, e.g. in cubic crystals. It is most convenient to align the $\mathbf{a}_i$ base vectors with the cube axes, in which case $\boldsymbol{\alpha}$ would be diagonal with all components equal.

In general, $\dot{\gamma}_\alpha$ will be a function of temperature, stress state and material state. As a specific example we have used expressions such as

$$\dot{\gamma}_\alpha = \dot{a}\,\mathrm{sgn}\{\tau_\alpha\}\left\{\left|\frac{\tau_\alpha}{g_\alpha}\right|\right\}^{1/n} \tag{5}$$

to represent strain rate sensitive power-law type behavior. In the expression, n is the material rate sensitivity parameter, τ_α is the resolved shear stress on the slip system α, and $g_\alpha > 0$ is its current strength.

The slip system hardness, g_α, is obtained by the path-dependent integration of the evolution equations of the form:

$$\dot{g}_\alpha = \sum_\beta h_{\alpha\beta}(\gamma_a)|\dot{\gamma}_\beta| + g_\alpha^\theta\dot{\theta}; \quad \gamma_a = \int_0^t \sum_\alpha |\dot{\gamma}_\alpha|\,\mathrm{d}t, \tag{6}$$

where γ_a is the accumulated sum of slips, $h_{\alpha\beta}$ is a matrix of hardening moduli and g_α^θ is the rate of change of slip system hardness with respect to temperature alone. The initial condition for this

Table 1. Elastic properties used for the computations

	E (GPa)	ν	α (K^{-1})
Al_2O_3	380	0.25	7.4×10^{-6}
Ni	214	0.35	15.4×10^{-6}

evolution is given by

$$g_\alpha(\gamma_a = 0, \theta) = g_0(\theta), \tag{7}$$

where θ is the temperature.

The detailed development of these constitutive relations can be found in McHugh *et al.* [14]. This constitutive theory has been implemented into finite element codes, using a rate tangent method introduced by Pierce *et al.* [18].

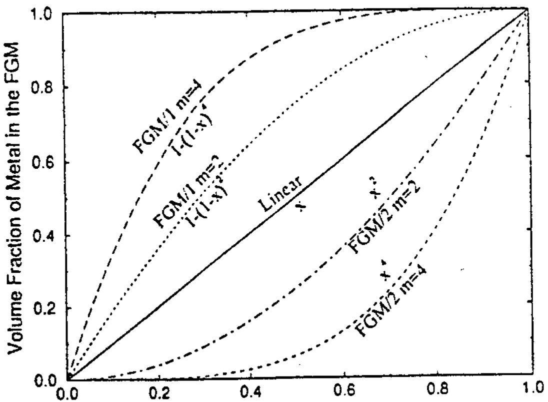

Fig. 4. Different gradient functions used in the residual stress analysis.

3. RESULTS

The geometry of the sandwich structure is specified in Fig. 2. To avoid the edge effects, the total length/width ratio ($L_0/(H + 2h)$) was chosen to be 5, while only the center part with length $L(L < 0.25L_0)$ was considered when performing residual stress analysis. Two sets of FGM interlayer thickness, i.e. $H/(H + 2h) = 40$ and 70 vol%, were used.

To make this complicated boundary value problem manageable computationally, a relatively coarse mesh (i.e. four triangular elements per grain) is used in this study and simple square grains are employed. Doing so, as Taylor [22, 24] and many others [25–27] did successfully in modeling polycrystalline materials, effectively treats the deformation within each individual grain as uniform. The finite element model, however, takes the interactions between all constituent grains into consideration, which is not achievable using Taylor or Sachs type models. In studying the interactions at the grain size level, this model design is at least a first-order approximation. Also, in keeping all the microstructural "building blocks" (i.e. ceramic and metal grains in the discrete model) exactly the same, the relative importance of material gradient and FGM volume percentage can be identified.

The specific FGM system is the Al_2O_3–Ni system. In this study, the major focus is on the relative importance of the discrete and random microstructure vs FGM volume fraction and gradient functional form. With that in mind, and noting that all the case studies shown later were performed under a relatively small (300°C) temperature variation, for simplicity the elastic properties were taken to be constants. The material properties used for the computations are listed in Tables 1 and 2. A two-dimensional plane strain deformation condition was imposed. The thermal loading was induced by cooling the structure by 300°C. The temperature was assumed to be uniform within the three-layer structure, and the sandwich structure was set to be stress free at the beginning temperature. For the metal grains, linear interpolation was used to obtain the temperature-dependent critical resolved shear stresses $g_0(\theta)$ in equation (7) between the several temperatures shown in Table 2. The shear strain hardening h in equation (6) was taken to be 77.4 MPa, which was converted from the data in Ref. [28] using a Taylor factor of 3.06 for f.c.c. polycrystals with the linear hardening assumption. A low material rate sensitivity parameter is given as $n = 0.005$ in equation (5).

We write V_{FGM} as the volume fraction of Ni within the FGM layer, and x as the relative distance from the Al_2O_3–FGM interface (i.e. $x = 0$ stands for the Al_2O_3–FGM interface and $x = 1$ stands for the FGM–Ni interface). As shown in Fig. 4, three functional forms were used in the computations:

$$\text{Linear:}\quad V_{FGM}(x) = x, \tag{8a}$$

$$\text{FGM/1:}\quad V_{FGM}(x) = 1 - (1 - x)^m, \quad m = 2, 4, \tag{8b}$$

$$\text{FGM/2:}\quad V_{FGM}(x) = x^m, \quad m = 2, 4. \tag{8c}$$

When $m = 1$, both FGM/1 and FGM/2 reduce to the linear case of equation (8a), and when $m \geqslant 2$ functions in the FGM/1 class have zero slope at the FGM–Ni interface ($x = 1$), whereas the functions in the class FGM/2 have zero slope at the Al_2O_3–FGM interface ($x = 0$).

Table 2. Plastic properties of Ni grains used in the computations

T (°C)	20	127	227	327	427	527	627	727	827
$\sigma_y{}^a$ (MPa)	148	153	140	138	115	100	69	59	45
$\tau_{CRSS}{}^b$ (MPa)	48.4	50.0	45.8	45.1	37.6	32.7	22.5	19.3	14.7

[a] Data from Suresh *et al.* [28].

[b] Calculated from σ_y with a Taylor factor of 3.06.

3.1. The continuous model—macroscopic stresses vs material gradients and FGM volume percentages

For this problem, the only non-zero stress component is the in-plane normal stress along the X_2 direction. Figures 5(a) and (b) show the results of the in-plane normal stress distribution along the X_1 direction for the 40 and 70 vol% FGM, respectively. Due to the presence of the FGM layer, the stresses are continuous, and have continuous derivatives wherever the material property variation function in equations (8) is. It is noteworthy that although the existence of the FGM layer in general decreases the stress at one or both of the interfaces, for power index $m \leqslant 2$ in equations (8), there is an extremum in the FGM layer, and this extremum in some cases has a magnitude close to that of the normal stress at the interface in the base-line case, i.e. a sharp ceramic–metal interface without the FGM layer [29]. Comparing Fig. 5(b) with Fig. 5(a), it is found that, in general, increasing the relative FGM volume percentage decreases the stress at one or both of the interfaces. These results are similar to those found in Giannakopoulos *et al.* [5].

Next, we will explore how the local stress concentrations interact with material gradient as well as the FGM volume percentage. The averaged physical meaning of the continuous solution will be clearer when we present the discrete solution below and compare the two solutions.

3.2. The discrete model—local stress concentrations and macroscopic stresses

In this section, the discrete micromechanics model is used and only elastic deformation is considered. Plasticity effects will be studied in the next section.

Figure 6 shows contour plots of (a) σ_{22}, and (b) averaged in-plane principal stress ($p = (\sigma_{11} + \sigma_{22})/2$) developed in the 40 vol% FGM with linear gradient. It is clearly seen that the local stress concentration is quite high and the stress field is very inhomogeneous, i.e. the stress variations among many of the adjacent grains are significant. The σ_{11} was also found to be inhomogeneous. Due to the thermal mismatch between ceramic grains and metal grains, most metal grains experience large tensile stresses; and this is especially true for metal grains near the ceramic–FGM interface and those in the middle region of the FGM layer.

Additional computations were performed using different gradient functions. Figure 7 shows contour plots of averaged in-lane principal stress ($p = (\sigma_{11} + \sigma_{22})/2$) developed in the 40 vol% FGM with (a) gradient function $V_{\mathrm{FGM}} = 1 - (1 - x)^2$ (FGM/1 $m = 2$), and (b) gradient function $V_{\mathrm{FGM}} = x^2$ (FGM/2 $m = 2$). The distribution of stresses is quite different with different gradient functions, as can be seen clearly from Figs 6(b), 7(a) and 7(b). Detailed examination of Figs 6 and 7 tells us that, in almost every local region (say take 5 × 5 grains as the region size) where the ceramic grains are more than 40 vol%, there are always some metal grains experiencing significant tensile stresses for all three cases. The results for the 70 vol% FGM were similar to those for the 40 vol% FGM.

For such discrete and random microstructures, more physical insights can be gained via the statistical analyses of the stress distribution. Figure 8(a) shows the distribution profiles of $p = (\sigma_{11} + \sigma_{22})/2$ developed in the FGM layer (40 vol% FGM) with three different gradient functions; Fig. 8(b) shows the distribution profiles of p developed in the FGM layer (linear gradient) of a 40 and a 70 vol% FGM, respectively. The three distribution profiles in Fig. 8(a) are distinctively different: (i) the distribution peak between 50 and 200 MPa (mostly in metal grains) drops as the total metal composition in the FGM layer decreases; and (ii) the distribution peak between −50 and −250 MPa (mostly developed in ceramic grains) increases as the total ceramic composition in the FGM layer increases. The FGM volume percentage also has large influences on the distribution profile of p, see Fig. 8(b): the distribution peak for tensile stresses shifted from around 110 MPa (40 vol% FGM) to about 50 MPa (70 vol% FGM); and the distribution peak for compressive stresses

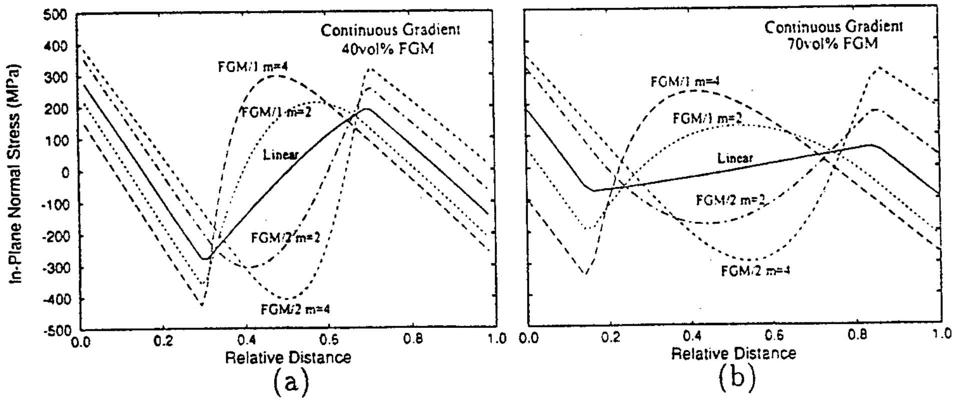

Fig. 5. In-plane normal stress distributions along the X_1 direction using the continuous model with (a) 40 and (b) 70 vol% FGM, respectively.

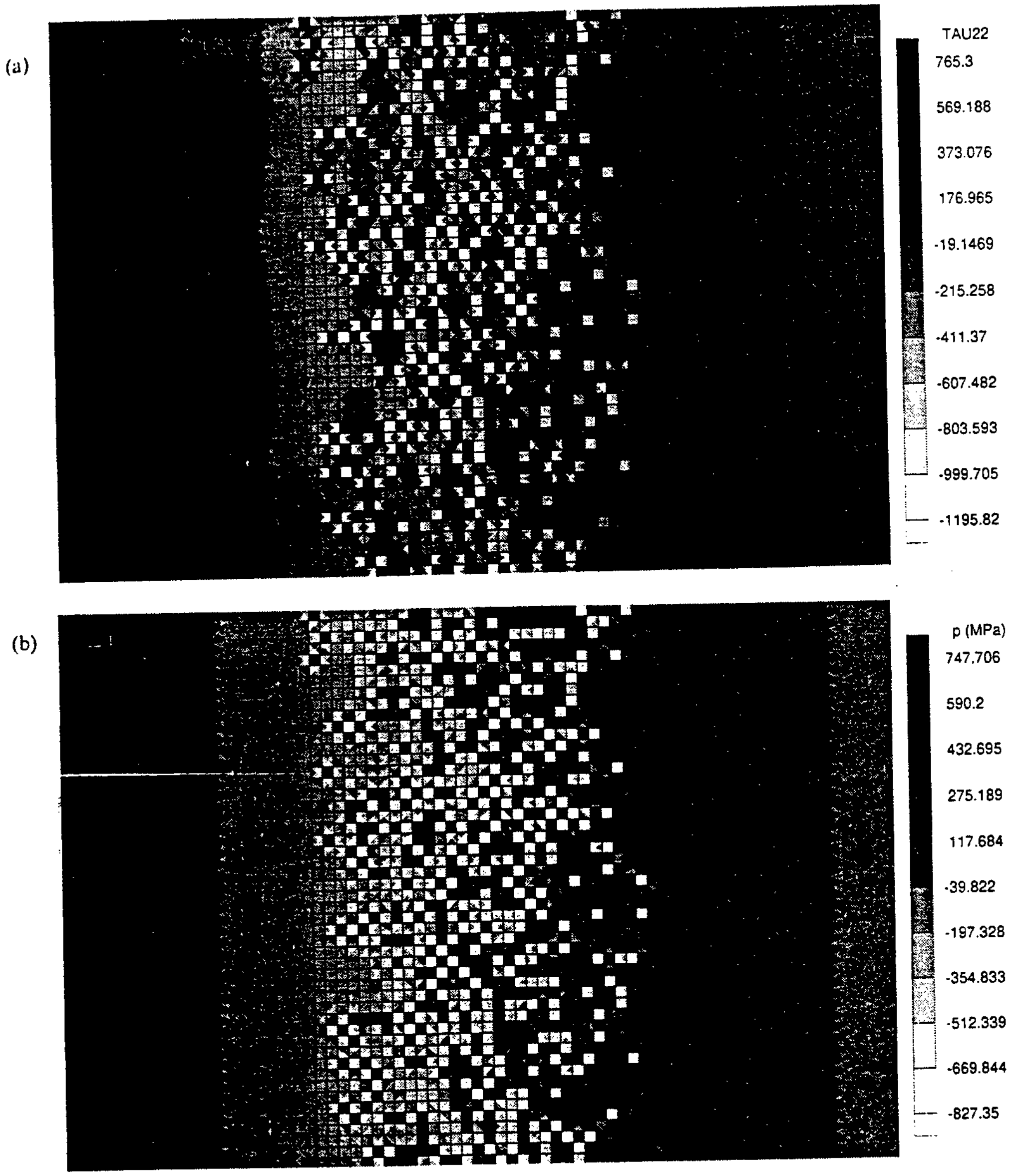

Fig. 6. Contour plots of (a) σ_{22}, and (b) averaged in-plane principal stress ($p = (\sigma_{11} + \sigma_{22})/2$) developed within the linear gradient, 40 vol% FGM. Only elastic deformation is considered here.

shifted from around -150 MPa (40 vol% FGM) to about -50 MPa (70 vol% FGM). However, the distribution profile for high stresses, i.e. for $p \leqslant 500$ MPa or $p \geqslant -500$ MPa, are found to be insensitive to material gradient and FGM volume percentage.

Finally, for the purpose of comparison, we averaged the stresses over each column of elements to get the mean stress along the vertical direction. Figure 9 shows the macroscopically averaged in-plane normal stress developed within the discrete microstructures (shown by separated symbols) as compared to the curves obtained using the continuous model (shown by continuous lines). It is interesting to see that, although there are a lot of local stress concentrations, the two types of modeling approach given practically the same averaged (or macroscopic) stresses. In an averaged sense, only small variations can be found in Fig. 9 for the discrete microstructure model due to the local randomness and discreteness. This shows that the macroscopic stresses are those based on a scale much larger than the grain size and obtained without considering certain details, such as local stress concentrations, at a smaller scale.

3.3. *The discrete model—influence of plastic deformation*

In this section, we explore the effects of plastic deformation within the metal grains in the discrete microstructure. Besides the concentrated stresses, large, locally concentrated plastic strain accum lation during repeated thermal cycling may also initiate failure.

Figure 10 shows the contour plots of (a) averaged in-plane principal stress ($p = (\sigma_{11} + \sigma_{22})/2$), and (b) accumulated sum of slips (γ_a) developed in the linear gradient, 40 vol% FGM. The temperature drop was from 700 to 400°C, and the plasticity parameters were taken to be as listed in Table 2. Similar to the thermoelastic case, the stress distribution is again inhomogeneous, with many metal grains experiencing high tensile stresses and many ceramic grains experiencing high compressive stresses. If we compare Fig. 10(a) with Fig. 6(b) (elasticity only), the stress concentration in the ceramic grains is significantly reduced in the region where metal content is greater than 70 vol%, due to plastic relaxation. With only a 300°C temperature drop, Fig. 10(b) shows that: (i) there are plastic strain accumulations in many of the metal grains, and (ii) certain sites have relatively high strain accumulations, about 1.5%. The high strain accumulation sites seem to appear in the regions where metal content is between 50 and 75 vol%.

Figure 11 shows the distribution profiles of p $(=(\sigma_{11} + \sigma_{22})/2)$ developed within the FGM layer (linear gradient, 40 vol% FGM), for both the elastic and the elastoplastic case. The plastic relaxation effect is very clear here in this case, where stresses are in general shifting to lower magnitudes with plasticity. The distribution profile for high tensile stresses with $p \geqslant 700$ MPa, however, has reduced only slightly with plastic relaxation. Similar to the thermoelastic case, the stress distribution profile for

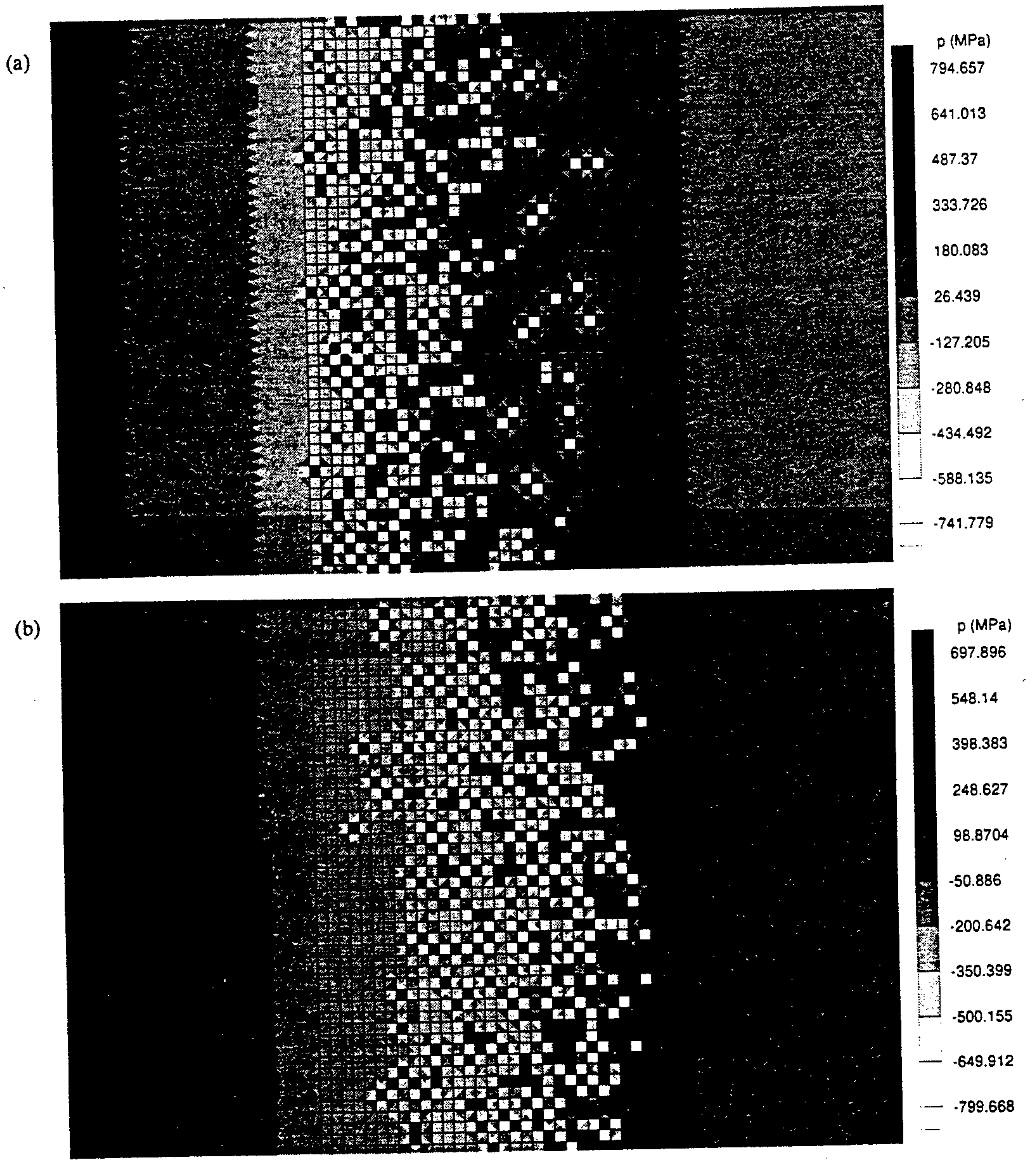

Fig. 7. Contour plots of averaged in-plane principal stress ($p = (\sigma_{11} + \sigma_{22})/2$) developed in the 40 vol% FGM with (a) gradient function $V_{\mathrm{FGM}} = 1 - (1 - x)^2$ (FGM/1 $m = 2$), and (b) gradient function $V_{\mathrm{FGM}} = x^2$ (FGM/2 $m = 2$). Only elastic deformation is considered here.

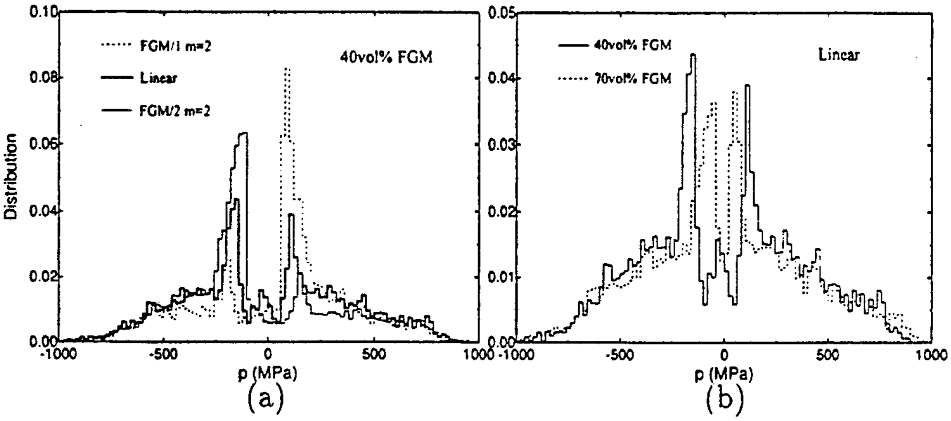

Fig. 8. (a) Averaged in-plane principal stress ($p = (\sigma_{11} + \sigma_{22})/2$) distribution profiles developed within the FGM layer (40 vol% FGM) with three different gradient functions; and (b) distribution profiles of p developed in the FGM layer (linear gradient) of a 40 and a 70 vol% FGM, respectively.

high tensile stress regions is insensitive to material gradient and FGM volume percentage. On the other hand, the distribution profile for high compressive stresses with $p \leqslant -250$ MPa (mostly in ceramic grains) drops significantly. This suggest that, when ceramic grains are subject to tensile stresses *if temperature increases*, the plastic relaxation effects may reduce their tensile stress concentrations.

We average the stresses over each column of elements for the plastic solution to obtain the averaged in-plane normal stress. Figure 12 plots the macroscopically averaged stress for both the elastic and the elastoplastic case. Comparing Fig. 12 with Fig. 10(b), it is found that the metal rich section and part of the pure metal region are under general macroscopic yielding, which sets the maximum magnitude of the macroscopic stresses for the plastic case.

3.4. The statistical analysis of residual stress concentrations—averaged peak stress

Since the stress distribution profiles of p for the high stress area shown in Figs 8 and 11 are small, to get more reliable statistical results we employ 6 vol% APSP to treat the data in these figures. The 6 vol% APSP (averaged peak stress of p) is the stress p averaged over the 6 vol% microstructure of the FGM layer which has the highest tensile stresses (p). Similarly, we can obtain 3 vol% APSP, 9 vol% APSP etc. Figure 13 shows the 6 vol% APSP (averaged peak stress of p) for different material gradients and different FGM volume percentages, and for both the elastic solution (marked with El) and the elastoplastic solution (marked with Pl). From Fig. 13, the distribution profile for high tensile stresses is again found to be insensitive to material gradient and FGM volume percentage, and the plastic relaxation effect is relatively small for the high stress regime. Similar conclusions can be drawn from the 3 vol% APSP (averaged peak stress of p).

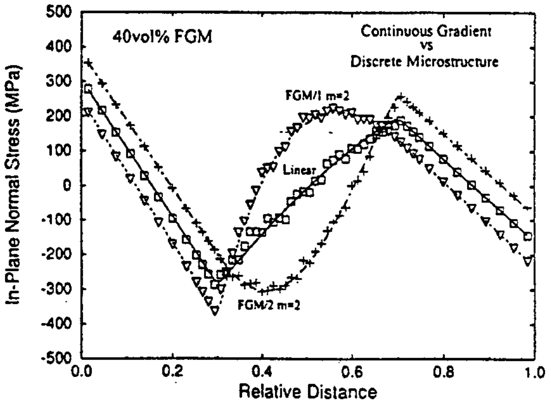

Fig. 9. Macroscopically averaged in-plane normal stress developed within the discrete microstructures (shown by separated symbols) as compared to the curves obtained using the continuous model (shown by continuous lines).

The above statistical results are interpreted by the following observations. As mentioned before, high tensile stresses always occur in those metal grains surrounded by many ceramic grains. Comparing those stresses in Figs 5 and 9, the stress concentrations in these metal grains are found to be an order of magnitude higher than the macroscopic stresses in the FGM layer. Considering the large number of stiff ceramics around each of those metal grains, the high local stresses are believed to be insensitive to the macroscopic physical parameters. The effect of material gradient and FGM percentage on the macroscopic stresses is mainly due to the change of the distribution profiles in the middle parts of Figs 8 and 11, which have lower magnitude of stresses.

For the small plastic relaxation for local stress concentrations shown in Fig. 13, this can also be related to the fact that peak tensile stresses always occur in metal grains where a lot of ceramic grains are surrounded. The general stress state induced in such metal grains is mostly all around tension, i.e. $\sigma_1 \approx \sigma_2$ where σ_1 and σ_2 are the two in-plane principal stresses. With $\sigma_1 \approx \sigma_2$, the maximum shear stress $\tau_{\max} = (\sigma_1 - \sigma_2)/2$ is therefore small. No matter how

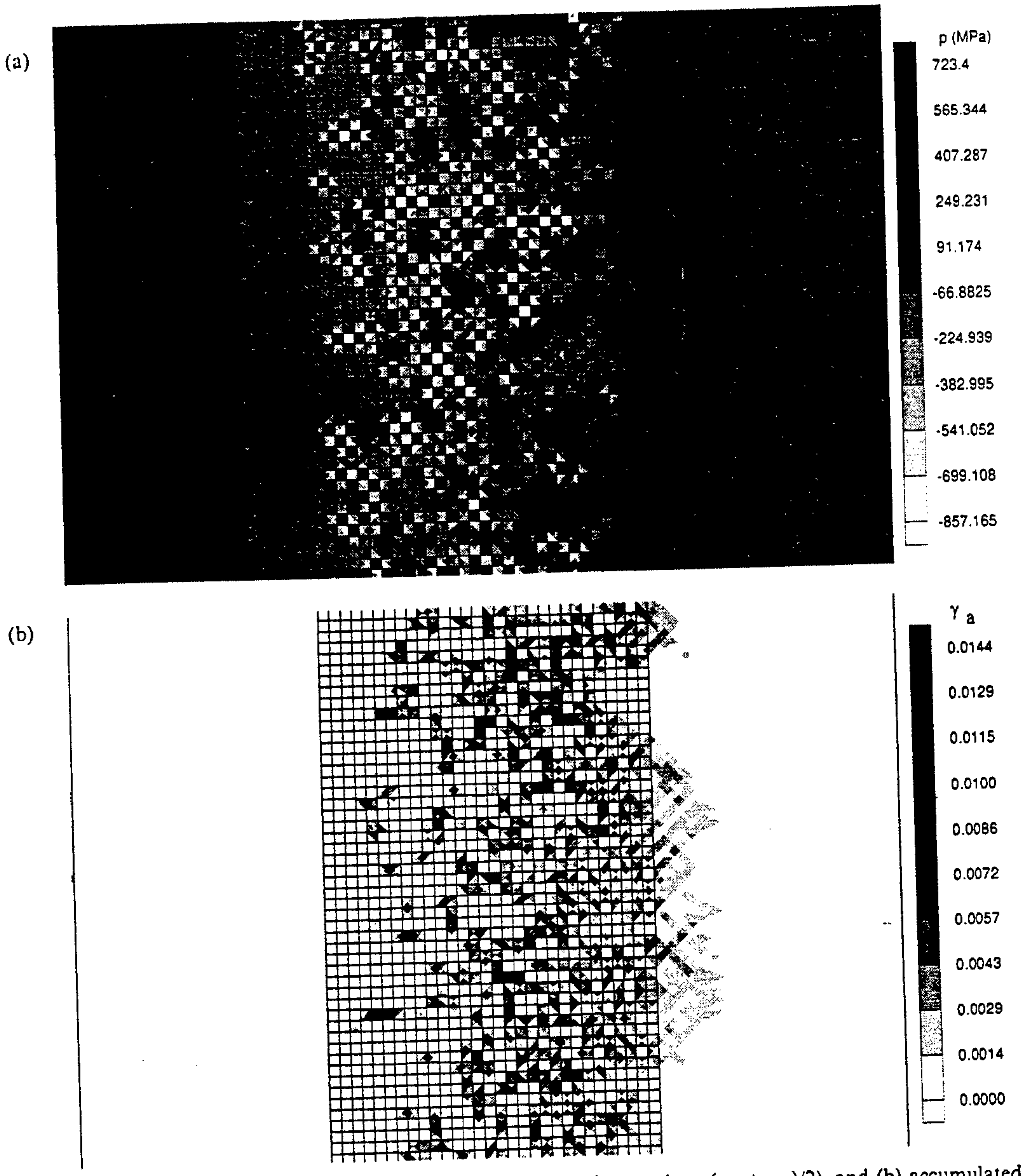

Fig. 10. Contour plots of (a) averaged in-plane principal stress ($p = (\sigma_{11} + \sigma_{22})/2$), and (b) accumulated sum of slips (γ_a) developed in the linear gradient, 40 vol% FGM. Plastic deformation is considered here.

low the yield strength is in the metal grains, small shear stresses can hardly produce any plastic deformation, and therefore are not helpful in relaxing this kind of stress state.

4. DISCUSSION

A physically based micromechanical model is developed to study residual stress distributions and concentrations in the FGM sandwiched between two dissimilar materials during thermal loadings. The results obtained reveal detailed information of microstructural behavior at the grain size level, and thus provide some insights for optimizing FGMs and the control of their failures.

It is stressed that the scale level we are concerned with in this study is at the grain size level and upwards. Using the relatively coarse mesh and square "building blocks" is a first-order approximation to the reality, and not intended for subgrain level microscopic features. For example, a very refined mesh will show very high stress concentrations (in fact singularities) at the inter-phase corners. Due to the relative small $E_{Al_2O_3}/E_{Ni}$ ratio (1.77), the singularity is a fairly weak one, which means high stress regions will only occupy a very small volume fraction. It is shown that in the case of two elastic bonded quarter planes, the order of the singularity is about 0.05 ($1/r^\alpha$, $\alpha = 0.05$) for such an elastic difference, see Bogy [30]. This kind of singularity is thus expected to have little (i.e. second order) effect on the averaged grain level stress. However, if 5–6 vol% of the FGM grains have some averaged tensile stresses higher than

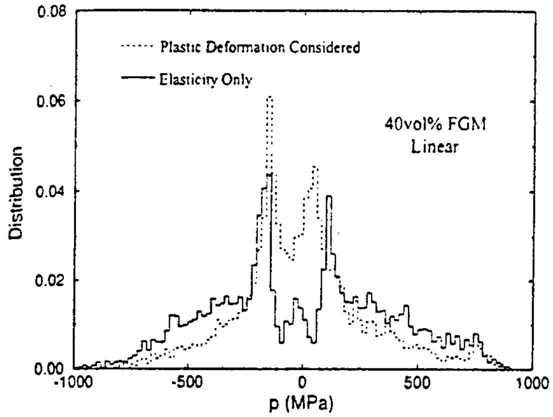

Fig. 11. Averaged in-plane principal stress ($p = (\sigma_{11} + \sigma_{22})/2$). distribution profiles developed within the FGM layer (40 vol% FGM, linear gradient) for both the elastic and the elastoplastic case.

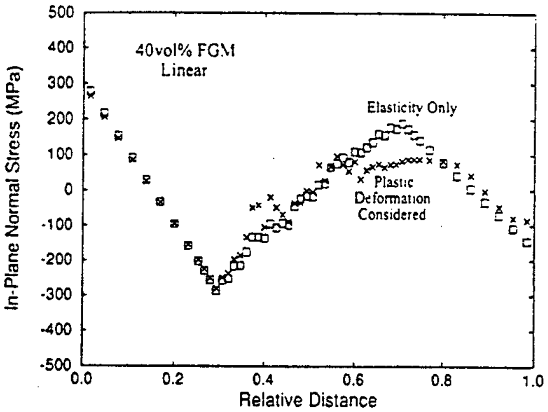

Fig. 12. Macroscopically averaged in-plane normal stress developed within the discrete microstructure (40 vol% FGM, linear gradient). for both the elastic and the elastoplastic case.

700–800 MPa, only higher local stresses can be expected near those subgrain level microscopic features.

The grain level microscopic stress concentrations are found to be quite high, of the order of 800 MPa, with only a 300°C temperature drop; whereas the macroscopic stresses are much lower than the microscopic stresses. This suggests that, if high tensile stress concentration at the grain size level is the failure initiation mode at this size scale, there are always micro-fractures at the grain size scale during thermal loading. Since the stress distribution profile for the high stress region is quite insensitive to material gradient and FGM volume percentage as shown in Section 3, the above conclusion is independent of those two macroscopic parameters. On the other hand, the high stress region in the stress distribution profile is relatively small (about 5–6 vol% with stress p above 700 MPa). Whether the small-scale micro-fractures at the grain size level will develop into large-scale fractures to cause the fatal damage of the whole structure depends on other factors whose effects require further investigation, such as stress redistribution after small-scale failure initiation, loading history and the grain boundary adhesion between the adjacent grains. The present computational micromechanics model can be extended to account for these influences.

For optimizing the microstructure, since the dense structure results in high local stress concentrations, our results suggest that for achieving higher toughness the porous microstructure should be considered; and this is consistent with the experimental observation by Sohda *et al.* [11] on the Si–C FGM. Their experiments showed that the porous microstructure has a much better resistance against

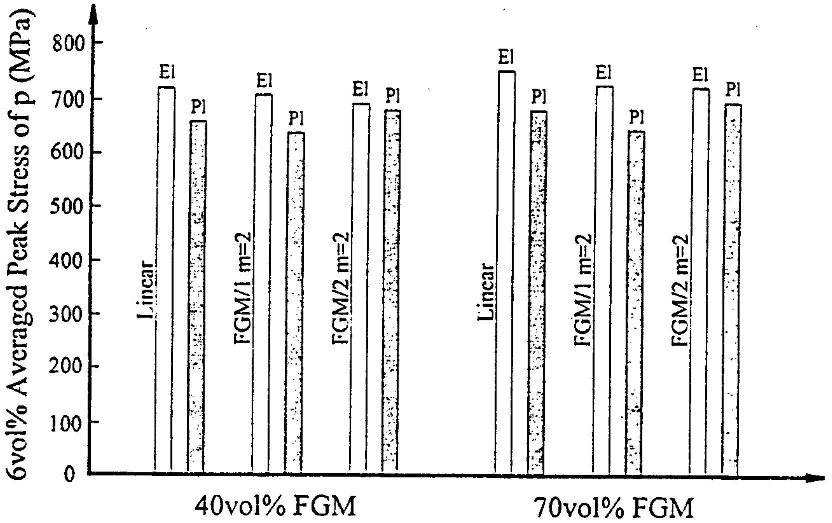

Fig. 13. The 6 vol% averaged peak stress of p (APSP) developed in FGM microstructures with different material gradients and different FGM volume percentages for both the elastic solution (marked with "El" on top) and the elastoplastic solution (marked with "Pl" on top).

cracking than the dense microstructure. Also, in a recent review paper, Koizumi and Niino [31] listed micropore as one of the most important material constituencies in FGM microstructures. Regarding the grain size, the extent of micro-fracturing exhibits large sensitivity to the grain size in ceramic polycrystals subject to thermal loading, being more severe in coarse grained ceramics [32, 33]; therefore, a fine grain sized microstructure is suggested to improve the FGM's resistance against cracking and delamination.

Other microstructural factors, such as grain shape, grain size and third-phase particle, are beyond the scope of the present work, and are the considerations of later studies. The results shown here have clearly demonstrated the need to consider microstructural details in modeling FGMs for determining their mechanical behavior: due to the microstructural discreteness, local residual stress concentrations play a very important role in failure initiation.

Acknowledgements—This research was supported by the Office of Naval Research under contract number N00014-93-1-1164. Partial support by the U.S. National Science Foundation under contract number DMR91-10930 is also acknowledged. Computations were performed at the National Science Foundation supported San Diego Supercomputer Center. The authors are glad to acknowledge helpful discussions with Dr Ning Shi at Los Alamos National Laboratory.

REFERENCES

1. Niino, M., Hirai, T. and Watanabe, R., *J. Jpn. Soc. Comp. Mater.*, 1987, **13**, 257.
2. Yamanouchi, M., Koizumi, M., Hirai, T. and Shiota, I. ed., *Proc. 1st Int. Symp. Functionally Gradient Materials*, FGM Forum, Tokyo, Japan, 1990.
3. Holt, J. B., Koizumi, M., Hirai, T. and Munir, Z. A. ed., *Functionally Gradient Materials, Proc. 2nd Int. Symp. Functionally Gradient Materials*, San Francisco, CA, 1992.
4. Pindera, M. J., Arnold, S. M., Aboudi, J. and Hui, D. ed., *Compos. Engng*, 1994, **4**, 1.
5. Giannakopoulos, A. E., Suresh, S., Finot, M. and Olsson, M., *Acta metall.*, 1995, **43**, 1335.
6. Finot, M., Suresh, S., Bull, C. and Sampath, S., *Materi. Sci. Engng A*, 1996, **205**, 59.
7. Aboudi, J., Pindera, M. J. and Arnold, S. M., *Int. J. Solids Struct.*, 1994, **31**, 1393.
8. Aboudi, J., Pindera, M. J. and Arnold, S. M., *Int. J. Solids Struct.*, 1995, **32**, 1675.
9. Noda, N. and Jin, Z., *Int. J. Solids Struct.*, 1993, **30**, 1039.
10. Gu, P. and Asaro, R. J., *Int. J. Solids Struct.*, 1997, **34**, 1.
11. Sohda, Y., Kude, Y., Uemura, S., Saitoh, T., Wakamatsu, Y. and Niino, M., in *Functionally Gradient Materials*, ed. J. B. Holt, M. Koizumi, T. Hirai and Z. A. Munir, San Francisco, CA, November, 1992, p. 125.
12. Harren, S. V., Dève, H. E. and Asaro, R. J., *Acta metall.*, 1988, **36**, 2435.
13. Harren, S. V. and Asaro, R. J. *J. Mech. Phys. Solids*, 1989, **37**, 191.
14. McHugh, P. E., Asaro, R. J. and Shih, C. F., *Acta metall.*, 1993, **41**, 1461.
15. Asaro, R. J. and Rice, J. R., *J. Mech. Phys. Solids*, 1977, **25**, 309.
16. Asaro, R. J., *Acta metall.*, 1979, **27**, 445.
17. Peirce, D., Asaro, R. J. and Needleman, A., *Acta metall.*, 1982, **30**, 1087.
18. Peirce, D., Asaro, R. J. and Needleman, A., *Acta metall.*, 1983, **31**, 1951.
19. Dao, M. and Asaro, R. J., *Mater. Sci. Engng A*, 1993, **170**, 143.
20. Dao, M. and Asaro, R. J., *Mech. Mater.*, 1996, **23**, 71.
21. Dao, M. and Asaro, R. J., *Mech. Mater.*, 1996, **23**, 103.
22. Taylor, G. I., *J. Inst. Metals*, 1938, **62**, 307.
23. Hill, R. and Rice, J. R., *J. Mech. Phys. Solids*, 1972, **20**, 401.
24. Taylor, G. I., in *Stephen Timoshenko 60th Anniversary Volume*, ed. J. M. Lessels. Macmillan, New York, 1938, pp. 218.
25. Asaro, R. J. and Needleman, A., *Acta metall.*, 1985, **33**, 923.
26. Molinari, A., Canova, G. R. and Ahzi, S., *Acta metall.*, 1987, **35**, 2983.
27. Kalidindi, S. R., Bronkhorst, C. A. and Anand, L., *J. Mech. Phys. Solids*, 1992, 40, 537.
28. Suresh, S., Giannakopoulos, A. E. and Olsson, M., *J. Mech. Phys. Solids*, 1994, **42**, 979.
29. Maewal, A. and Asaro, R. J., Technical Report for ONR Contract No. N00014-94-C-0113, Trans-Science Corporation, 1995.
30. Bogy, D., *J. appl. Mech.*, 1968, **35**, 460.
31. Koizumi, M. and Niino, M., *MRS Bull.*, 1995, **20**(1), 19.
32. Rice, R. W. and Pohanka, R. C., *J. Am. Ceram. Soc.*, 1979, **62**, 559.
33. Ortiz, M. and Molinari, A., *J. Mech. Phys. Solids*, 1988, **36**, 385.

A Simplified Method for Calculating the Crack-Tip Field of Functionally Graded Materials Using the Domain Integral

P. Gu[1]

M. Dao
Assoc. Mem. ASME

R. J. Asaro

Division of Structural Engineering,
University of California at San Diego,
La Jolla, CA 92093-0085

A finite element based method is proposed for calculating stress intensity factors of functionally graded materials (FGMs). We show that the standard domain integral is sufficiently accurate when applied to FGMs; the nonhomogeneous term in the domain integral for nonhomogeneous materials is very small compared to the first term (the standard domain integral). In order to obtain it, the domain integral is evaluated around the crack tip using sufficiently fine mesh. We have estimated the error in neglecting the second term in terms of the radius of the domain for the domain integration, the material properties and their gradients. The advantage of the proposed method is that, besides its accuracy, it does not require the input of material gradients, derivatives of material properties; and existing finite element codes can be used for FGMs without much additional work. The numerical examples show that it is accurate and efficient. Also, a discussion on the fracture of the FGM interlayer structure is given.

1 Introduction

The mechanics of functionally graded materials (FGM), including crack problems, have been intensively studied recently. It has been shown that for FGM crack problems the crack tip has a regular square-root singularity, the stress and displacement near-tip fields are of the same forms as those for homogeneous materials (see Delale and Erdogan, 1983, 1988; Gu and Asaro, 1997a, b). So the influence of material gradients at the near tip manifests itself through the stress intensity factors. In other words, the stress intensity factors uniquely characterize the near-tip field. Knowing the structure of the crack-tip field, it is important to accurately calculate the stress intensity factors and determine the effect of material gradients on them for different geometries and loadings, including those often-used specimens. Finite element analysis which can handle difficult material behaviors and geometries as well as various loadings provides useful and the most often-used way to solve mechanical and thermal problems including those involving FGMs. In this paper, we present a simple and sufficiently accurate finite element method for calculating the crack-tip field for FGMs, which can be easily incorporated into existing finite element codes and commercial software packages without much additional work.

The often-used method to calculate the crack-tip field, stress intensity factors (elastic case), and energy release rate (elastic or plastic case), involves evaluating the J-integral (Rice, 1968) using the solved stress and deformation fields around crack tip. For homogeneous materials, this has been an efficient way since the path independence of the J-integral allows us to perform the calculation along a path not too close to the tip so that the inaccuracy of field variables at the tip region due to the singularity can be avoided. Later, the domain integral method has been developed to perform the calculation of the J-integral (Li, Shih and Needleman, 1985; Shih, Moran and Nakamura, 1986; Moran and Shih, 1987). The domain integral method has been shown to be more efficient and more accurate than direct calculation of the J-integral, since the domain integration comes more naturally than the line integration of the two-dimensional space and the surface integration of the three dimensional space in finite element analysis. Works along similar line as the domain integral can be found in the early papers by Parks (1974, 1977), Hellen (1975) and deLorenzi (1982), whose virtual crack extension method is the special case of the domain integral. The domain integral method has been implemented in numerous programs to solve crack mechanics, including the well-known commercial package ABAQUS. In this paper, we use the domain integral methodology to treat the FGM case. In the non-homogeneous case, there is an additional term besides the regular one due to the variation of material properties. In our analysis of two-dimensional elastic crack problems of nonhomogeneous materials, to capture the singularity and material property variation, the mesh is designed such that the smallest elements at the crack tip are very small, about 10^{-5} times a characteristic length, which is usually the crack length, and even much smaller for inelastic problems. The material variation is achieved by using corresponding material properties at Gauss integration points (different Gauss points have different properties). For such mesh design, to perform the domain integration, the domains can be chosen as the circular regions formed by the first few rings of elements. In such a situation, we show that the second term in the domain integral for nonhomogeneity is very small compared to the first term, the standard domain integral, and may be neglected. Therefore the domain integral can be calculated numerically in the same way as that for homogeneous materials, using the standard domain integral. From the numerical point of view, this allows us to apply existing finite element programs for homogeneous materials to nonhomogeneous materials, avoiding the additional programming work.

The current study is focused on elastic two-dimensional and three-dimensional problems. The method may also be extended

---

[1] MARC Analysis Research Corporation, 4330 La Jolla Village Drive, Suite 320, San Diego, CA 92122.

Contributed by the Applied Mechanics Division of THE AMERICAN SOCIETY OF MECHANICAL ENGINEERS for publication in the ASME JOURNAL OF APPLIED MECHANICS.

Discussion on the paper should be addressed to the Technical Editor, Professor Lewis T. Wheeler, Department of Mechanical Engineering, University of Houston, Houston, TX 77204-4792, and will be accepted until four months after final publication of the paper itself in the ASME JOURNAL OF APPLIED MECHANICS.

Manuscript received by the ASME Applied Mechanics Division, Mar. 9, 1998; final revision, July 14, 1998. Associate Technical Editor: M.-J. Pindera.

Copyright © 1999 by ASME

to the nonlinear material behavior. The numerical examples given include a sandwiched structure with a FGM interlayer, which illustrates the advantage of using FGM to reduce material mismatch between the upper and lower layers. For such structures, cracks may form at one side and propagate to the other side through the FGM interlayer when the microscopic defects and external loading are favorable. The crack in the sandwiched structure solved in this paper is along the layers' thickness direction with the crack tip inside the FGM, and the loading includes remote bending, three-point bending, and four-point bending. This kind of configuration may also be good for fracture testing of FGMs since the FGMs are usually very thin so that mechanical testing may be handled when bonding them to two bulk materials. In general, the solutions to the three-point bending and four-point bending specimens depend on several parameters, including geometry, loading, and material variation. We write them in a compact form such that the functionality of each parameter may be clearly understood. These examples show a way to systemically present the solutions so that they can be documented and are easy to use in practice.

The paper consists of three sections. Besides this Introduction, Section 2 is the discussion of the domain integral method in which we estimate the second term due to nonhomogeneity and show that based on the analysis, the term can be neglected. Section 3 contains numerical examples.

2 Numerical Method

The crack-tip stress field in a FGM has a regular singularity (see Delale and Erdogan, 1983, 1988; Gu and Asaro, 1997a, b) and the singular term for plane problems is given by

$$\sigma_{ij} = \frac{K_I}{\sqrt{2\pi r}}\,\sigma^I_{ij}(\theta) + \frac{K_{II}}{\sqrt{2\pi r}}\,\sigma^{II}_{ij}(\theta) \tag{1}$$

where the angular functions σ^I_{ij} and σ^{II}_{ij} are independent of material properties and their variations and are the same as those for homogeneous materials. The displacement singular term is given by

$$u_i = \frac{K_I}{2\mu_0}\sqrt{\frac{r}{2\pi}}\,u^I_i(\theta) + \frac{K_{II}}{2\mu_0}\sqrt{\frac{r}{2\pi}}\,u^{II}_i(\theta). \tag{2}$$

Here, μ_0 is the shear modulus at the crack tip. The angular functions u^I_i and u^{II}_i are also independent of material gradients, and are the same as those for homogeneous materials. Material gradients only affect the near-tip fields through the mode I and mode II stress intensity factors, K_I and K_{II}. The energy release rate is defined as

$$G = -\frac{\partial \Pi}{\partial a} \tag{3}$$

which is related to the near-tip field by

$$G = \frac{K_I^2}{E_0} + \frac{K_{II}^2}{E_0} \tag{4}$$

where E_0 is Young's modulus at the crack tip. The energy release rate can be represented by the following line integral:

$$J = \lim_{\Gamma\to 0}\int_\Gamma (W\delta_{1i} - \sigma_{ij}u_{j,1})n_i\,dC \tag{5}$$

where W is the strain energy density and n_i is the outward normal of the path Γ, which starts from a point on the lower crack face and ends at another point on the upper crack face. For the homogeneous case, the integral under the limit is divergence free; therefore, it is path independent and the limit is not needed. In this case, the J in (5) is Rice's J-integral (Rice, 1968). For nonhomogeneous materials, path independence occurs when the crack is perpendicular to the material property variation direction, since in this case the integral is still divergence free.

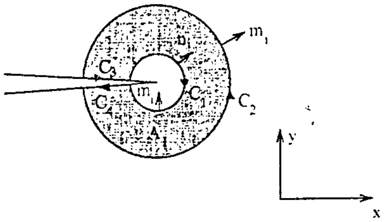

Fig. 1 A simply connected domain A_I enclosed by the contour C ($C = C_1 + C_2 + C_3 + C_4$) near crack tip. The domain is where the domain integral is evaluated.

There are usually several ways to calculate stress intensity factors after the stress and displacement fields are obtained. In the stress matching and displacement matching, the stress intensity factors are obtained by extrapolating from the stresses or displacements ahead of the crack tip using (1) or (2). For example, K_I is obtained by substituting the obtained normal stress ahead of the crack tip into (1). The matching method has the advantage that almost no additional calculation is required even in the FGM case, but it requires a high degree of mesh refinement and often suffers from instability as the crack tip is approached (see Anderson, 1995). Another way, the domain integral method, which is an energy approach based on the J-integral and which has been proved to be efficient for homogeneous materials, is the focus of our numerical study here.

In the domain integral method, the energy release rate J is calculated through an area integral in the two-dimensional case and stress intensity factors are then obtained using (4). The area integral approach provides much better accuracy than directly evaluating the contour integral in (5), and is easier to implement numerically. Early works along the line of the energy approach were given by Parks (1974, 1977), Hellen (1975), and deLorenzi (1982). Shih and his co-workers (see Li, Shih, and Needleman, 1985; Shih, Moran, and Nakamura, 1986; Moran and Shih, 1987) formulated the domain integral methodology in a general way. For homogeneous materials, it has been applied in above works to elastic and plastic material responses, mechanical and thermal loadings, and two-dimensional and three-dimensional spaces. We will discuss the application of the domain integral to nonhomogeneous materials. In particular, we will show that the integral term representing the effect of nonhomogeneity may be neglected when evaluating the integration at a region close the crack tip; therefore, the standard domain integral for homogeneous materials gives sufficient accuracy. We will discuss the elastic case; the conclusion may be extended to the power-law hardening case, i.e., HRR singularity (Hutchinson, 1968; Rice and Rosengren, 1968).

Consider an annular region A_I around the crack tip in the two-dimensional case, as shown in Fig. 1. For simplicity in the discussion, we consider that the material variation is along the x-axis; and only one of the two material parameters, the Young's modulus, has a gradient where the Poisson's ratio is taken as a constant since its variation is usually small compared to the former. The conclusion obtained below can be extended to the general material variation case. Both the inner and outer boundary of the region A_I are sufficiently close to the crack tip. The J given in (5) can be written in terms of the boundary integral.

$$J = \oint_C (\sigma_{ij}u_{i,1} - W\delta_{1j})qm_j\,ds \tag{6}$$

where $C = C_2 + C_3 + C_1 + C_4$ is the boundary of A_I; m_i is the outward normal of A_I; on C_1, $m_j = -n_j$, and on C_2, $m_j = n_j$; and q is a smooth function which has the value of unity on C_1 and zero on C_2. Applying the divergence theorem to (6) gives

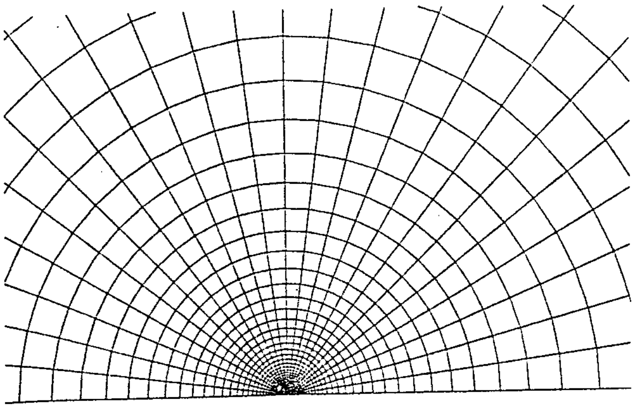

Fig. 2 Finite element mesh of the crack-tip region. In our calculation four-node bilinear elements are used. The smallest element at the tip is 10^{-5} times a characteristic length.

$$J = \int_{A_I} (\sigma_{ij}u_{i,1} - W\delta_{1j}) q_{,j} dA - \int_{A_I} W_{,1} q dA. \qquad (7)$$

Here, $W = W[E(x), \epsilon(x, y)]$. The derivative of W under the second integral is with respect to the coordinate x in $E(x)$. Comparing with the homogeneous case, the second integral is an additional term which represents the effect of nonhomogeneity.

In numerical implementation, the inner contour C_1 is usually taken as the crack tip, and the outer boundary C_2 is taken to be the same as element boundaries. The function q defined above is an arbitrary function as long as it gives the correct values at the boundaries, C_1 and C_2. It was shown by Shih and his coworkers in the previously mentioned papers that the calculated J is insensitive to the choice of q. The value of it within an element may be taken as

$$q = \sum_{i=1}^{n} N_i q_i \qquad (8)$$

where N_i are the shape functions of the element, n is the number of nodes per element, and q_i are the nodal values of q, which are assigned in accordance with a smooth function varying from zero at the outer boundary to unity at the crack tip. The derivative of q with respect to the coordinate x_i is

$$\frac{\partial q}{\partial x_i} = \sum_{i=1}^{n} \sum_{k=1}^{2} \frac{\partial N_i}{\partial \eta_k} \frac{\partial \eta_k}{\partial x_i} q_i \qquad (9)$$

where η_k are the coordinates in the isoparametric space. Evaluating the quantity under the integral in (7) at the Gauss integration points, J is obtained numerically by

$$J = \sum_{A_I} \sum_{p=1}^{n} \left\{ [(\sigma_{ij}u_{i,1} - W\delta_{1j})q_{,j} - W_{,1}q] \det\left(\frac{\partial x_k}{\partial \eta_k}\right) \right\}_p w_p. \qquad (10)$$

Here, w_p is the weight function of integration, and det $(\cdot)$ is the determinant of Jacobian matrix.

The mesh design for our nonhomogeneous problems is a standard mesh design for crack problems. The crack tip is surrounded by an arrangement of wedge-shaped isoparametric elements. The same type of elements makes circular rings which surround the wedge-shaped elements at the tip (see Fig. 2). In this region, the size of the elements increases along the radial direction according to the exponential scale which gives the unit aspect ratio of the elements. The smallest elements at the crack tip are smaller or equal to $10^{-5}a$, where a is a characteristic length. Between the circular region and the region far away from the tip where the stresses vary regularly, there is a transition zone in which the element shape changes gradually from the curved polygon to the regular element shape. The geometry of a typical mesh of this kind was shown in the previously mentioned papers (also see Shih and Asaro, 1989). It is noted that near the tip the mesh needs to be refined to account for the high-stress gradients associated with the singularity; in the FGM case, also to account for the material property variation.

Using this type of mesh, we show here that if we evaluate the domain integral in the region sufficiently small around the crack tip, the value of the second term in (7) involving the derivative of W is very small, essentially negligible. The domain integral in practice can be calculated in the region close to the crack tip (the circular domain consisting of the first 10 or 20 circular rings of elements at the crack tip zone) as demonstrated in the next section. In our calculations, as mentioned above, the smallest element is in the size of $10^{-5}a$, where a is the characteristic length. In such a situation, the second integral in (7) may be estimated as follows. Using the above mesh design, the first 10 or 20 rings of elements are arranged within the radius $10^{-4}a$ from the crack tip. The weight functions for the two integrals in the expression (7) are q and $q_{,j}$. If the pyramid shape for the function q (Fig. 3(a)) is used, its derivative with respect to the coordinates is on the order of $10^4 a^{-1}$ considering that the domain is within a circle with radius $10^{-4}a$. Then, the weight functions of the first and second integrals are of the orders 10^4 and 1, respectively. Note that a^{-1} in the derivative of q has been moved to the integrand of the first integral. The first integral is overweighted by its weight function compared to that of the second. On the other hand, the two integrands are not likely to differ by such a large amount as that of the weight functions, i.e., to be of the same order. This is due to the following: (a) they both are essentially energy density terms (energy density unit/length) calculated using stress and strain fields; (b) both are proportional to the loading, the square of the stress intensity factor K_I^2; and (c) the first is proportional to the inverse of the modulus and the second is proportional to the derivative of the modulus divided by the square of the modulus. Since such a small domain for the domain integral is well within the K-dominance zone, the asymptotic expressions (1) and (2) are valid within it. The K-dominance zone for FGMs has been examined in Gu and Asaro (1997b), where it has been shown that within the distance of a few percent of the characteristic length, the difference of the stress fields of the asymptotic and full solutions are within a few percent. Substituting (1) and (2) into the two integrands, (b) and (c) can be confirmed. This permits us to write

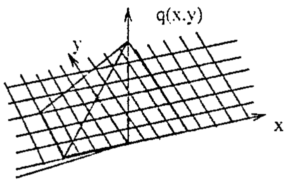

(a) pyramid function

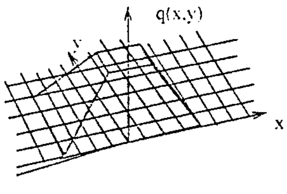

(b) plateau function

Fig. 3 The two often used shapes of q function

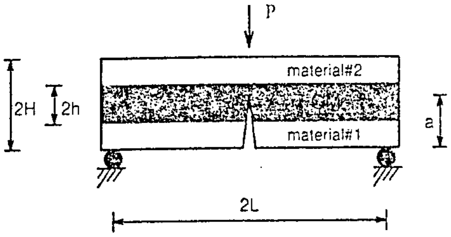

Fig. 4(*a*)

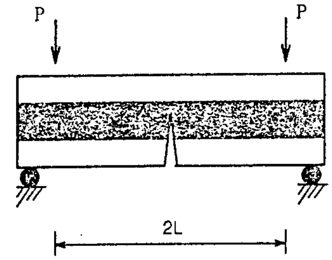

Fig. 4(*b*)

Fig. 4 Two sandwiched bending specimens with FGM interlayer: (*a*) three-point bending; (*b*) four-point bending

$$[\text{first integrand}] = \frac{K_I^2}{E_0 a}\frac{f_1(\theta)}{r}$$

$$[\text{second integrand}] = \frac{K_I^2 E_0'}{E_0^2}\frac{f_2(\theta)}{r}. \tag{11}$$

In (11), E_0' is the derivative of the Young modulus at the crack tip: f_1 and f_2 are obtained from angular functions in (1) and (2), and therefore they do not have much effect on the magnitudes of the two integrands. In our discussion, we assume that there is only mode I loading. However, one can obtain the same conclusion for mixed-mode presentation through similar steps. Also, $E_0'a$ is roughly proportional to E_0 as can be seen from the following example. Consider the FGM interlayer in Fig. 4 with linear modulus variation, we have $E_0 = (E_2 + E_1)/2$ and $E_0'a = E_0 a\zeta/2/h$ when the crack tip is at the middle of the FGM interlayer, where the subscripts denote the properties for material #1 and #2. and $\zeta = (E_2 - E_1)/(E_2 + E_1)$. The variation of the multiplier ζ, as E_2/E_1 varies, is small. So, the two scale factors in the above expression (11) would not differ much as long as a and h do not differ much, and this is similar for other material variation forms. Note that if h is the smallest length compared to other dimensional lengths, one could chose the characteristic length a to be h so that $a/h = 1$. If E_0 and $E_0'a$ are of the same order, from the above analysis we estimate that the first integral is 10^4 times the second integral. In general, the difference between E_0 and $E_0'a$ is not significant at all, compared to that of the two weight functions and therefore the second term in (7) may be neglected. It may also be shown that the conclusion is true by a similar step if the plateau shape for the q function (Fig. 3(*b*)) is used.

Suppose that r_D is the radius of domain where the domain integral is evaluated and within it the field can be well represented by the singular field (1) and (2), then from the above analysis the error of neglecting the second term can be estimated as

$$e \approx \frac{r_D E_0'/E_0}{1 + r_D E_0'/E_0}. \tag{12}$$

The error is very small if we choose r_D to be sufficiently small. The simplified method has the following advantages: (a) it gives the same accuracy for the stress intensity factors as the domain integral for homogeneous materials, as we shall see in numerical examples; (b) the input of the derivatives of the material properties (gradients) is not required such that in the numerical implantation only material properties need to be assigned to elements or Gauss integration points and this is easy to achieve; and (c) no additional calculations are required as compared to the homogeneous case.

When the gradient of the thermal expansion coefficient of the FGM does not vanish and thermal loading (temperature change) is applied, the additional term related to the gradient of the thermal expansion coefficient is an integrand under the second integral in (7) which can be written as

$$[\text{thermal term under second integral}] = K_I T_0 \alpha_0' \frac{f_3(\theta)}{\sqrt{r}} \tag{13}$$

where T_0 is temperature change at the crack tip, α_0' is the gradient of thermal expansion coefficient at the crack tip, and f_3 is obtained from the angular function in (1). This term may also be neglected due to the following reasons. First, it is under the second integral in (7). As analyzed before, the first integral is overweighted. Second, the $1/r$ factor in first integrand, given in (11), is much larger than the $1/\sqrt{r}$ factor in (13), in the domain with radius $10^{-4}a$. Third, since the stress solution only depends on the ratio of the muduli of the two bulk materials for traction problems (as we shall see in next section), the two moduli may be chosen in the calculation such that $1/E_0$ in (11) is in a normal range. Having these, we can estimate that the magnitude of (13) and that of the first expression of (11) do not differ much.

We have gone a rigorous way to show that the standard domain integral can be directly used for nonhomogeneous materials. A simple way to argue this is that since the asymptotic expressions (1) and (2) are the same as those for homogeneous materials with the material properties being those at the crack tip, there exists a small homogeneous zone which may be regarded as the K-dominance zone so that the standard domain integral is valid there. But from this simple way it is impossible to obtain the above error analysis. When the second term is neglected, the expression to numerically calculate domain integral becomes

$$J = \sum_{A_I}\sum_{p=1}^{n}\left\{[(\sigma_{ij}u_{i,1} - W\delta_{1j})q_{,j}] \det\left(\frac{\partial x_k}{\partial \eta_k}\right)\right\}_p w_p. \tag{14}$$

which is the same as that for the homogeneous case.

When the domain integral is obtained, the stress intensity factors can be evaluated using (4). If there is only mode I stress intensity factor at the tip due to the symmetric material properties, the geometry and the loading, it can be evaluated directly from (4). If it is a mixed-mode problem, the interaction energy release rate defined in Shih and Asaro (1989) may be evaluated instead of the energy release rate in (4). Using the interaction energy release rate, modes I and II can be separated.

3 Numerical Results

We have extensively tested the numerical method using many crack geometries and loadings. The results have been compared with those obtained by other methods, such as displacement-matching and singular integral equations. All showed the method to be accurate, convergent to the correct solution. The domain integral evaluated from the domains near the tip is stable, independent of the domain chosen. The following are four examples that illustrate this.

The first example is an edge-cracked plate made of a FGM, subject to remote constant strain. It has been solved previously by Erdogan and Wu (1993), using the singular integral equation method. We use it to check the accuracy of our scheme. The second and the third are three-point bending and four-point bending specimens made of sandwiched structures with the interlayers being FGMs (Fig. 4). The interlayer is a zone of transition wherein the material properties change smoothly from the upper layer to the lower layer. The length $2L$ is assumed to be sufficiently large so that it would not affect the solutions. The height of the bars is $2H$, the crack length a, and the height of the interlayers $2h$. The crack is perpendicular to the upper and lower boundaries, and its tip is inside the FGM. The sandwiched structures can be used to study either the fracture of FGMs or the interface behavior when the interlayer thickness is small compared to those of the two bulk layers. The geometry of the first example is the same as Fig. 4, and the only difference is that it is a single piece of FGM for the constant strain problem.

The mesh design was discussed in the previous section. The four-node bilinear elements are used in the study. We have extensively tested the numerical method by changing the material properties, the loadings, and the specimen dimensions. We also have changed the size of the domain by changing the number of rings of elements. All of the stress intensity factors evaluated from the domain integral have shown the accuracy of the scheme. The convergence study results will be provided in tabular form later in the section. The material property variation is achieved by using corresponding material properties at Gauss integration points of each element. We use the software package ABAQUS to perform the calculation, and only the user-subroutine UMAT is required for the material variation. The J-integral is also calculated using the standard domain integral function provided in ABAQUS.

For real FGMs, the property variation along the thickness can be linear, exponential, or some other form. For elastic problems, both Young's modulus and Poisson's ratio vary with the position in general. It is assumed in all examples in this section that the former has the major effect and the latter is taken to be constant. It is reasonable to do so since the variation of the Poisson's ratios is usually small compared to that of the moduli. For the problems studied (see Fig. 4), the Young's modulus is expressed by the following:

$$E(y) = Ay + B$$

$$E(y) = A\exp(By) \qquad (15)$$

where A and B are material constants which represent material gradients. The origin of the coordinates is at the center of these specimens and y is along the thickness direction. The first expression in (15) is a linear form, whereas the second is an exponential form. Given the moduli of the lower and upper layer, E_1 and E_2, the two constants are expressed as

$$A = \frac{E_2 - E_1}{2h}, \quad B = \frac{E_2 + E_1}{2} \qquad (16)$$

for the linear gradient, and

$$A = \sqrt{E_1 E_2}, \quad B = \frac{1}{2h}\log\left(\frac{E_2}{E_1}\right) \qquad (17)$$

for the exponential variation.

In the first example, material variation along the thickness is taken to be the exponential form in (15). The loading is a constant strain ϵ_0 far away from the crack at the two ends which gives rise to a remote stress field, $\sigma = \sigma_0\exp(By)$, where $\sigma_0 = A\epsilon_0/(1 - \nu^2)$. The energy release rate was calculated from the domains formed by the first 20 rings, using the J-integral evaluation function in ABAQUS. The results from the first ten rings are shown in Table 1, given for different E_2/E_1 ratios, and the results from the domains formed by the remaining ten rings of elements basically are the same as those of column 9 and 10 in the table. The ratio E_2/E_1 is the modulus of the upper boundary over that of the lower boundary. In the calculation we choose $\sigma_0 = 1$ and the crack length $a = 1$. From the table, the convergence of the numerical method is clearly seen. When the ratio is 1, it represents homogeneous material. In the strong material variation case, the ratio is 10. We see that in both cases the convergence behavior is the same. So, we may conclude that the convergence of using the standard domain integral for FGMs is the same as that for homogeneous materials. The domain integral scheme has been proved to be a useful one in the numerical analysis of the homogeneous fracture. Note that those results from the domains formed by the first two rings usually have a relatively large error in both the homogeneous and FGM case, due to the inaccuracy of the innermost elements. Thus, those results from the domains formed by the first two rings may be disregarded. The stress intensity factors obtained from the four cases in the table, in which the ratio is equal to 0.1, 0.2, 5, and 10, are 4.01, 4.22, 6.49, and 7.48, respectively. These results are the same as those obtained from the singular integral equation method provided by Erdogan and Wu (1993).

Due to the symmetric geometries and symmetric material properties with respect to the crack line for the two specimens in Fig. 4, there is only mode I stress intensity factor at the crack tip for the second and third examples. Since the near-tip fields are of the same form as those for homogeneous materials, the generic form of the stress intensity factor may be written as

$$K_I = Ta^{1/2}Y\left(\frac{E_2}{E_1}, \frac{a}{H}, \frac{h}{H}, \wp\right) \qquad (18)$$

where T is a representative stress magnitude, a is a characteristic length (can be taken as the crack length) and Y is a dimensionless function which is related to the geometries of the problems and material properties: the ratio of the moduli and $\wp$, the form of material variation. There are four independent variables in the dimensionless function Y. For known material variation $\wp$ and the thickness of the FGM h/H, the solution Y depends on the modulus ratio and the position of the crack tip a/H, and may be systemically presented by tables or figures. For example, if using tables, each table contains the solution for given $\wp$ and h/H, where the row represents E_2/E_1 and the column represents a/H. If using figures, each figure contains the solution for given $\wp$ and h/H, and in the figure each curve corresponds to a value E_2/E_1 with the x-axis being a/H. Given the representatives of $\wp$ and h/H, we construct the complete solution in above ways for others to use. For homogeneous materials, Y is only related to a/H. It is obtained in terms of a figure or empirical expressions which are given in the handbook by Tada et al. (1985).

Figure 5 shows the solution of mode I stress intensity factor versus the position of the crack tip in the FGM for linear mate-

Table 1 Convergence for the Remote Constant Strain Problem

E_2/E_1	Energy release rate calculated from the first ten rings [in units of $\sigma_0^2 a/E_1$] 1	2	3	4	5	6	7	8	9	10
0.1	42.43	46.15	46.21	46.24	46.25	46.26	46.26	46.26	46.28	46.27
0.2	33.26	36.17	36.22	36.24	36.25	36.26	36.26	36.26	36.27	36.27
1	20.99	22.83	22.86	22.88	22.88	22.89	22.89	22.89	22.90	22.90
5	15.76	17.14	17.16	17.17	17.18	17.18	17.18	17.18	17.19	17.19
10	14.78	16.07	16.09	16.10	16.11	16.11	16.11	16.11	16.12	16.12

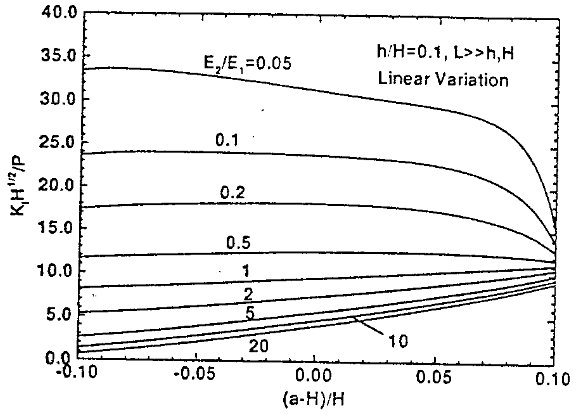

Fig. 5 Stress intensity factor versus crack-tip position in the FGM interlayer for three-point bending with $h/H = 0.1$

rial variation in the three-point bending specimen, where $h/H = 0.1$. The geometry represents the case where the interlayer of FGM is considerably thin compared to the two bulk materials. It is seen that the curves in the figure are the nondimensional function Y in (18) if the characteristic length is taken to be H. The solutions of this kind for various h/H and $\wp$ form a complete solution for the three-point bending specimen. Usually tough materials such as metals have a lower modulus than brittle materials such as ceramics. From this figure, when the crack travels from a tough side (the side with smaller modulus) to a brittle side (the side with larger modulus) the crack-tip stresses increase. The energy release rate calculated from the domains formed by the first ten rings of elements is listed in Table 2 for both linear and exponential material variations. The stable results in the table again show the convergence of the numerical scheme. When the toughness of the two bulk materials is different, it is expected to vary along the thickness of the FGM and can be written as $\Gamma((a-H)/H)$ in the FGM. Then, for stable growth in the FGM interlayer we have

$$G\left(\frac{a-H}{H}\right) = \frac{K_I^2\left(\frac{a-H}{H}\right)}{E\left(\frac{a-H}{H}\right)} = \Gamma\left(\frac{a-H}{H}\right)$$

$$\frac{\partial G\left(\frac{a-H}{H}\right)}{\partial a} < \frac{\partial \Gamma\left(\frac{a-H}{H}\right)}{\partial a}. \tag{19}$$

For unstable growth, in the second equation "<" is replaced by ">." Let's consider a special case where the toughness is constant across the thickness of the FGM. From the figure, we see in this special case that when material #2 is much softer than material #1, $E_2/E_1 \ll 1$, the crack growth is likely to be stable. This is especially true when the crack tip is close to material #2. When material #2 is stiffer than material #1, the crack growth is likely to be unstable. In general, if the toughness varies with position and the crack is close to material #2 with $E_2/E_1 \ll 1$, it is a stable growth when the decrease of the slope in the figure overcomes the decrease of the toughness. Figure 6 represents the case when $h/H = 0.5$ and other parameters are the same as Fig. 5. From the two figures we see that the trend of these curves has a dramatic change as the percentage of the FGM changes, and this is especially true for those curves with $E_2/E_1 < 1$. For many crack-tip positions in Fig. 6 the stress intensity factor increases as the crack length increases. This means that if the increase of the toughness at the crack tip as the crack length increases is not as fast as the stress intensity factor, it is an unstable growth for the crack tip traveling in those positions. In the above discussion of the crack growth, we have assumed that the crack propagates along the original direction, since these are the cases where geometry, loading, and material are symmetric with respect to the crack line. A first-order approximation model, which is based on local homogeneity, has been used to examine the crack propagating direction for several cracked FGM geometries (Gu and Asaro, 1997b). The model also predicts that a crack grows along its original direction when everything is symmetric.

For the four-point bending specimen shown in Fig. 4, the two ends far away from the crack line is in a pure bending state, where the bending moment $M = Pl$ and l is the distance between the applied force and the support of the beam. The neutral axis changes with material properties, material variation, and layer's thicknesses and is known when these are given. Our numerical results show very good convergence as those listed in Table 1 and 2. Figures 7(*a*) and (*b*) illustrate the stress intensity factor versus the interlayer thickness for the crack tip at the center of the beam and linear material variation. It is recognized that these curves are the function Y in (18) if the characteristic length is chosen as H. Compared to Fig. 5, this is another way to present the solution: each curve represents a case for a value E_2/E_1, given $\wp$ and a/H. In these two figures, for a fixed H and as h/H increases, the K_I increases when $E_2/E_1 > 1$ and decreases when $E_2/E_1 < 1$. When h/H is zero, it is the bimaterial solution. The figure tells us that although the increase of the percentage of the FGM in the structure due to the increase of interlayer thickness reduces the mismatch between the two bulk materials, it may not reduce the stress intensities at the crack tip. The increase or decrease of the stress intensities depends on the crack position. As far as the crack propagation is concerned, at this point we do not know how the toughness changes with the FGM percentage increase (note that the increase of the percentage reduces the material gradients). So we do not know if the increase of FGM percentage can prevent the crack growth. However, under the special case that the toughness is constant for FGM, we may conclude that the increase of FGM percentage may not be good to prevent crack growth. In another paper (Dao et al., 1997) we have shown that the increase of FGM percentage may not reduce microstress concentration at the grain size level under thermal loading for a perfect FGM without cracking. The conclusion of the microstress concentration was obtained from a statistically based analysis.

Using a similar analysis, the method can be extended to the three-dimensional case. In three-dimensional space, the domain can be chosen such that its boundary is a tube, which surrounds the crack tip and whose radius of the cross section is sufficiently

Table 2 Convergence for the Three-Point Bending Specimen*

$\wp$	Energy release rate calculated from the first ten rings [in units of $P^2/(HE_1)$]									
	1	2	3	4	5	6	7	8	9	10
linear	466.8	507.7	508.4	508.7	508.8	508.9	508.9	508.9	509.1	509.1
exponential	542.7	590.2	591.1	591.4	591.6	591.6	591.7	591.7	591.9	591.8

* The numerical results in the table are for $h/H = 0.1$, $(a-H)/H = -0.1$ and $E_2/E_1 = 0.1$

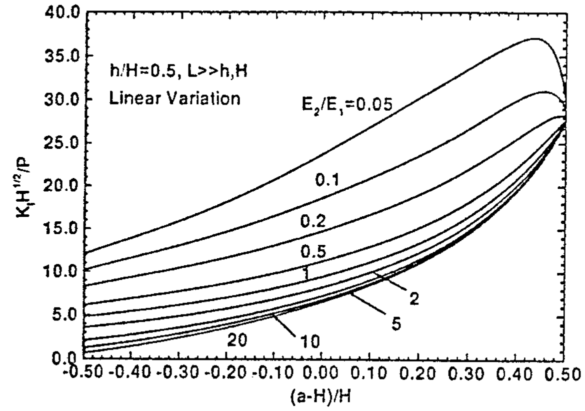

Fig. 6 Stress intensity factor versus crack-tip position in the FGM interlayer for three-point bending with $h/H = 0.5$

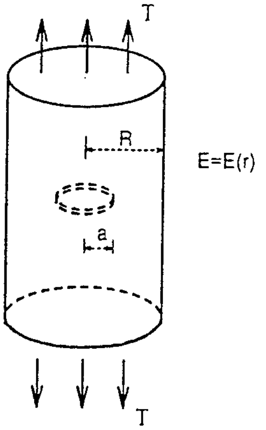

Fig. 8 Penny-shaped crack in a cylindrical FGM solid

small such that the analysis similar to the two-dimensional case can be applied. Detailed discussion of the three-dimensional standard domain integral can be found in previously mentioned papers on the domain integral. The reason for which the simplified method is true is exactly the same as that for the two-dimensional case, i.e., the standard domain integral is overweighted compared to the nonhomogeneous terms. Here we will only give an example of a special version in three-dimensional space, an asymmetric problem shown in Fig. 8. The detailed discussion of the general three-dimensional problem will be given in a separate article elsewhere. The penny-shaped crack (Fig. 8) is in a cylindrical solid. The radius of the crack is a, the radius of the cross section is R, and the length of the solid is so large as not to affect the solution. The Young's modulus is considered to vary along the radius direction, $E = E(r)$. By the structure of the crack-tip field and dimensional consideration, the solution is given in the form

$$K_I = Ta^{1/2}Y\left(\frac{E_2}{E_1}, \frac{a}{R}, \wp\right) \tag{20}$$

where E_2 is the modulus at the outer boundary and E_1 is the modulus at the asymmetric line. The solution to the problem can be easily documented compared to the three-layer bending bars, since we have fewer dependent parameters in the nondimensional function Y here. For given material variation $\wp$, the solution can be presented by a table or a figure. Table 3 shows the convergence for linear and exponential variations, where $E_2/E_1 = 20$ and $a/R = 0.5$. The convergence is very much similar to the two-dimensional case. Except for the first one or two rings, others give the accurate solution.

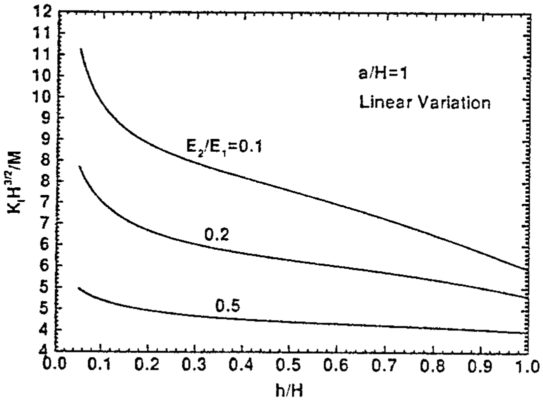

Fig. 7(*a*)

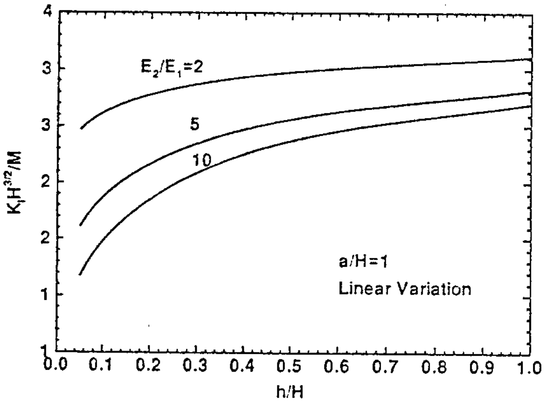

Fig. 7(*b*)

Fig. 7 Stress intensity factor versus thickness of the FGM interlayer for four-point bending

4 Concluding Remarks

We have shown that the standard domain integral can be used to evaluate the crack-tip field for nonhomogeneous materials, such as FGMs. The method requires a sufficiently fine mesh near the crack tip as shown. However, the error induced by the method is estimated such that one can control the error by controlling the size of the domain where the domain integral is evaluated. From the numerical solutions given in the previous section, we have seen that the energy release rate calculated from the domains formed by the rings of elements around the crack tip in this way is very stable and accurate. The examples are all in mode I where both loading, geometry, and material variation are symmetric with respect to the crack face, but the method can be used to calculate the modes I and II stress intensity factors for the mixed-mode case using a defined interaction energy release rate by Shih and Asaro (1989). The method may also be extended to the nonlinear case, such as plastic crack problems. These all suggest that this simplified method, without the input of material gradients and without many changes of the existing finite element code for homogeneous materials, may be well suited for crack mechanics analysis of FGMs where the materials possess gradients. In the examples of the sandwiched structure we have presented the solution in a compact functional form which can be used to easily document a complete solution for other study and design purpose. Finally, it is noted that the material variation is assumed to be continuous across the thickness of the FGM in this study. For real FGMs, the material variation is created by the spatial distribution of one material phase relative to the other. The continuous approach, the proposed numerical method and the fracture behav-

Table 3 Convergence for Penny-Shaped Crack in a Cylindrical Solid*

$\wp$	Energy release rate calculated from the first ten rings [in units of T^2a/E_1]									
	1	2	3	4	5	6	7	8	9	10
linear	0.04260	0.04633	0.04640	0.04642	0.04644	0.04644	0.04645	0.04645	0.04646	0.04646
exponential	0.03286	0.03574	0.03579	0.03581	0.03582	0.03583	0.03583	0.03583	0.03584	0.03584

* The numerical results in the table are for $a/R = 0.5$ and $E_2/E_1 = 20$

ior analysis in the previous section, implies that the particle size of the phases that make the FGMs is very small compared to the crack length and other geometrical lengths, and the microstructure of the FGMs is sufficiently fine. In the above condition, the effect of the particle size in the mechanics analysis may be neglected.

Acknowledgment

This work was supported by the Office of Naval Research through grant N00014-93-1-1164. We are grateful to Prof. C. F. Shih of Brown University with whom we had helpful discussions. We are also grateful to Dr. Q. S. Yu of UCSD who made helpful suggestions in the presentation of the material.

References

Anderson, T. L., 1995, *Fracture Mechanics—Fundamentals and Applications*, 2nd Ed., CRC Press, Boca Raton, FL.

Dao, M., Gu, P., Maewal, A., and Asaro, R. J., 1997, "A Micromechanical Study of Residual Stresses in Functionally Graded Materials," *Acta Metallurgica*, Vol. 45, pp. 3265–3276.

Delale, F., and Erdogan, F., 1983, "The Crack Problem for a Nonhomogeneous Plane," ASME JOURNAL OF APPLIED MECHANICS, Vol. 50, pp. 609–614.

Delale, F., and Erdogan, F., 1988, "On the Mechanical Modeling of the Interfacial Region in Bonded Half-Planes," ASME JOURNAL OF APPLIED MECHANICS, Vol. 55, pp. 317–324.

deLorenzi, H. G., 1982, "On Energy Release Rate and the *J*-Integral for 3-D Crack Configurations," *International Journal of Fracture*, Vol. 19, pp. 183–193.

Erdogan, F., and Wu, B. H., 1993, "Analysis of FGM Specimens for Fracture Toughness Testing," *Ceramic Transactions*, Vol. 34, J. B. Holt et al., eds., The American Ceramic Society, Westerville, OH.

Gu, P., and Asaro, R. J., 1997a, "Cracks in Functionally Graded Materials," *International Journal of Solids and Structures*, Vol. 34, pp. 1–17.

Gu, P., and Asaro, R. J., 1997b, "Crack Deflection in Functionally Graded Materials," *International Journal of Solids and Structures*, Vol. 34, pp. 3085–3098.

Hellen, T. K., 1975, "On The Method of Virtual Crack Extension," *International Journal of Numerical Methods in Engineering*, Vol. 9, pp. 187–207.

Hutchinson, J. W., 1968, "Singular Behavior at the End of a Tensile Crack Tip in a Hardening Material," *Journal of the Mechanics and Physics of Solids*, Vol. 16, pp. 13–31.

Li, F. Z., Shih, C. F., and Needleman, A., 1985, "A Comparison of Methods for Calculating Energy Release Rates," *Engineering Fracture Mechanics*, Vol. 21, pp. 405–421.

Moran, B., and Shih, C. F., 1987, "A General Treatment of Crack Tip Contour Integrals," *International Journal Fracture*, Vol. 35, pp. 295–310.

Parks, D. M., 1974, "A Stiffness Derivative Finite Element Technique for Determination of Crack Tip Stress Intensity Factors," *International Journal Fracture*, Vol. 10, pp. 487–502.

Parks, D. M., 1977, "The Virtual Crack Extension Method for Nonlinear Material Behavior," *Computational Method in Applied Mechanics and Engineering*, Vol. 12, pp. 353–365.

Rice, J. R., 1968, "A Path Independent Integral and The Approximate Analysis of Strain Concentration by Notches and Cracks," ASME JOURNAL OF APPLIED MECHANICS, Vol. 35, pp. 379–386.

Rice, J. R., and Rosengren, G. F., 1968, "Plane Strain Deformation near a Crack Tip in a Power-Law Hardening Material," *Journal of the Mechanics and Physics of Solids*, Vol. 16, pp. 1–12

Shih, C. F., Moran, B., and Nakamura, T., 1986, "Energy Release Rate along a Three-Dimensional Crack Front in A Thermally Stressed Body," *International Journal Fracture*, Vol. 30, pp. 79–102.

Shih, C. F., and Asaro, R. J., 1989, "Elastic-plastic Analysis of Cracks on Bimaterial Interfaces: Part I—small Scale Yielding," ASME JOURNAL APPLIED MECHANICS, Vol. 55, pp. 299–316.

Tada, H., Paris, P. C., and Irwin, G. R., 1985, *The Stress Analysis of Cracks Handbook*, 2nd Ed., Paris Publications, St. Louis, MO.